IN-SITU STRESS MAGNITUDE AND ORIENTATION DETERMINATION OF ANKARA KAZAN DISTRICT FROM FMI LOG

A THESIS SUBMITTED TO
THE GRADUATE SCHOOL OF NATURAL AND APPLIED SCIENCES
OF
MIDDLE EAST TECHNICAL UNIVERSITY

BY

KUTAY EMRE KARADENIZ

IN PARTIAL FULFILLMENT OF THE REQUIREMENTS
FOR
THE DEGREE OF MASTER OF SCIENCE
IN
MINING ENGINEERING

SEPTEMBER 2019

Approval of the thesis:

IN-SITU STRESS MAGNITUDE AND ORIENTATION DETERMINATION OF ANKARA KAZAN DISTRICT FROM FMI LOG

submitted by **KUTAY EMRE KARADENIZ** in partial fulfillment of the requirements for the degree of **Master of Science in Mining Engineering Department, Middle East Technical University** by,

Prof. Dr. Halil Kalıpçılar
Dean, Graduate School of **Natural and Applied Sciences** _____

Prof. Dr. Celal Karpuz
Head of Department, **Mining Engineering** _____

Prof. Dr. Hasan Öztürk
Supervisor, **Mining Engineering, METU** _____

Examining Committee Members:

Assist. Prof. Dr. Onur Gölbaşı
Mining Engineering Department, METU _____

Prof. Dr. Hasan Öztürk
Mining Engineering, METU _____

Assist. Prof. Dr. Serhat Canbolat
Petroleum and Natural Gas Engineering Department, NEU _____

Date: 03.09.2019

I hereby declare that all information in this document has been obtained and presented in accordance with academic rules and ethical conduct. I also declare that, as required by these rules and conduct, I have fully cited and referenced all material and results that are not original to this work.

Name, Surname: Kutay Emre Karadeniz

Signature:

ABSTRACT

IN-SITU STRESS MAGNITUDE AND ORIENTATION DETERMINATION OF ANKARA KAZAN DISTRICT FROM FMI LOG

Karadeniz, Kutay Emre
Master of Science, Mining Engineering
Supervisor: Prof. Dr. Hasan Öztürk

September 2019, 116 pages

Wellbore instability is a major problem in the oil and gas industry. Rock failures occur around the borehole when the induced local stresses exceed the rock strength. Borehole breakouts and drilling-induced fractures (DIFs) are important indicators of horizontal stress orientation. Borehole breakouts are stress-induced enlargements of the wellbore cross-section which occurs when the stresses around the borehole exceed the compressive strength of the borehole wall. DIFs are created when the stresses concentrated around a borehole exceed tensile strength of the wellbore wall. In this study, a Formation Micro Imager (FMI) log which was carried out for a solution mining project in Kazan district of Ankara was used to determine the in-situ horizontal stress magnitude and orientation determination of the site. The FMI log was analyzed to determine and differentiate the DIFs and breakouts. Laboratory and field studies were carried out to determine the mechanical properties of the formations that the well was passing through. Leak-off tests from the field studies were analyzed to determine minimum horizontal stress magnitude. Later numerical analyses of various circular cross-sections of the borehole was done using FLAC to mimic the DIFs and breakouts. An iterative in-situ horizontal stress inputs were tried in the models until matching the failures around the borehole. Later, the orientation and magnitude of the horizontal

stresses around the borehole was determined using both analytical and numerical methods.

Keywords: FMI Log, Breakout, Drilling Induced Fracture (DIF), In-Situ Stress, Numerical Modelling, Analytical Solution

ÖZ

ANKARA KAZAN BÖLGESININ FMI LOGUNDAN ARAZI GERILME DEĞERI VE YÖNELIMI TAYINI

Karadeniz, Kutay Emre
Yüksek Lisans, Maden Mühendisliği
Tez Danışmanı: Prof. Dr. Hasan Öztürk

Eylül 2019, 116 sayfa

Petrol ve doğal gaz endüstrilerinde, sondaj kuyusu dayanıksızlığı önemli bir problem teşkil etmektedir. Uyarılan bölgesel gerilme, etrafındaki kayaçların dayanımını aşarsa sondaj kuyusu etrafında kayaç yenilmeleri meydana gelir. Sondaj kuyusu kesmeleri ve uyarılmış sondaj çatlakları, yatay gerilme yönelmesinin önemli göstergeleridir. Sondaj kuyusu kesmeleri, kuyu etrafındaki gerilmelerin kuyu duvarlarındaki basma dayanımını aşmasıyla, kuyu kesitinde meydana gelen gerilme kaynaklı genişlemelerdir. Uyarılmış sondaj çatlakları ise kuyu etrafındaki gerilme konsantrasyonunun kuyu duvarlarındaki çekme dayanımını aşmasıyla meydana gelmektedir. Bu çalışmada, Ankara Kazan bölgesinde bulunan çözelti madenciliği sahasının arazi yatay gerilme değerlerini ve yönelimini tayin etmek için Mikro Formasyon Görüntüleme günlüğü (MFG) uygulandı. Sondaj kuyusu kesmelerini ve uyarılmış sondaj çatlaklarını belirlemek ve ayırt etmek için kullanılan Mikro Formasyon Görüntüleme günlüğü analiz edildi. Kuyu boyunca bulunan formasyonların mekanik özelliklerini belirlemek için laboratuvar ve arazi çalışmaları yapıldı. Arazide yapılan kaçak testleri, asgari yatay gerilmeyi belirlemek için analiz edildi. Ayrıca, sayısal program modelleri sondaj kuyusu kesmelerine ve uyarılmış sondaj çatlaklarına benzetilerek, çeşitli dairesel kuyu kesitlerinin sayısal analizleri FLAC programları kullanılarak yapıldı. Modellemelerde, yatay arazi gerilme girdileri

iterasyon yapılarak kuyu etrafındaki yenilmelere ulaşılana kadar denendi. Son olarak, her iki analitik ve sayısal yöntemleri kullanarak, kuyu etrafındaki yatay gerilmelerin büyüklüğü ve yönelimi belirlendi.

Anahtar Kelimeler: Mikro Formasyon Görüntüleme (MFG) logu, Uyarılmış sondaj çatlağı, Yerinde Arazi gerilmesi, Sayısal modelleme, Analitik çözüm

To My Family

ACKNOWLEDGEMENTS

I would like to express my deep gratitude to my supervisor Prof. Dr. Hasan ÖZTÜRK. He broadened my horizon for academic studies with his valuable guidance. Therefore, I would like to thank him for his encouraging notion of work throughout this study.

I am also thankful to the examining committee members, Asst. Prof. Dr. Onur GÖLBAŞI and Asst. Prof. Dr. Serhat CANBOLAT for their comments and supervisions. I would also like to thank to Güray ÇAKMAKÇI for providing data.

I am especially grateful to Asst. Prof. Dr. Mustafa ERKAYAOĞLU for his all recommendations to me regardless of time.

I wish to acknowledge my special thanks to my friends and co-workers. Doğukan GÜNER is the first person to be thanked for his very precious contributions to me and my studies. I am also grateful to my friend Alper KIRMACI for his support and cooperation throughout my thesis. Ceren KARATAŞ BATAN and Enver YILMAZ are also the persons that I want to thank for their continuous supports.

I am beholden to my mother, Füsun KARADENİZ, and my father, Dr. Mehmet KARADENİZ, for their great sacrifices, patience and visions. I also owe to thanks to the rest of my family.

TABLE OF CONTENTS

LIST OF TABLES

TABLES

LIST OF FIGURES

FIGURES

LIST OF SYMBOLS AND ABBREVIATIONS

ABBREVIATONS	DESCRIPTION
AE	Acoustic Emission
BHTV	Borehole Televiewer
C1	Caliper 1
C2	Caliper 2
CBIL	Circumferential Borehole Imaging Tool
DIF	Drilling-Induced Fracture
EMI	Electrical Micro Imager
EMS	Electrical Micro Scanner
ELOT (XLOT)	Extended Leak-off Test
FIT	Formation Integrity Test
FMI	Formation Micro Imager
FMS	Formation Micro Scanner
LOT	Leak-off Test
OBMI	Oil-Based Micro Imager
PIT	Pressure Integrity Test
RAB	Resistivity at Bit
UBI	Ultrasonic Borehole Imager
STAR	Simultaneous Acoustic and Resistivity Tool
R	Borehole Radius
r	Distance from Borehole Center

σ_n	Normal Stress
τ	Shear Stress
S_1/ σ_1	Maximum Principal Stress
S_2/ σ_2	Intermediate Principal Stress
S_3/ σ_3	Minimum Principal Stress
$\sigma_{\theta\theta}$	Tangential Stress
σ_{rr}	Radial Stress
S_{hmax}	Maximum Horizontal Stress
S_{hmin}	Minimum Horizontal Stress
S_v	Vertical Stress
θ	Azimuth Measured from Direction of S_{hmax}
C_0	Compressive Strength
T_0	Tensile Strength
E	Young's Modulus
ν	Poisson's Ratio
ϕ	Internal Friction Angle
θ_b	Angle of Breakout Initiation
ϕ_b	Angle of Half Width of Breakout
W_{BO}	Width of Breakout
r_d	Breakout Depth
P_0	Pore Pressure
ΔP	Difference between the Mud Weight and Pore Pressure

CHAPTER 1

INTRODUCTION

Weight of overlying strata causes natural stresses on rocks defined as in-situ stresses (Amadei & Stephansson, 1997) and when virgin rock is excavated, stress distribution around the rock changes significantly. The stress fields around the rock are called induced stresses. Since magnitudes and orientations of those in-situ and induced stresses are important for the design of underground or surface mines considering economy and safety, knowledge of these stress states is one of the crucial information for mining and geotechnical engineering approaches. However, the measurement of the stress states is challenging as stated by Leeman (1959). The measure of this phenomenon is an imaginary quantity as it is not possible to identify it directly. Although there are indirect methods that might estimate the stresses from the measurement results, they are performed on a solid body. The common features of these techniques are the testing of the rock sample where the behavior is measured in terms of different quantitative properties such as strain, displacement, or hydraulic pressures. These recordings are then analyzed with estimated rock properties and corresponding constitutive rock behavior.

In-situ stresses mainly consist of three components; maximum and minimum horizontal and vertical stresses. The estimation of vertical stress is simply based on the multiplication of the depth of the rock and the unit weight of the rock mass. The defined relationship between vertical and horizontal stresses is represented by a factor, namely “k”. In literature, there is an argument about whether this “k” value is dependent on depth or not. Terzaghi and Richard (1952) claim that “k” is only related to the Poisson’s ratio for rock mass loaded by gravity; $k= \nu/(1-\nu)$. Other researchers argue that “k” is likely to be lower as depth increases (Brown & Hoek, 1978).

Therefore, the estimation of horizontal stresses might be considered more complicated than vertical stresses.

There are various measurement techniques used for the estimation of in-situ stresses, classified in terms of the location they are performed. These techniques might be conducted in boreholes, in drill cores, on rock surfaces, and large-scale geological structures and are defined as strain recovery methods. There are also core discing, acoustic methods in drill cores, overcoring, hydraulic tests on pre-existing fractures, hydraulic fracturing, borehole breakouts in boreholes, jacking and surface relief methods on rock surfaces, earthquake focal mechanism and fault slip analysis in large scale geological structures (Ljunggren et al., 2003). However, there are some difficulties and disadvantages related to these techniques; for example, overcoring and strain relief measurements can be useful only when the measurement is done close to a free surface. In this study, borehole breakouts were used to estimate the in-situ stress of the field. The improvements in borehole imaging technology have made borehole breakouts advantageous in stress estimation by means of time saving and cost as compared to other methods (Lin et al., 2018) because they enable simple and fast measurement by using borehole geometry. Another advantage of this technique is to obtain all breakouts of the borehole at different depths with one measured image. In addition to this, it provides measurement of stresses at great depths with respect to other measurement techniques.

1.1. General Remarks and Definitions

There have been several studies about the investigation of in-situ stress from the borehole failures as elongation in diameter of boreholes and fractures vertically aligned in the borehole surfaces. The studies (Cox, 1970; Bell & Gough, 1979) demonstrated that these elongations (breakouts) and fractures (Drilling-induced fractures) are indicators of the directions of minimum and maximum horizontal principal stresses. In some studies, leak-off tests (LOT) were performed to obtain minimum horizontal stress magnitudes similar to this thesis study (Wiprut et al., 1997;

Addis et al., 1998). To obtain information about the state of the borehole walls, borehole imaging tools like Formation Micro Imager (FMI) are required. Therefore, FMI, breakouts, drilling-induced fractures (DIFs), and LOTs are important definitions for this thesis study.

- FMI is one of the resistivity imaging tools to observe deformations on the borehole walls (Ekstrom et al., 1987).

- Breakout is the borehole failure causing elongations in opposite sides of the borehole resulting from compressive failure due to stress concentration around the borehole after it is drilled.

- DIFs are the borehole failures causing fractures parallel to the borehole axis in opposite sides of the borehole resulting from tensile failure by the stress distribution like in the formation of breakout (Zoback, 2007).

- Leak-off test is one of the pressure integrity tests to obtain minimum formation pressure or minimum horizontal stress magnitude of the field (Addis et al., 1998).

1.2. Problem Statement

In-situ stress magnitude and orientation have an important role in mining applications such as slope stability, selection of support system, cavern stability and others. However, the estimation of the quantity of in-situ stress is challenging and studies related to the determination of in-situ stresses are very limited, in Turkey. Although there is an AE laboratory studies conducted in Turkey, for example, it is possible to find some data of several locations in terms of maximum - minimum horizontal stresses and principal stresses and orientations according to the study (Tuncay et al., 2002), those laboratory studies are all limited information and resource. This study indicated the values of stresses of Ankara and Çayırhan for Ankara district determined from AE rock block tests of the related sites. For Batı Raman site, FMI is also used for determination of stress orientation (Arslan et al., 2007). Nevertheless, there has

been no study on any in-situ data including both magnitude and direction of stresses for Kazan district in Ankara.

1.3. Objective of Study

This study is mainly composed of two parts; the determination of the direction and the magnitude of horizontal principal stresses in Kazan district of Ankara. In the estimation of the stress directions, FMI log of the borehole V040A was interpreted in terms of borehole failures, breakouts and DIFs, as signs for maximum and minimum stress directions. In the second part of the study, the aim was the determination of the magnitude of horizontal stresses numerically and analytically. Horizontal stresses are defined as minimum and maximum stresses; the minimum stresses were estimated by field studies (LOTs), then maximum stresses were found by changing its magnitude iteratively with a known minimum horizontal stress magnitude as inputs of the numerical analyses. Therefore, research objectives of this study are defined as determination of the horizontal stress magnitudes and orientations for Kazan district.

1.4. Research Methodology

This study purposes to determine the maximum and the minimum horizontal stresses in terms of magnitude and orientation. Therefore, this study covers field studies, laboratory experiments, FMI log interpretation, numerical modelling and analytical analyses in the scope. The field studies are leak-off tests and FMI logs; the leak off tests were used to estimate the magnitude of the minimum horizontal stresses in the field and the FMI logs were used to define the borehole failures leading to identify the orientations of those stresses. Laboratory experiments were carried out to identify the mechanical properties of two different rock units, marl and trona, in different intervals of the borehole. Those properties are Young's modulus, Poisson's Ratio, uniaxial compressive strength, tensile strength, cohesion, and internal friction angle for both rock units. After the determination of mechanical properties and utilization of the field study results, 2D numerical analyses of the borehole cross-sections in two rock units were performed by finite difference numerical code FLAC 2D. The simulations of the

borehole cross-section behavior were examined for different maximum and minimum horizontal stress magnitudes with corresponding failures expected. The FLAC 2D run results were compared with analytical solutions to study their compatibilities in the estimation of maximum horizontal stress magnitudes for both rock units.

1.5. Outline of the Thesis

Introduction part of the thesis mentions mainly importance of the in-situ stress and methodology and objective of the thesis. Literature survey chapter gives a brief summary of the studies carried out about this thesis topic. There are explanations of the main points of the study and scope of those studies. The information of the project site and the geology are provided in the FMI log chapter. This chapter also covers the interpretation and results of this logging tool (FMI). Field and laboratory studies chapter include the leak-off test and rock mechanics experiments test results. It also explains the leak-off test with its theory and other available testing methods. In numerical modeling, the results of the models are given and these results are analyzed in terms of depth and width of the breakouts in FLAC 2D. Those results are compared with analytical solutions. Conclusions and recommendations are given in the last chapter of the thesis.

CHAPTER 2

LITERATURE SURVEY

Literature was comprehensively reviewed within the scope of this study and the details are given in this chapter. Theories behind the studies conducted were mentioned such as formation of breakouts and DIFs and their utilizations in the studies.

2.1. Literature Review

Imaging of the borehole walls provides several information such as stratigraphic structures, faults, folds, etc. besides the borehole failures, hence borehole logging plays an important role in geomechanical studies. It is generally a field study of petroleum engineering; beginning with the studies, surface resistivity measurement, done by Conrad Schlumberger (Slb.com, 2019), who is the owner of the company (Schlumberger), the world's first logging company. The first well logging was carried out in the years of 1920's. At later times, dipmeter tools were developed to determine stratigraphic structure in the field (Allaud & Ringot, 1969; Luthi, 2001) and FMI tool is originated from dipmeters depending both on resistivity differences on surfaces (called as four-arm caliper logs). Besides stratigraphic structures, breakouts on wellbore walls were investigated by several researches, (Cox, 1970; Babcock, 1978; Schafer, 1979; Brown et al., 1980; Zoback et al., 1985). DIF's were also studied to determine the relationship between those fractures and the determination of in-situ stresses on constraining the full stress tensor from observations of LOTs (Pendexter & Rohn, 1954; Wiprut et al., 1997; Haimson & Lee, 1995).

2.2. Relative Stress Magnitudes

One of the principal stresses is normal to the other two principal stresses and to the earth's surface. Therefore, in order to obtain the stress state of the field, there are four

parameters required; those are the maximum principal horizontal stress, S_{hmax}, the minimum horizontal stress, S_{hmin}, and the vertical stress S_v, referring to the overburden weight, and one of the orientations of one of the stresses. This orientation is generally introduced to be the S_{hmax} azimuth. Anderson was the researcher to state that the magnitudes of the least (S_3), intermediate (S_2), and greatest principal stress (S_1) as S_{hmax}, S_{hmin}, S_v should be considered (Anderson, 1951).

The Anderson classification shows the relation between faulting regimes and relative stress magnitudes. By this scheme, normal faulting regime is expected under the condition, S_v ($S_v = S_1$) is greater than the horizontal stresses. If the magnitude of S_{hmax} is greater than S_v ($S_v=S_2$) with sufficient difference of S_{hmax} and S_{hmin}, strike-slip faulting regime may occur as an intermediate stress state. On the contrary to normal faulting regime, if S_v ($S_v=S_3$) is less than both horizontal stresses, and S_{hmax} is greater enough than S_v, reverse faulting can be observed in the field. However, this theory is constrained by the strength of the rocks exposed to those stress states; compressive and tensile strength of the rocks. As stated by Zoback (2007), upper limit of in-situ stress magnitudes is the frictional strength of previously faulted rock. Therefore, the state of these stresses is important in aspect of possible faulting regimes. In the following parts, the relation between these stresses and strengths of the rock to estimate the principal stresses are explained.

2.3. Measuring In-situ Stress

In order to find the stress states on field, there are some steps that follow each other,

- The magnitude of S_v can be estimated by the rock density from the surface to the corresponding depth and gravitational acceleration, and S_v is assumed to be a principal stress.
- The borehole observations and earthquake focal mechanisms provide the orientations of S_{hmax} and S_{hmin}.
- The magnitude of S_{hmin} is attained by mini-fracs and pressure integrity tests.

- The remaining parameter is only the magnitude of S_{hmax} to estimate the full stress tensor for the field studied. Analyses of the borehole failures determined in the borehole observations provide this S_{hmax} estimation.

In the Cajon Pass and KTB (Kontinentale Tiefbohrprogramm der Bundesrupublik Deutchland) projects, this progress method was first applied for the estimation of those three principal stresses (Zoback & Healy, 1992; Zoback et al., 1993, Zoback & Harjes, 1997). This strategy is called an integrated stress measurement strategy due to the use of wide range of observations (Zoback, 2007).

In Cajon pass study, stress-induced borehole breakouts were used for the measurement of in-situ stress orientation and magnitude from depths 0.9-3.5 km, and using the hydraulic fracturing in Southern California. The results were also analyzed for faulting mechanism. On the other hand, in KTB project, researchers estimated the magnitude and orientation of in-situ stress for 6 km depth in Southern Germany. Wiprut et al. (1997) investigated to constrain the full stress tensor using both borehole failures and pressure integrity tests in the estimation with the same strategy in Norway.

In those studies, the S_{hmin} was found by using pressure integrity tests results and the borehole failures were determined by ultrasonic or electrical imaging tools in order to identify what kind of borehole failures occur and where they are located in terms of azimuth for the direction of the horizontal stresses. The other parameters required were the strength values of the rock units in the field; hence the borehole failures depend on the compressive and the tensile strength of the rock.

Stress-induced wellbore breakouts are viable methods for the estimation of stress direction and magnitude according to those studies. In this manner, breakouts are one of the important indicators with a characteristic compressive failure process that occurs when the tangential stresses exceed the compressive strength of the rock.

This results in that the rock around a part of the borehole yields in compression (Bell & Gough, 1983; Zoback et al., 1985; Bell, 1989). For the straightforward instance of a vertical hole when S_v is a principal stress, this prompts stress-induced borehole

breakouts that structure at the azimuth of the S_{hmin}. Hence, they are useful in estimation of horizontal stress direction. The researches have demonstrated that the orientations are uniform along the borehole, which means they do not depend on lithology and age (Plumb & Cox, 1987; Castillo & Zoback, 1994).

The other borehole failure type, also important indicator to define stress direction, is DIF (Moos & Zoback, 1990; Brudy & Zoback, 1999). On the contrary to breakouts, DIFs are tensile failure process that observed when the tangential stress exceeds the tensile strength of the rock. These fractures are seen in the azimuth of the S_{hmax}. It was shown that they can present a good sign in estimation of stress direction (Wiprut et al., 1997).

2.4. Stress Concentration around a Borehole

Drilling a borehole is the removal of material, therefore, the far-field stresses are not supported due to the formation of a free surface in borehole walls. This refers to the stress concentrations around borehole walls as induced stresses. As shown in Figure 1, these stresses follow a bended path to be parallel and perpendicular actually in far-field zones. The stress concentration around a borehole was first defined by the Kirsch equations with the assumptions that the medium is isotropic and elastic, and a vertical borehole is drilled parallel to the vertical principal stress (Kirsch, 1898; Jaeger & Cook, 1979). Those paths or trajectories, in Figure 2.1, illustrate compressive and tensile stresses at the azimuths of Shmin and Shmax, respectively. At the azimuth of Shmin, the trajectory lines accumulate on the top part of the circular section, which indicates compression in this zone. At the azimuth of Shmax, the lines extend at the sides of the section, so that tensile stress is represented.

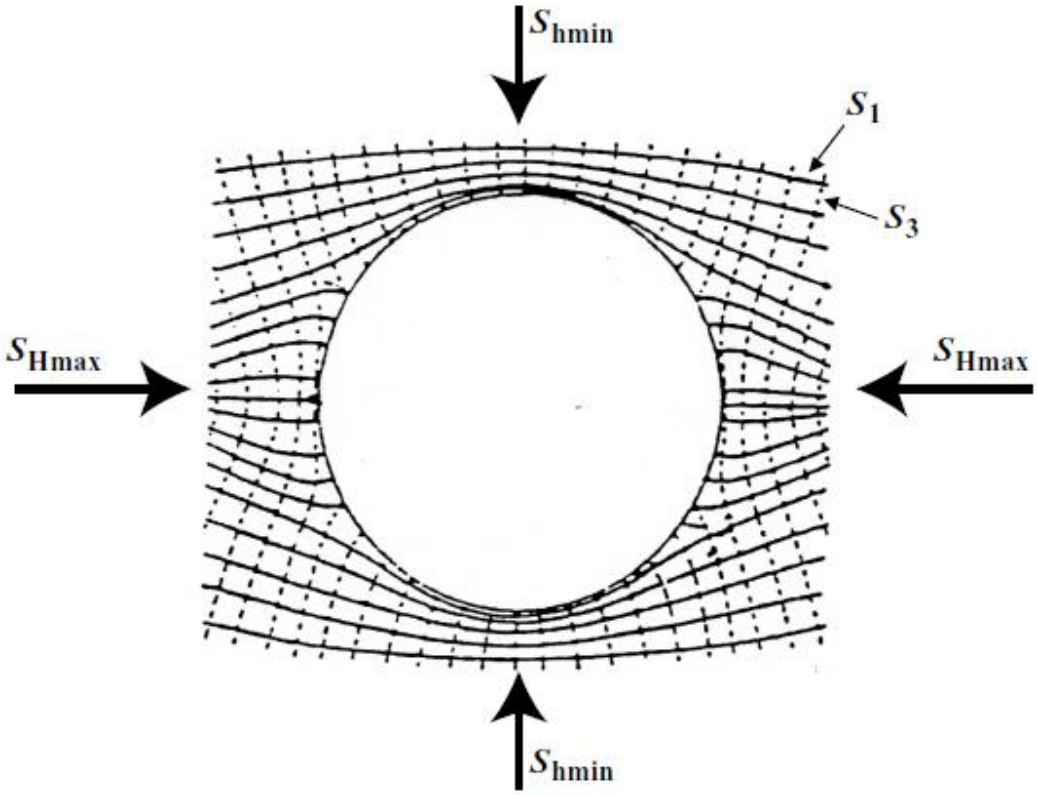

Figure 2-1: Schematic view of principal stress trajectories around a circular opening based on the Kirsch solutions

The stresses due to the removal of material and induced stresses are the effective stresses around a borehole, those stress components are radial, circumferential, and tangential shear stresses. The mathematical notations of those stresses by the Kirsch equations are as follows.

$$\sigma_{rr} = \frac{1}{2}(S_{h\max} + S_{h\min} - 2P_0)(1 - \frac{R^2}{r^2}) + \frac{1}{2}(S_{h\max} - S_{h\min})(1 - \frac{4R^2}{r^2} + \frac{3R^4}{r^4})\cos 2\theta + \frac{P_0 R^2}{r^2} \quad (1)$$

$$\sigma_{\theta\theta} = \frac{1}{2}(S_{h\max} + S_{h\min} - 2P_0)(1 + \frac{R^2}{r^2}) - \frac{1}{2}(S_{h\max} - S_{h\min})(1 + \frac{3R^4}{r^4})\cos 2\theta - \frac{P_0 R^2}{r^2} - \sigma^{\Delta T} \quad (2)$$

$$\tau_{r\theta} = \frac{1}{2}(S_{h\max} + S_{h\min})(1 + \frac{2R^2}{r^2} - \frac{3R^4}{r^4})\sin 2\theta \quad (3)$$

These equations are defined in terms of S_{hmax}, S_{hmin}, the borehole radius (R), the distance from the borehole center (r), the difference between the mud weight and pore pressure (P0) in the borehole (ΔP), and the azimuth measured from the direction of S_{hmax} (θ). As it can be seen from Equations (1, 2, and 3), the stress concentration change has a function that depends on location in terms of distance from the borehole wall and azimuth from the direction of S_{hmax}. Radial stress is the stress perpendicular to the borehole wall, while circumferential stress is perpendicular to radial stress. The concentrated stress zone is symmetric regarding the horizontal principal stresses. In the direction of S_{hmax}, $\sigma_{\theta\theta}$ behaves compressive to the north and the south direction or called as at the azimuth of S_{hmin}. In contrast, $\sigma_{\theta\theta}$ is tensile to the east and the west direction at the azimuth of S_{hmax}. The equations do not depend on the Young's modulus, this means that the stress concentration around a borehole does not show any difference in distinct formations.

Based on the magnitude of the circumferential stress, the compressive or the tensile failures are likely to be observed in the zones of maximum and minimum tangential stresses at the azimuth of S_{hmin} and S_{hmax}, respectively, and depend on the compressive and the tensile strength of the rock (Zoback, 2007).

There are two important terms, previously defined in the first chapter, those are breakouts and DIFs. By simplifying the Equations (1-3), it can be envisioned that they are good indicators of in-situ stress directions. Where r is equal to R, the effective tangential (or also called as effective hoop stress) and the radial stress at the boundary of the borehole surface can be given by Equations (4-5).

$$\sigma_{\theta\theta} = S_{h\min} + S_{h\max} - 2(S_{h\max} - S_{h\min})\cos 2\theta - 2P_0 - \Delta P - \sigma^{\Delta T} \tag{4}$$

$$\sigma_{rr} = \Delta P \tag{5}$$

The stress parallel to the borehole axis is given by Equation 6.

$$\sigma_{zz} = S_v - 2\nu(S_{h\max} - S_{h\min})\cos 2\theta - P_0 - \sigma^{\Delta T} \tag{6}$$

By the assumption that θ is measured from the azimuth of S_{hmax}, the effective hoop stress can be defined as in Equation 7 at θ = 0° and θ = 180°, where it is the minimum compression around the borehole.

$$\sigma_{\theta\theta}^{\min} = 3S_{h\min} - S_{h\max} - 2P_0 - \Delta P - \sigma^{\Delta T} \quad (7)$$

Likewise, for the zone of maximum compression, the effective hoop stress can be expressed as given in Equation 8 at θ = 90° and θ = 270°

$$\sigma_{\theta\theta}^{\max} = 3S_{h\max} - S_{h\min} - 2P_0 - \Delta P - \sigma^{\Delta T} \quad (8)$$

The difference of those two effective hoop stresses give the amplitude of sinusoidal change around the borehole in Equation 9, it supports the indication of in-situ stress directions by borehole failures.

$$\sigma_{\theta\theta}^{\max} - \sigma_{\theta\theta}^{\min} = 4(S_{h\max} - S_{h\min}) \quad (9)$$

2.5. Compressive and Tensile Failures in Vertical Holes

The three principal stresses, described by Equation (4-6), are the stresses that the borehole wall rock is exposed to. If the rock strength is not sufficient to resist those stresses, the rock will yield. Depending on the states of stresses, whether it is compressive or tensile, the expected borehole failures changes; these might be breakout or DIFs.

2.5.1. Breakouts

As shown in Figure 2.2, the largest compressive stress is observed at the azimuth of S_{hmin} due to the stress concentration at the borehole walls. At this point of the largest compressive stress state, the rock might be expected to fail, if these stresses exceed the compressive strength of the rock. This failure type is called breakout (Zoback, 2007). Breakout is the compressive failure zone in the borehole walls. Therefore, by the assumption of θ is azimuth measured from the direction of S_{hmax}, the breakouts are observed at θ = 90° and θ = 270° (Figure 2.2).

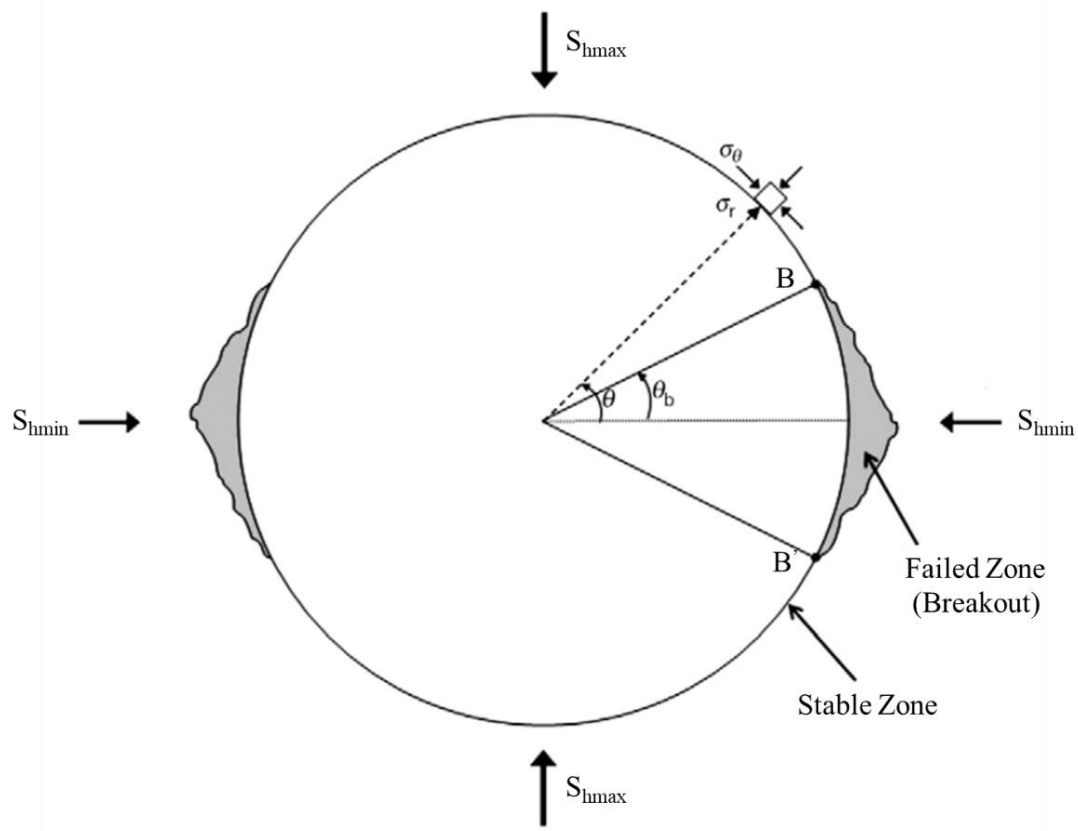

Figure 2-2: Representative view of a borehole breakout (Haimson et al., 2010)

As indicated in Figure 2.2, the formed breakout represents a dog-ear shaped failure zone. This zone actually has two geometric components; those are depth and width in terms of radius and angle, respectively. After the initial formation of the breakout, the diameter of the borehole extends symmetrically in dog-ear shaped zones at the azimuth of S_{hmin}. This refers to the increase in the depth of the diameter of the borehole at that azimuth. The other one is an angular extension in width, the arc of the borehole in failed zone gives an angle measured from the center of the borehole.

However, one of those two components might change with time after initial formation. According to Zoback et al. (1985), the induced stress at the borehole surface lead to breakout and tends to deepen until the growth of breakout would stabilize. The following studies promoted this idea by laboratory studies and other field studies (Zheng et al., 1989). Figure 2.3 shows the image of a breakout observed in laboratory

experiments (Haimson & Herrick, 1989), theoretical representation of a breakout growth by Zoback et al. (1985) and laboratory image by Haimson and Herrick (1989) are illustrated at the left and right side of Figure 2.3, respectively. Therefore, it is concluded that while breakout growth is getting deeper, the angular width of this dog-ear shape does not change.

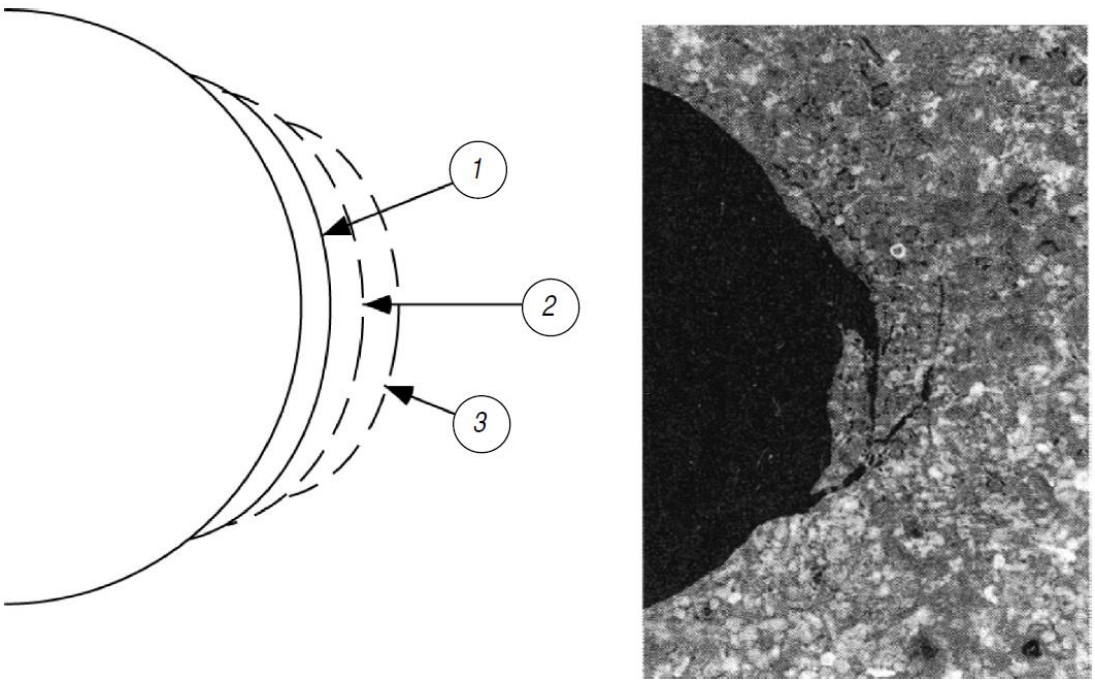

Figure 2-3: Theoretical illustration of a breakout evolution by Zoback et al., (1985) at the left side, and Laboratory image of a breakout evolution by Haimson and Herrick (1989) at the right side

This growing progress was also studied by Zheng et al. (1989), as the researchers tried to investigate the model analytically but the proposed breakout shapes were not seen as actual breakouts in the boreholes in general. The actual ones have a relatively flat-bottomed shape. The reason of this concept was the absorption of strain energy through inelastic deformation with the beginning of the failure of the rock. Besides, there are some parameters that affect the formation of breakouts considering borehole stability; those might be affected by rock strength anisotropy, the relation between mud chemistry, rock strength and borehole stability, and mud penetration into fractured rock around the borehole (Zoback, 2007).

Furthermore, the stabilization of the breakouts in terms of angular width aided researchers to establish a correlation between this angular width and the stress change in the field (Barton et al., 1988). A relation was developed to estimate S_{hmax} depending on Kirsch equations as the width does not change during the evolution of the breakout growth. In this relation, the equilibrium of stress concentration with the strength of the rock at the edge of a dog-ear shape was utilized as a stable condition in Equation 10, and also as represented in Figure 2.4.

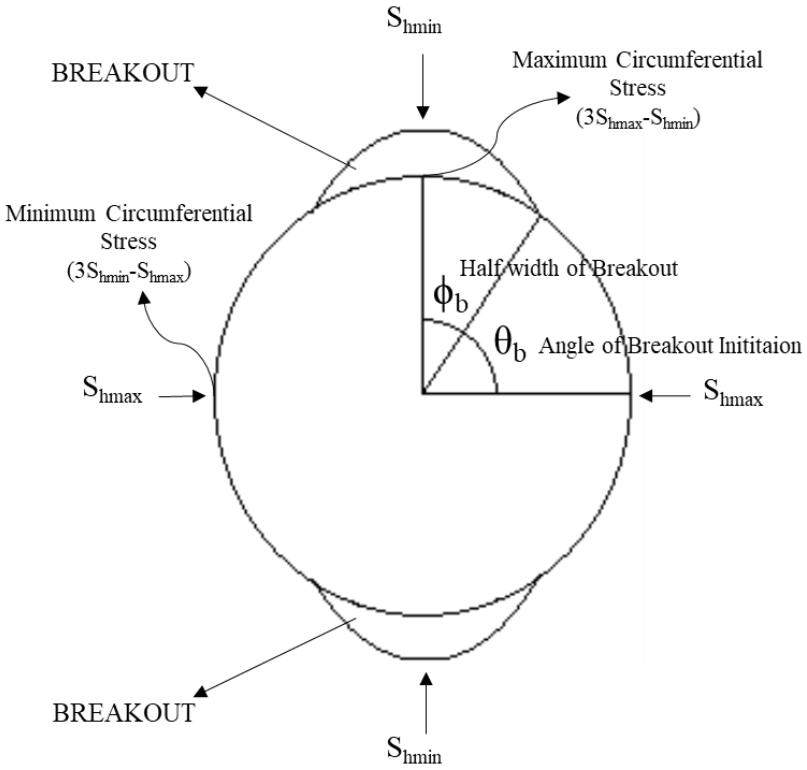

Figure 2-4: A schematic view of a breakout with half width and initiation angle

$$S_{hmax} = \frac{(C_0 + \Delta P + 2P)}{(1 - 2\cos 2\theta_b)} - S_{hmin} \frac{(1 + 2\cos 2\theta_b)}{(1 - 2\cos 2\theta_b)} \qquad (10)$$

In this equation, C_0 is the compressive strength of the rock, ΔP is the difference between the mud weight in the borehole and the pore pressure (P). θ_b is the angle between the edge of a breakout initiated and the azimuth of S_{hmax}. In case the half

width of a breakout is defined as angle ϕ_b, as indicated in Figure 2.4, it might be calculated by Equation 11. Besides, the breakout opening angle is defined as twice the half width of a breakout, called W_{BO}.

$$\phi_b = \frac{\pi}{2} - \theta_b \tag{11}$$

This theory only uses the breakout width to estimate S_{hmax}, it is not interested in depth of breakout. Hence, according to literature studied, the analytical solution of the maximum stress estimation is accomplished by not taking into account time-dependent failure or propagation of breakout.

2.5.2. Drilling Induced Fractures

In parallel to the breakouts, DIFs are also borehole failures due to induced stresses around the borehole walls. As indicated in the breakout section, after drilling, the stress concentration might create tensional stresses, if the stress concentrated exceeds the tensile strength of the rock. Drilling-induced fractures or drilling-induced tensile fractures are observed at these parts of the borehole walls at the azimuth of S_{hmax}, orthogonal to the breakouts, if they both exist at the same cross-section of the borehole.

On the contrary to the breakouts, DIFs do not propagate more than one cm from the borehole wall, perpendicular to the borehole axis. Therefore, if the mud weight does not exceed S_3, formation of DIFs will not result in the propagation of hydraulic fracturing. Since they do not have any sufficient distance perpendicular to the borehole axis, they do not have a significant effect on drilling (Zoback, 2007).

It has to be seen on both opposite sides of the borehole in order to be considered as DIFs parallel to the axis of the boreholes. Since they are observed at the azimuth of S_{hmax}, they might be considered as the indicator of S_{hmax}. However, occurrence of one of the breakouts or DIFs can be adequate to estimate the stress directions due to the orthogonality of S_{hmax} and S_{hmin}, Figure 2.5. The main points in the formation of DIFs

are the large difference between S_{hmax} and S_{hmin}, and the one principal stress is parallel to the borehole axis.

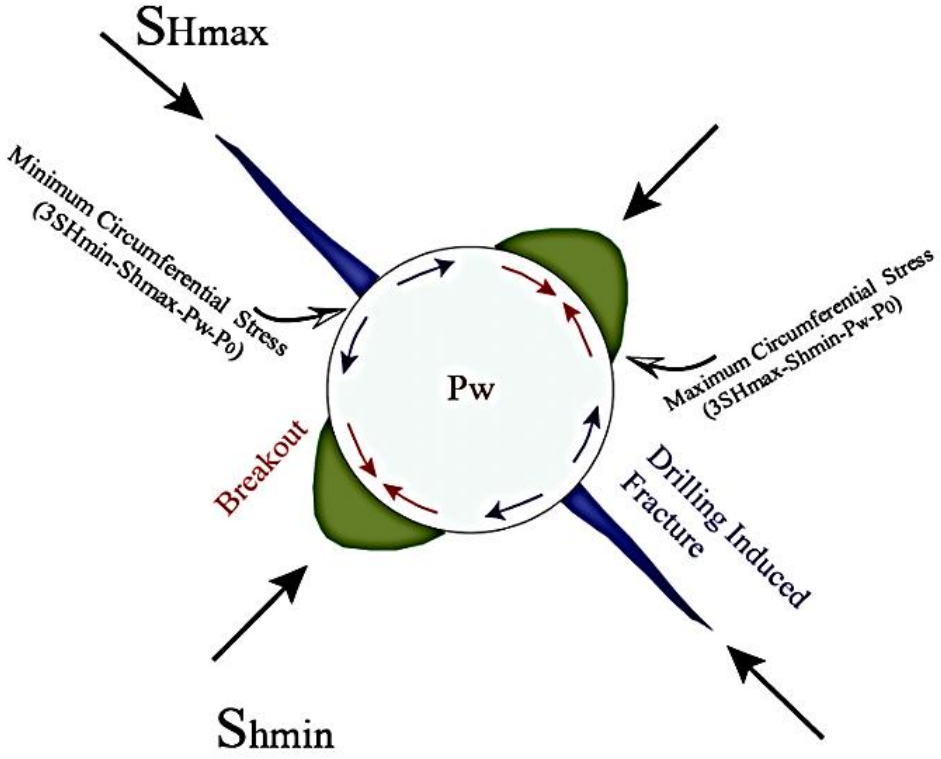

Figure 2-5: Schematic view of breakout and DIFs with the minimum and maximum horizontal stresses (Fjaer et al., 1992)

Those breakouts and DIFs are observed by the borehole imaging tools, utilizing different physical properties of the borehole surface such as ultrasonic and resistivity imaging tools. These tools and their interpretation will be explained in the FMI Log chapter.

2.6. Failure Criteria

There are different failure criteria developed to define the strength of the rock under different stress conditions depending on conducted laboratory tests. Due to the highly concentrated stress around the boreholes at depth, the estimation of in-situ stress is more important than the determination of the value of rock strength (Zoback, 2007). Therefore, it is essential to choose the proper failure criterion for the mechanical

analysis of rock. Failure criteria, will be discussed in this chapter, are Mohr-Coulomb, Hoek-Brown, Modified Lade, Drucker-Prager, and Mogi-Coulomb criteria.

2.6.1. Mohr-Coulomb Criterion

In this criterion, it is stated that there is a relation between the normal stress (σ_n) and shear stress (τ), depending on the cohesion (c) and internal friction angle (ϕ), Equation 12.

$$|\tau| = S_0 + \mu_i \sigma_n \tag{12}$$

where S_0 is cohesion, and μ_i is coefficient of internal friction.

If this relation is converted to principal stresses, it would be represented as in Equation 13. The intermediate principal stress is assumed to have no effect on failure (Colmenares & Zoback, 2002). The affecting parameters are only the maximum and the minimum principal stresses (σ_1, σ_3) with the uniaxial compressive strength (C_0) and the internal friction angle (ϕ). The assumption is that intermediate principal stress (σ_2) and σ_3 are equal to each other, σ_1 is greater than σ_2 and σ_3. Linearized Mohr-Coulomb failure criterion might be considered to be a shear failure criterion.

$$\sigma_1 = C_0 + q\sigma_3 \tag{13}$$

$$q = \left[\left(\mu_i^2 + 1 \right)^{\frac{1}{2}} + \mu_i \right]^2 = \tan^2 \left(\frac{\pi}{4} + \frac{\phi}{2} \right) \tag{14}$$

$$\phi = \tan^{-1}(\mu_i) \tag{15}$$

2.6.2. Hoek-Brown Criteria

This is an empirical criterion, which uses the uniaxial compressive strength of the intact rock to scale the material, explained by two dimensionless strength parameters (m and s). According to this criterion, there is a relation between σ_1 and σ_3 depending on the extensive experimental data by Hoek and Brown. This relation is as in Equation 16;

$$\sigma_1 = \sigma_3 + C_0 \left(m_b \frac{\sigma_3}{C_0} + s \right)^a \quad (16)$$

The parameters "m_b" and "s" are constants, while "m_b" is related to the rock type, "s" is about the characteristics of the rock mass (Hoek & Brown, 1980; Hoek & Brown, 1997; Hoek et al., 2002). There are different rock classes studied to assign "m" value, for example, 5 < m < 8 for carbonate rocks (dolomite, limestone, etc.). "s" value is assigned based on the condition of the rock in terms of similarity to intact rock or not, for example, "s" is equal to 1 for intact rock, but it is 0 for a rock aggregate (Colmenares & Zoback, 2002). This failure criterion is mainly used for the estimation of the rock mass strength.

2.6.3. Modified Lade Criterion

Modified Lade criterion is a frictional material criterion without effective cohesion, developed for soil materials (Ewy, 1999). It is a three-dimensional failure criterion with a curved failure envelope, represented by Equation 17 as follows.

$$\left(\frac{I_1^3}{I_3} - 27 \right) \left(\frac{I_1}{p_a} \right)^{m'} = \eta_1 \quad (17)$$

I_1 and I_3 are the first and the third stress tensor invariants.

$$I_1 = S_1 + S_2 + S_3 \quad (18)$$

$$I_3 = S_1.S_2.S_3 \quad (19)$$

where p_a is atmospheric pressure, and m' and η_1 are the material constants. S is related to the cohesion of the rock. This criterion is used to estimate strengthening effect depending on the increasing intermediate principal stress σ2.

2.6.4. Drucker-Prager Criterion

It was mainly developed for soil materials, the extended version of von Mises yield criterion (Drucker & Prager, 1952). It is described as in Equation 20, where J_1 and J_2 are the stress invariants, and α and k are the material constants.

$$J_2^{1/2} = k + \alpha J_1 \tag{20}$$

α and k are related to the internal friction angle and the cohesion of the material, respectively. In comparison to Mohr-Coulomb failure criterion, if α is greater than the upper bound of the geometric representation of the Drucker-Prager criterion, C_0 and μ_i cannot be found. If those two parameters are not necessary to be found out, the Drucker-Prager failure criterion can be applied in each case (Colmenares & Zoback, 2002).

2.6.5. Mogi-Coulomb Criterion

As it is stated by Al-Ajimi and Zimmerman (2005), the linear version of the Mogi criterion is “Mogi-Coulomb” criterion. According to these researchers, it is also thought that Coulomb failure criterion is a special condition of the more general linear Mogi failure criterion, where σ_2 is equal to σ_3. Therefore, it is actually used for polyaxial failure conditions.

It is described as in Equation 21 in terms of the first and second stress invariants I_1 and I_2.

$$(I_1^2 - 3I_2)^{1/2} = a' + b'(I_1 - \sigma_2 - 2P_0) \tag{21}$$

where

$$I_1 = \sigma_1 + \sigma_2 + \sigma_3 \tag{22}$$

$$I_2 = \sigma_1\sigma_2 + \sigma_2\sigma_3 + \sigma_1\sigma_3 \tag{23}$$

$$a' = 2c\cos\phi \tag{24}$$

$$b' = \sin\phi \tag{25}$$

This criterion can also be applied in true-triaxial conditions as by the Mohr-Coulomb criterion to have an advantage of besides the polyaxial conditions.

High tangential stresses with zero radial stresses are the conditions that the rock is exposed to, where it is close to the stress-free borehole walls. Likewise, in a uniaxial and triaxial compression under very low confining pressure condition, the rock close to cylindrical surface is subjected to high stress parallel to the surface, which means extensile splitting is expected in the rock parallel to the loading direction (Wawersik & Fairhurst, 1970; Gallagher et al., 1974; Paterson, 1978, Zheng et al., 1989). By higher confining stresses, shear failure takes place instead of extensile splitting. Loading is mainly unconfined plane strain adjacent to the stress-free surface of the borehole; high tangential stress and zero radial stress. In these locations, away from the borehole boundaries, the confinement is getting higher due to the increasing radial stresses, hence, the failure is expected to be a shear failure. Furthermore, Colmenares and Zoback (2012) investigated the failure criteria for different rock types and presented that one of those criteria would give the best results for different rock types such as the modified Lade criterion is the most suitable one for dolomite and limestone samples. However, Zoback (2007) states that since the rock strength is quite complex, it is difficult to make a choice in the characterization of rock strength with those criteria. In addition, it was stated that in the application of the borehole stability problems, the Mohr-Coulomb or the Hoek-Brown criteria gives more reliable yielding results in relatively strong rocks. Nevertheless, the Mohr-Coulomb failure criterion is considered to be more practical since the Hoek-Brown criteria uses the parameter of m, which is rarely measured.

In the view of such information, Mohr-Coulomb failure criterion was preferred to be used in numerical analysis for this study.

CHAPTER 3

FMI LOG

In order to obtain the information of the borehole failures; breakouts and DIFs, borehole imaging tools are required. These tools provide images of the borehole surfaces and these images might be created based on different physical properties. Imaging tools generally are classified as resistivity and acoustic based imaging tools.

An image of the borehole wall from resistivity contrasts is provided by resistivity imaging tools (Ekstrom et al., 1987), they have resistivity buttons on their pads to allow the current transmitting to create an image from the electrical conductivity difference of the surface that they touch. Some of the available resistivity imaging tools are the Formation Micro Imager (FMI), the Formation Micro Scanner (FMS), Oil-Based Micro Imager (OBMI), Electrical Micro Scanner (EMS), Electrical Micro Imager (EMI). In addition to those ones, logging while drilling or measurement while drilling tools are also resistivity-based imaging tools; such as the Resistivity at Bit (RAB) (Tingay et al., 2008). In this study, the image of the borehole was obtained by FMI.

On the other hand, acoustic imaging tools have a rotating piezoelectric transducer to produce a high frequency sonic pulse towards the borehole surface (Asquith et al., 2004). Then, the acoustic tool records the total travel time of the sonic pulse with the return echo amplitude. Those recorded time and reflected amplitude are measured for each azimuth multiple times for a given depth. While this return echo amplitude is used in the process of the image of the borehole surface reflectance, travel time is needed to determine the instantaneous borehole radius. There are different types of acoustic imaging tools; such as the Borehole Televiewer (BHTV), Ultrasonic

Borehole Imager (UBI), Simultaneous Acoustic and Resistivity tool (STAR), and Circumferential Borehole Imaging Log (CBIL).

3.1. FMI Log Interpretation

Four-arm dipmeters were used to estimate the orientation of the borehole elongation in several studies (Bell & Gough, 1979; Cox, 1983; Gough et al., 1983; Fordjor et al., 1983). The breakouts and DIFs were recorded in these studies using the theory explained in the previous chapter. The dipmeter used in these studies is an old version of resistivity logging tool with four pad type electrodes orthogonally placed.

Likewise, FMI tools create images of the borehole walls depending on resistivity contrast; they are new types of dipmeter tools with the same working principle with four caliper arms. These borehole imaging tools are to make measurements on strikes and dips of bedding planes, fractures, folds, faults, and stratigraphic information; they have electrodes on their pads (Plumb & Hickman, 1985).

This tool touches the borehole surface by the mounted pads on four arms, the pads (yellow parts in Figure 3.1) measure the electrical conductivity of borehole surface by current transmit. The controllable normal force is applied to the pads to provide contact between the borehole surface and the pads.

Figure 3-1: FMI tool with four pads in a borehole (Schlumberger, 2018)

FMI log provides two outputs for two different purposes, resistivity image and caliper logs. Resistivity images are used to obtain information about the lithologic contacts,

foliation, fractures, folds, stratigraphy, dip, and strike of bedding planes in the logged borehole, while caliper logs give the information of change in the cross-section of the borehole in terms of perimeter at any given depth, Figure 3.2.

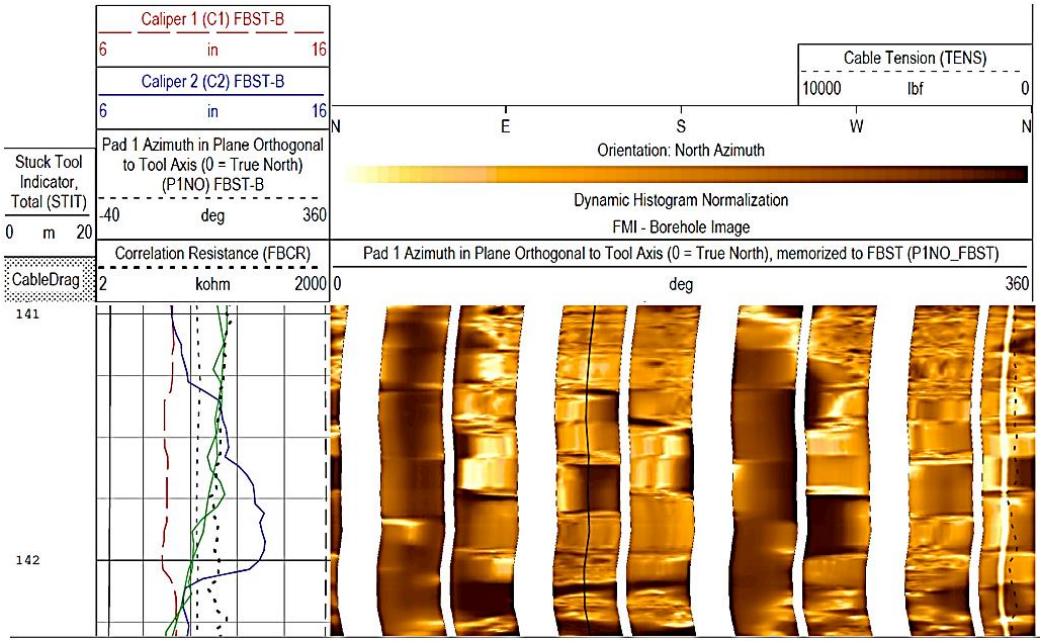

Figure 3-2: An image of FMI log with caliper log (Left side) and resistivity image (Right side) for the interval of 141 to 142.5 m

3.1.1. Reading of Caliper Logs

The pads, located at an angle of 90° to each other, are numbered from 1 to 4; the first and the third ones are one pair, and the other second and fourth ones are the other pairs (also called as caliper pairs). While those pads measure the conductivity of the surface to create the resistivity image, the distance of the opposite caliper pads, or the distance between one caliper pairs are measured and recorded simultaneously to acquire the diametric change in the borehole at a given depth.

The azimuth of the pad, numbered as 1, is continuously known as it is the reference pad for the remaining three pads. Therefore, the azimuthal locations of all pads are identified by the reference pad (Zoback, 2007).

For this study, there are two important indicative borehole failures, breakouts and DIFs to estimate the direction of the horizontal principal stresses. DIFs are not obtained by analyzing the caliper logs since they are not resulting in the extension of the diameter of the borehole. As previously mentioned, since they do not propagate perpendicular to the borehole axis and the fractures do not have significant width, the mounted pads just pass over those fractures. Hence, they cannot be noticed by looking at the caliper movements. However, the caliper logs are required to observe the existence of the borehole breakouts.

In caliper logs, as it can be seen from Figure 3.2, there are two lines colored as red and blue. Red line represents the caliper 1 (C1), the distance between the pad 1 and 3, while blue line shows the caliper 2 (C2), the distance between the pad 2 and 4. As indicated at the top of scaled caliper logs, the lines might go from 6 in to 16 in, hence, the measured distance of those lines are understood from where they are going on this scale.

If both lines are going on top of each other, this means that the distances between the opposite pads are equal to each other, and if this distance is equal to the bit-size, or diameter of the borehole, this shows that there is no failure around the borehole. The borehole breakouts are the enlargements caused by the induced stresses at the azimuth of S_{hmin}, 180° apart in the opposite side of the borehole. By the existence of the borehole breakout at a given depth, one of the lines, C1 or C2, moves away from the other ones, depending on which of the caliper pairs fall into the failed part of the borehole. Therefore, by the assumption of C1 falling into the breakout, when C1 line measures greater distance than the diameter as expected distance, C2 shows the distance equal to the diameter. Nevertheless, this caliper difference is not adequate to deduce whether there is a borehole breakout or not. The resistivity image should also be checked for the same interval.

On the other hand, while FMI log outputs are analyzed for these failures, there are different borehole failure conditions that cause misinterpretation. This means that

some borehole failures might be supposed to be the borehole breakouts. These failures are washouts and key-seats; they are also failures leading to enlargements in the borehole. The main difference is that breakout is an axisymmetric failure, but washouts and key-seats are asymmetric ones. Expansion throughout the borehole diameter is called washout, while enlargement in one side of the borehole refers to key-seat. It is considered that key-seats arise from rubbing of pipe, but there is no exact reason for the formation of washouts. Therefore, both washout and key-seat are not indications of horizontal stresses.

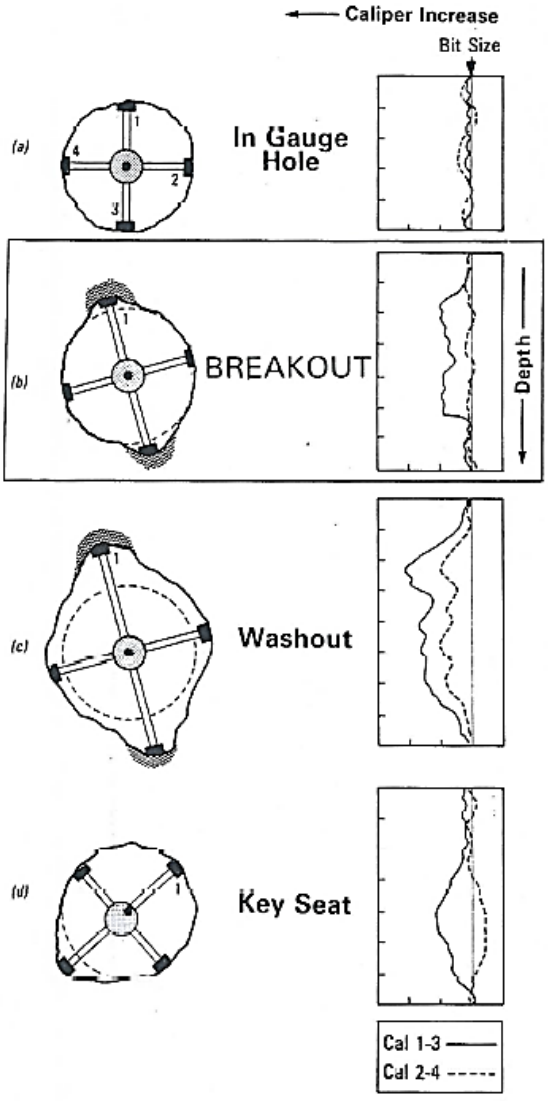

Figure 3-3: Caliper Logs and Borehole Geometries (Plumb & Hickman, 1985)

Plumb and Hickman (1985) stated some straightforward prerequisites to interpret the caliper logs for the analysis of those failures. In key-seat, one of the lines, C1 or C2 moves away from the other ones as it is observed in the breakout since one of the pads fall into the failed section of the rock. Therefore, although there is not a symmetric failure like a breakout, it might be considered as a breakout by just looking at the caliper logs. In order to differentiate those two failures, the resistivity image shows whether there is a symmetric failure or not (key-seat or breakout), Figure 3.3.

The identification of the washout is quite less complex because both of the caliper lines do not follow the bit-size line at the same time, Figure 3.4. This gives the information of the continuous enlargement throughout the borehole surface at a given depth. In this case, the resistivity image is not needed to be analyzed. In addition to those criteria, the reference pad, providing azimuthal location, does not rotate in breakout zones as both opposite pads fall into the zones; however, the rotation is continuous in case of washout and key-seats.

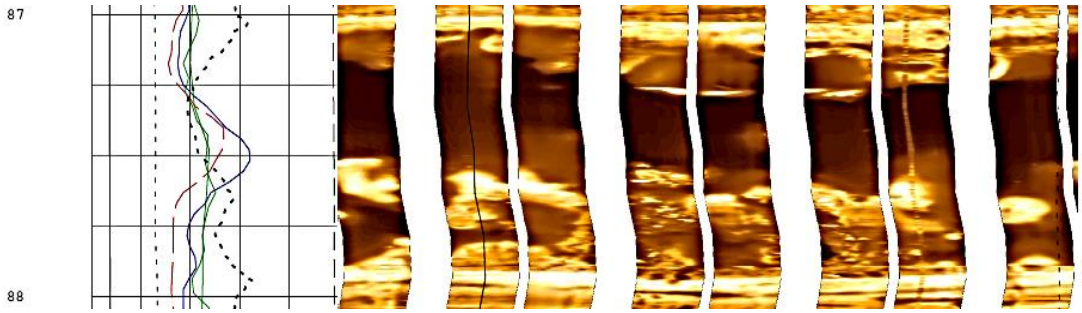

Figure 3-4: A typical washout from FMI Interpretation (87.00 m to 87.50 m of interval)

3.1.2. Reading of Resistivity Image

Resistivity images are high-resolution pictures of the borehole surfaces, created depending on resistivity differences. Therefore, they provide the direct analysis of breakouts and DIFs. In resistivity images, failures are noticed by darkness zones, referring to high conductivity zones; the pads read lower resistivity since they do not touch the formation, while the pads mounted are run into the failure zones. The mud diffuses in these fractures and spalling zones; therefore, it forms different resistivity

surfaces on the borehole with greater conductivity; this can also be considered as poor contact between the borehole wall and the pads mounted.

The key points for the identification of borehole breakouts and DIFs are darkness zones and their symmetry. As mentioned in the previous section, washouts and key-seats might exist, the resistivity image helps to differentiate them by presenting symmetrical darkness bands.

In resistivity images, the breakouts are the spalling zones that are conductive and poorly resolved since they cause poor contact in between the tool pads and the borehole surface due to the resistivity of the conductive drilling mud rather than the formation. Nevertheless, the breakouts are resistive in images rather than conductive (Tingay et al., 2008).

On the other hand, DIFs, cannot be observed from caliper logs and can only be acquired by resistivity image logs. The main point in analysis of DIFs in the resistivity image is again the symmetry of the fractures seen. Due to leaked drilling mud, they are seen as thin conductive fractures in the images. The important criteria for the interpretation of DIFs are that they have to be observed at opposite sides of the borehole, 180° apart, and they have to be seen as parallel or slightly inclined to the borehole axis in vertical boreholes in spite of the natural fractures, Figure 3.5.

The azimuths of noticed breakouts and DIFs are identified by where they are located in the resistivity images. As it can be seen in Figure 3.5, the image is spread out from 0° to 360°, or from north to south. If a breakout or a DIF is observed at 20°, it has to be at 200°, and this means that the orientation of S_{hmin} or S_{hmax}, depending on breakout or DIF, is in the direction of N20E, or S20W. However, this is the local orientation of the horizontal stress, it does not give the mean direction. To comment on the mean direction of those horizontal stresses, all breakouts and DIFs data gathered are plotted on a rose diagram or any other statistical tool in terms of the frequency and the azimuths of those indicative failures.

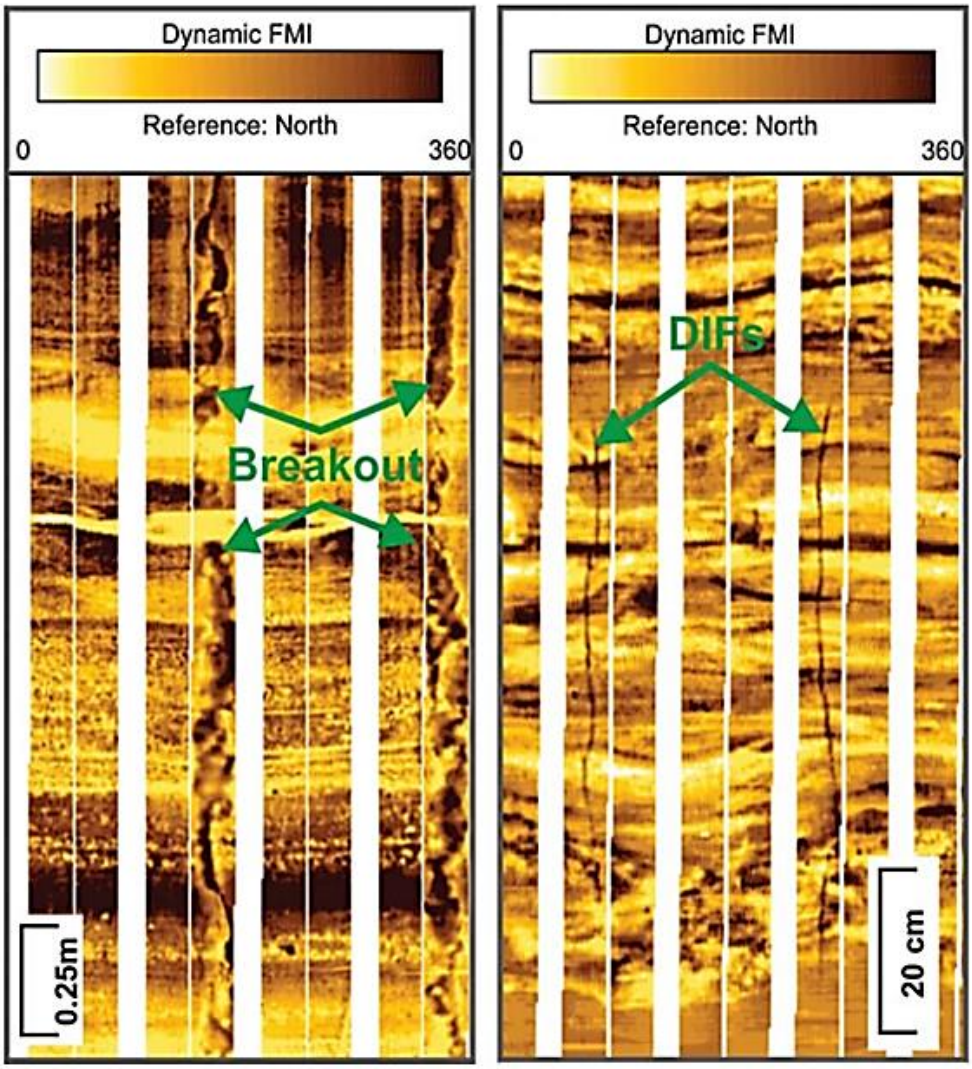

Figure 3-5: Typical views of Breakouts and DIFs on FMI log (Rajabi et al., 2016)

3.2. The Project Site and The Geology

The project area used in this study is located 20 km northwest of Kazan in Ankara. The field is characterized by the Eocene and Miocene aged formations consisting of sedimentary lithological units, overlying the Palezoic metamorphic thrusted into the Eocene units. The Eocene Mülk is the formation studied in the project having the oil shale and evaporites (Camur et al., 2008), as shown in Figure 3.6.

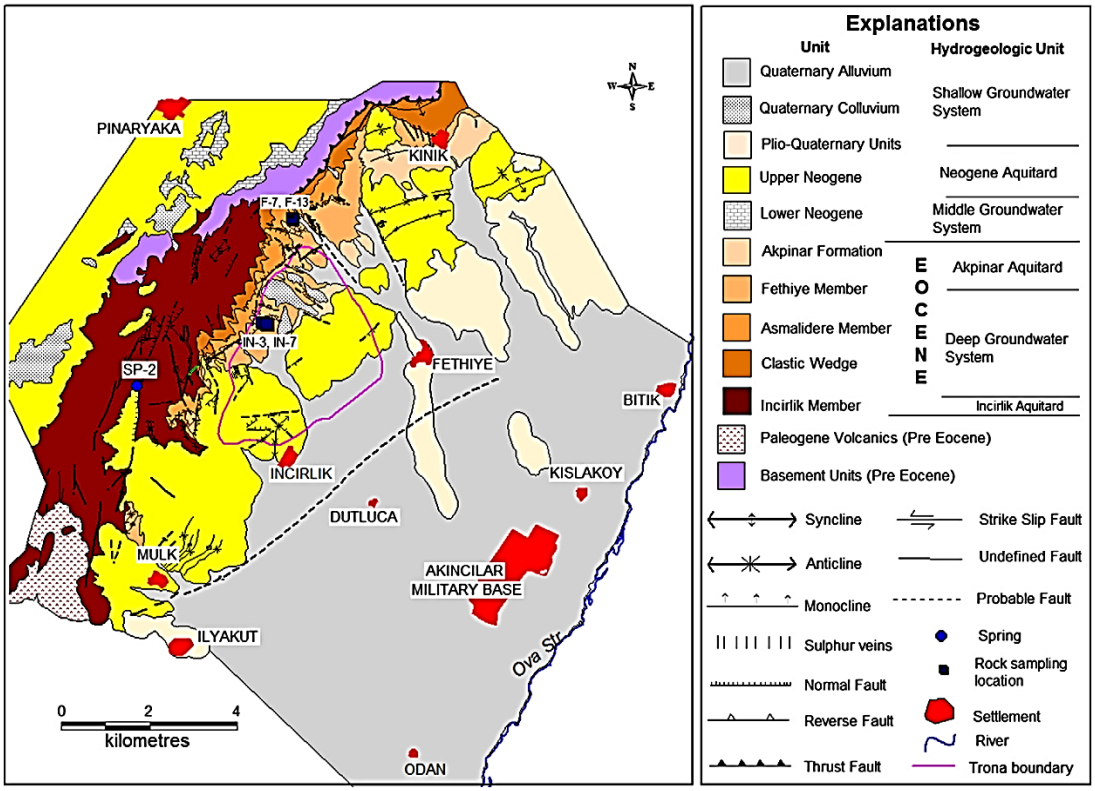

Figure 3-6: The simplified geology of Kazan (Camur et al., 2008)

3.2.1. Stratigraphy

In the project area, there are four rock formations from top to bottom; Plio-Quaternary deposits, Neogene Units, Eocene sequences (Mülk Formation and Akpınar Formation), and Paleozoic Metamorphics according to the geological studies (Ketin, 1996), as illustrated in Figure 3.7.

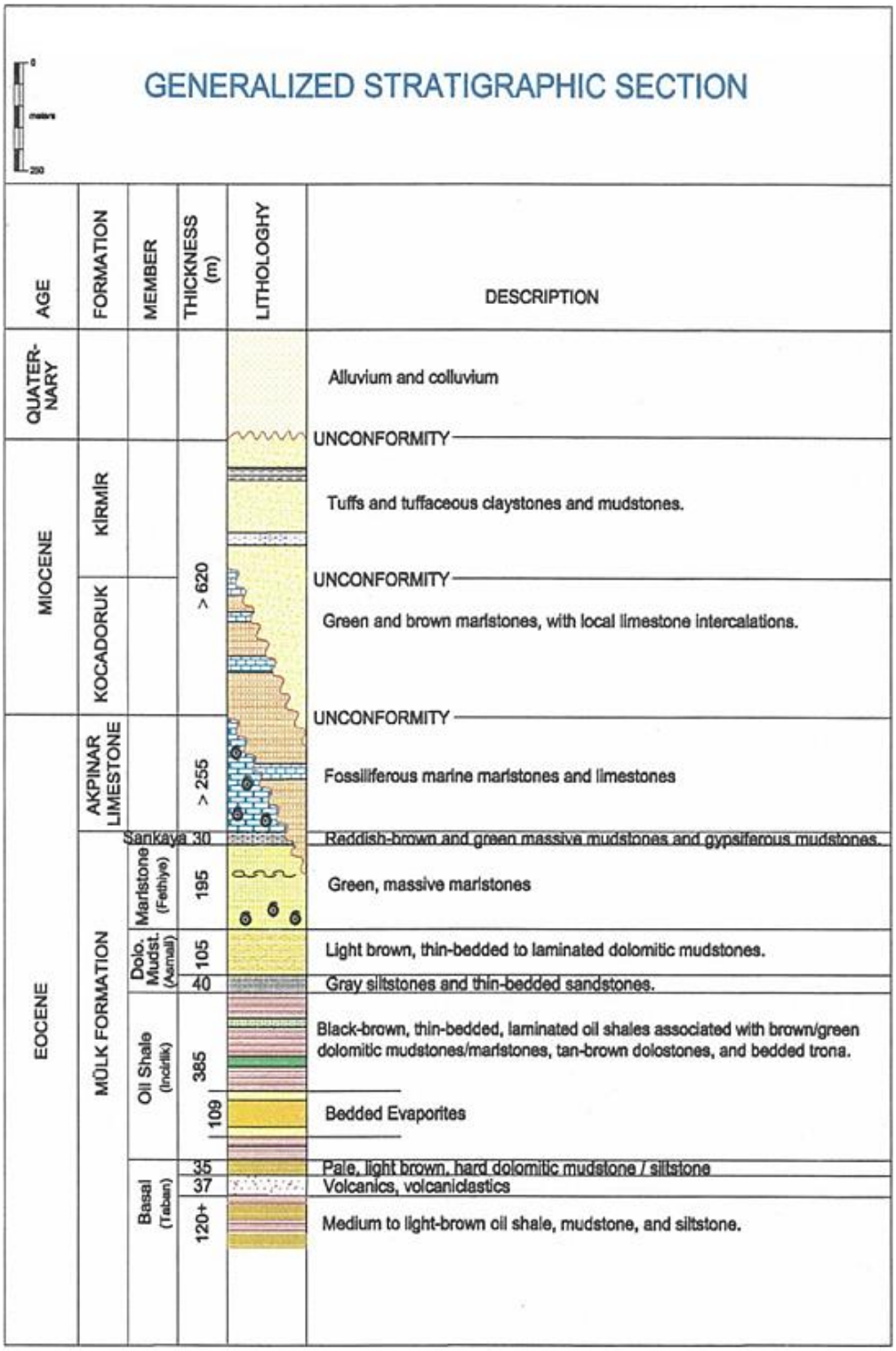

Figure 3-7: The regional geology and structural map (Ketin, 1996)

- **Paleozoic Metamorphics**

This rock formation is at the basement in northeast-southwest metamorphic trends in the northwest of the project area. Intensely deformed, graphitic schists black metamorphics surrounds gray-blackish gray, thick-bedded, and intensely fractured limestones into the Eocene sequences. Neogene units overlay this unit. The volcanics of the Paleogene in the southwest consist of lavas, tuffs, and volcano-clastics enclosed by the Eocene.

- **Eocene Sequences**

These sequences are separated into two formations, the lower Mülk Formation and the upper Akpınar Limestone Formation. Those units are outcrops in the direction of northeast-southwest. The complete range of the Eocene units is observed in the northwest direction of the Fethiye and İncirlik villages. The Palegene volcanic-sedimentary sequence to the southwest of Mülk village encrusts the Eocene units.

- **Mülk Formation**

This formation consists of four lithologic sequences. Those are brownish yellow sandstones and mud rocks, Taban Member, oil-shale, marl-sandstone- conglomerate sequence (İncirlik Member), yellow-yellowish brown sandstones conglomerates-siltstones and cream marls (Asmalıdere Member), and light green marls (Fethiye Member). Fethiye member is composed of green marls with clayey limestone to the top parts of the sequences. Asmalıdere member has brown-gray, highly porous sandstone-conglomerate-siltstone sequence with marls and mudstones at the top. İncirlik member consists of thick bedded sandstones and conglomerates at the bottom with clayey limestones and marls. Taban member is composed of deformed brownish yellow mudstones-siltstones-sandstones with volcanics.

- **Akpınar Formation**

The Formation consists of reddish-brown siltstones, sandstones, and conglomerates (Sarıkaya Member) at the base and green marls, green sandstones, conglomerates, and sandy limestones at the top.

- **Neogene Units**

The conglomerates of the Neogene overlay the Paleozoic metamorphics (Mülk and Akpınar Formations). The lower sequence of Neogene units outcrops in the western part of the project site. The units are composed of clayey and cherty limestones and mudstones. At base over the Akpınar Formation, pebble conglomerates are found with overlying of the conglomerates, there are silty limestone changing into a green siltstone and mudstone sequences found.

- **Plio-Quaternary Deposits**

The isolated conglomerates form the Plio-Quaternary Deposits; those are talus accumulations, alluvials, and alluviums. This unit is a flat deposit on the Eocene unit by angular unconformity.

3.2.2. Structure

Northeast-southwest trending folds in Neogene and Eocene units are the main structural features for the Kazan basin. Faulting is in the strike direction of both northeast-southwest and perpendicular northwest-southeast for the project site. In Eocene unit faults, normal, strike-slip and reverse faults are observed in this trend. In the north and west parts of the project site, reverse faulting is seen in the trend of northwest-southeast. The fracture sets, joints, faults, and veins have two dominant trends as N20-30E and N70-80W. In the Neogene faults, trends of normal, left-lateral strike-slip, and right-lateral strike-slip faults are N15 40W, N40 45E, and N15 30W, respectively.

3.3. FMI Logging of the Borehole V040A

In this study, the borehole, named as V040A, was logged by FMI. The borehole is located in the project area as seen in Figure 3.8. However, to obtain the stratigraphic information of the site, FMI was used for only this borehole. This log covered depth of the borehole from 50 m to 549 m with 8.5 inch diameter, hence this interval of the borehole was analyzed. After the interpretation of the FMI log from caliper logs and resistivity images in terms of failure types, the failures mentioned in chapter 3.1 were identified.

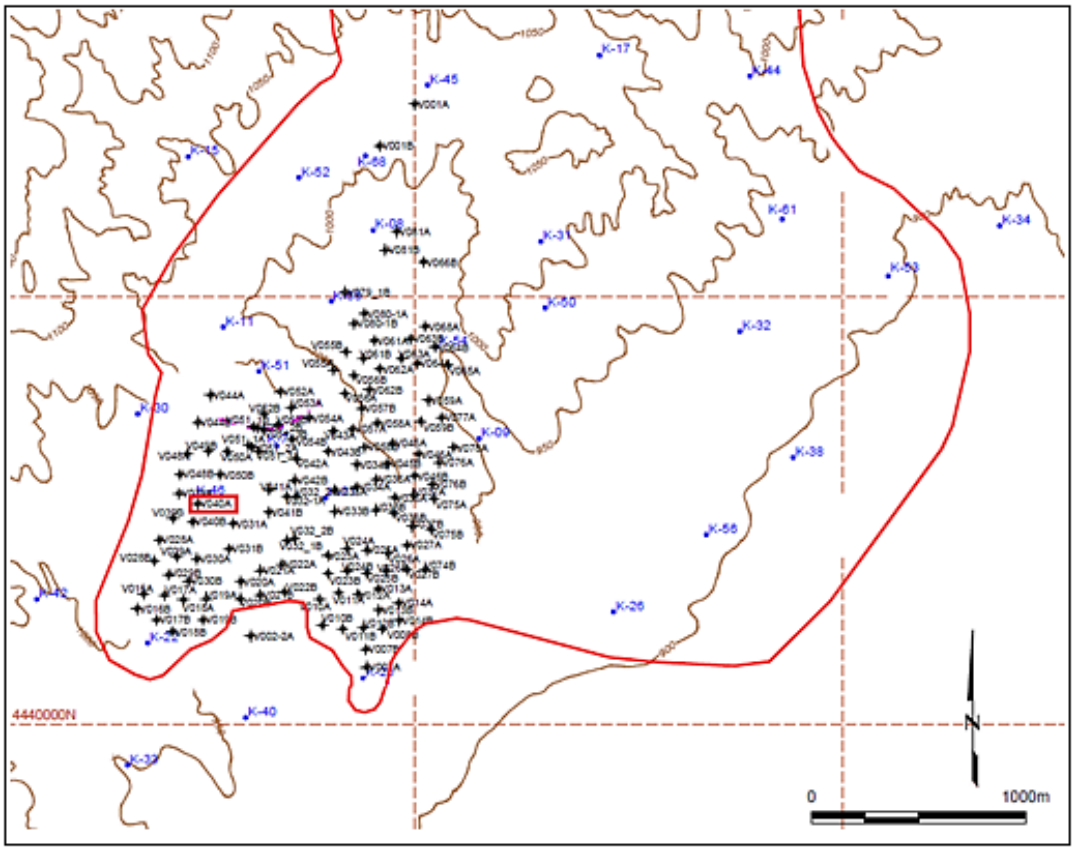

Figure 3-8: The location of the FMI logged borehole and other boreholes

According to the analysis of FMI log for this borehole, DIFs were not captured along the borehole, and washouts and key-seats were seldom obtained. On the other hand, the detected failures were all breakouts, Appendix A. In Table 3.1, the obtained breakouts are listed with their azimuths, lithology, and interval of depth. In the first

150 m, 8 breakouts were observed with some spacing among each other. In the last 300 m, the breakouts were not also encountered.

Table 3-1: *Type of Failure for a given depth*

Type of Failure	**Azimuths (degree)**	**Lithology**	**Interval of Depth (m)**
Breakout	(90-135) - (270-315)	Marl	77.75 - 78.50
Breakout	(90-135) - (270-315)	Marl	94.00 - 95.00
Breakout	(90-135) - (270-315)	Marl	117.75 - 118.50
Breakout	(0-45) – (180-225)	Marl	121.00 - 123.50
Breakout	(45-90) – (225-270)	Marl	124.00 - 125.00
Breakout	(45-90) – (225-270)	Marl	126.50 - 127.50
Breakout	(45-90) – (225-270)	Marl	141.00 - 142.00
Breakout	(45-90) – (225-270)	Marl	143.75 - 144.75
None	-	Marl – Shale (Trona)	144.75 - 549.00

Rose diagram in terms of their frequency and angles (or breakout width) was utilized to estimate the general trend of orientation according to the breakout azimuths, Figure 3.9. By this rose diagram, the orientation of S_{hmin} could be identified in trend of N78.75E since the breakouts are observed at the azimuth minimum horizontal stress. Although the borehole does not include any DIF data, the direction of S_{hmax} can be identified by adding 90 degrees to the azimuth of S_{hmin} since the direction of S_{hmax} is perpendicular to S_{hmin} direction; therefore, the S_{hmax} direction is N11.25W.

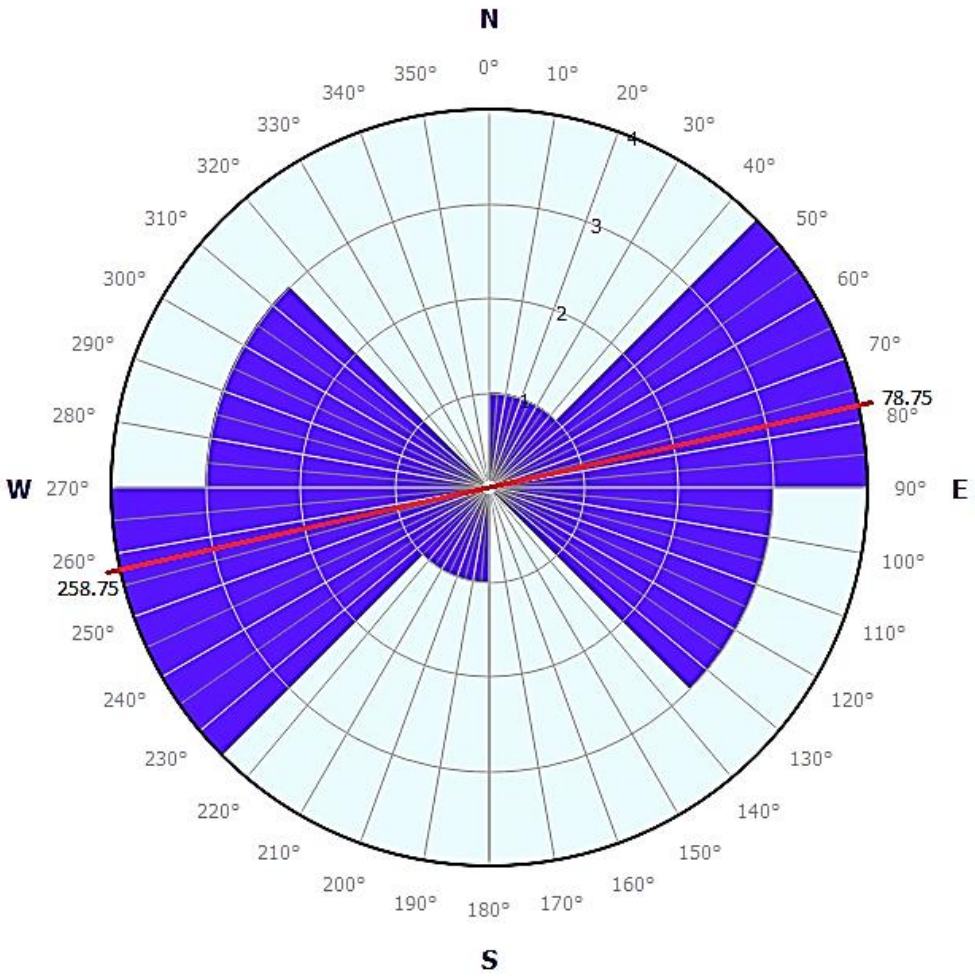

Figure 3-9: Rose Diagram of the Borehole from FMI log shows trend N78.75E S_{hmin}

CHAPTER 4

FIELD AND LABORATORY STUDIES

To estimate the magnitude of S_{hmax}, the mechanical properties of the rock and the magnitude of S_{hmin} in the field are required as mentioned in Chapter 2. In this chapter, the established field and laboratory studies will be covered to obtain those parameters. Leak-off tests (LOTs) were carried out in the field to have the magnitude of S_{hmin} are explained with their results. Besides, the rock mechanics experiments will be mentioned to have the parameters; the compressive and tensile strength, Young's Modulus, Poisson's ratio, cohesion, and internal friction of the rock units.

4.1. Field Studies

In the field studies, LOTs were applied to the boreholes in the Project area to get minimum formation pressure of the site. It is one of the direct measurements of the least principal stress, it can be considered as one type of hydraulic fracturing; hydraulic fracturing methods are the only ways applied in the boreholes to have reliable results of S_3.

Pressure integrity tests are established to determine the maximum pressure that can be applied by the maximum mud weight since providing the stability of the borehole is one of the most important issue in exploration and drilling.

They are measurements of the formation strength; those tests are generally classified as leak-off tests (LOT), formation integrity tests (FIT), and extended leak-off tests (XLOT or ELOT), (Addis et al, 1998; Postler, 1997). The purposes of those tests are identifying the limits of the formation strength, the integrity of the cement, acquiring the magnitude of in-situ stress, and some other properties such as permeability (Allerstorfer, 2011). The main difference of those tests is the application of pressurization in the borehole.

In the FIT, the pressure is risen up to some pre-defined level, based on the evaluation of that the borehole pressure will be reached in the safe drilling of the other boreholes, therefore the verification of the quality of the cementing of casing is the essential objective of this type of testing. FITs are utilized in case of verification of the formation integrity to the expected maximum pressure while drilling. The main purpose is testifying the safe drilling, since the observation is only about the linear section of the pressure applied versus volume plot. Therefore, this test cannot provide the strength of the formation. Less cost, shorter test time, and preventing of any possibility of weakening the formation due to LOTs and XLOTs are the reasons why this method is preferred (Allerstorfer, 2011).

In the LOT, the pressure is heightened up to observation of the leak in the formation due to the initiation of the fracture, the pressure is increased up to change in the linearity of the pressure versus volume plot, on the contrary to FITs. This test is used to take shut-in time pressure, leak-off pressure, and minimum formation pressure. The objective is to obtain the formation pressure at the fracture initiation.

The XLOT can be considered as the cyclic type of LOTs since initiated fracture is opened up to a considerable level and this procedure is applied in a cycle manner by pressurization (Raeen & Brudy, 2001). This cycle is continued until a stable pressure level is observed. This method is more reliable for the estimation of in-situ stress magnitudes (S_{hmin}) than LOTs. However, ELOTs are not used as standard field testing unless special conditions exist such as that a fracturing treatment is required (Allerstorfer, 2011).

In this study, LOT was conducted in the boreholes, therefore, the results of LOTs were used to estimate the magnitude of S_{hmin}.

4.1.1. Leak-off Test

After drilling the formation around 3 to 5 meters, the drill string is inserted and pulled back to the casing to execute the test, then the fluid is gradually sent to the borehole as seen in Figure 4.1. At a certain level of pressure, the pump is stopped. After the

pressurization is stopped and kept constant, the pressure gauge is monitored to validate the existence of any leak-off. This is called as shut-in pressure before the pressure is released.

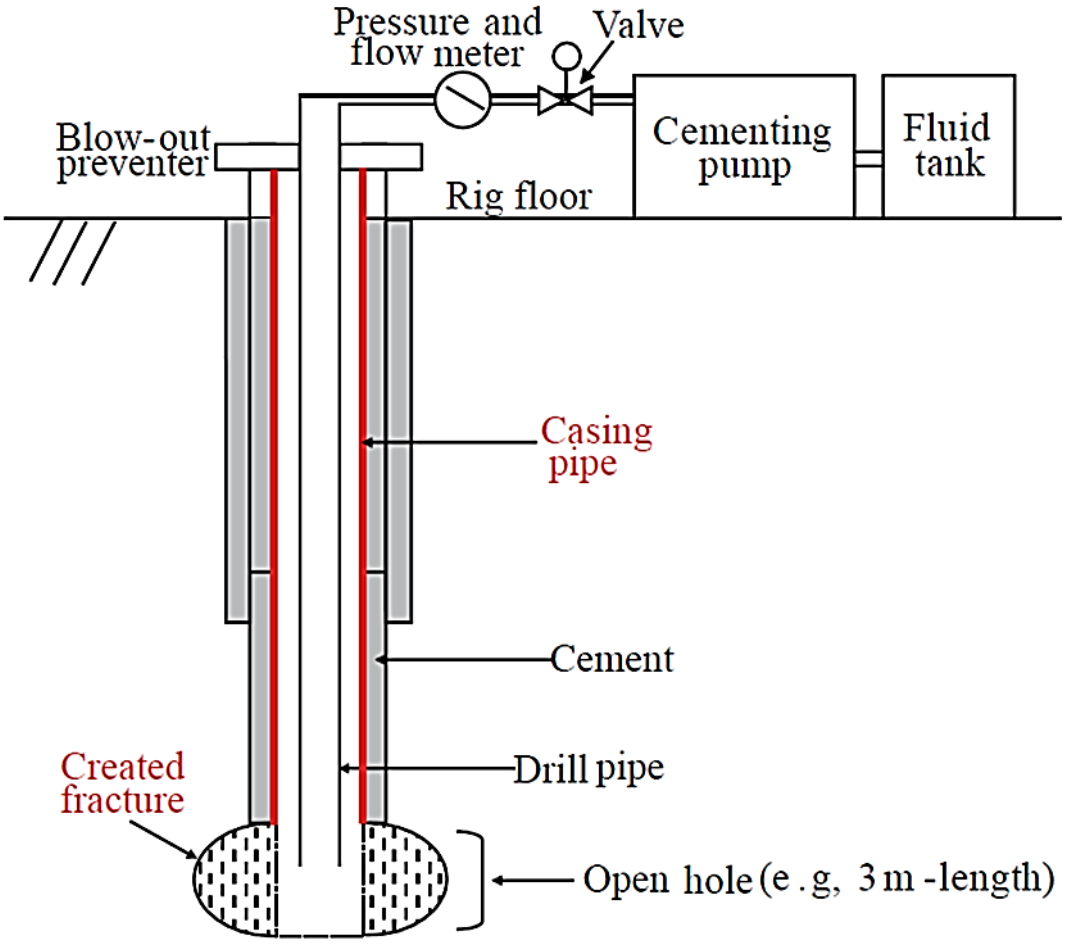

Figure 4-1: A schematic view of a borehole during a LOT (Yumamato, 2003)

During this testing procedure, the main point is the plot of pressure versus volume of the fluid pumped to the borehole. At the end of the test, each portion of the plot represents different pressure values such as leak-off pressure, maximum test pressure, minimum test pressure, and fracture closure pressure as represented in Figure 4.2.

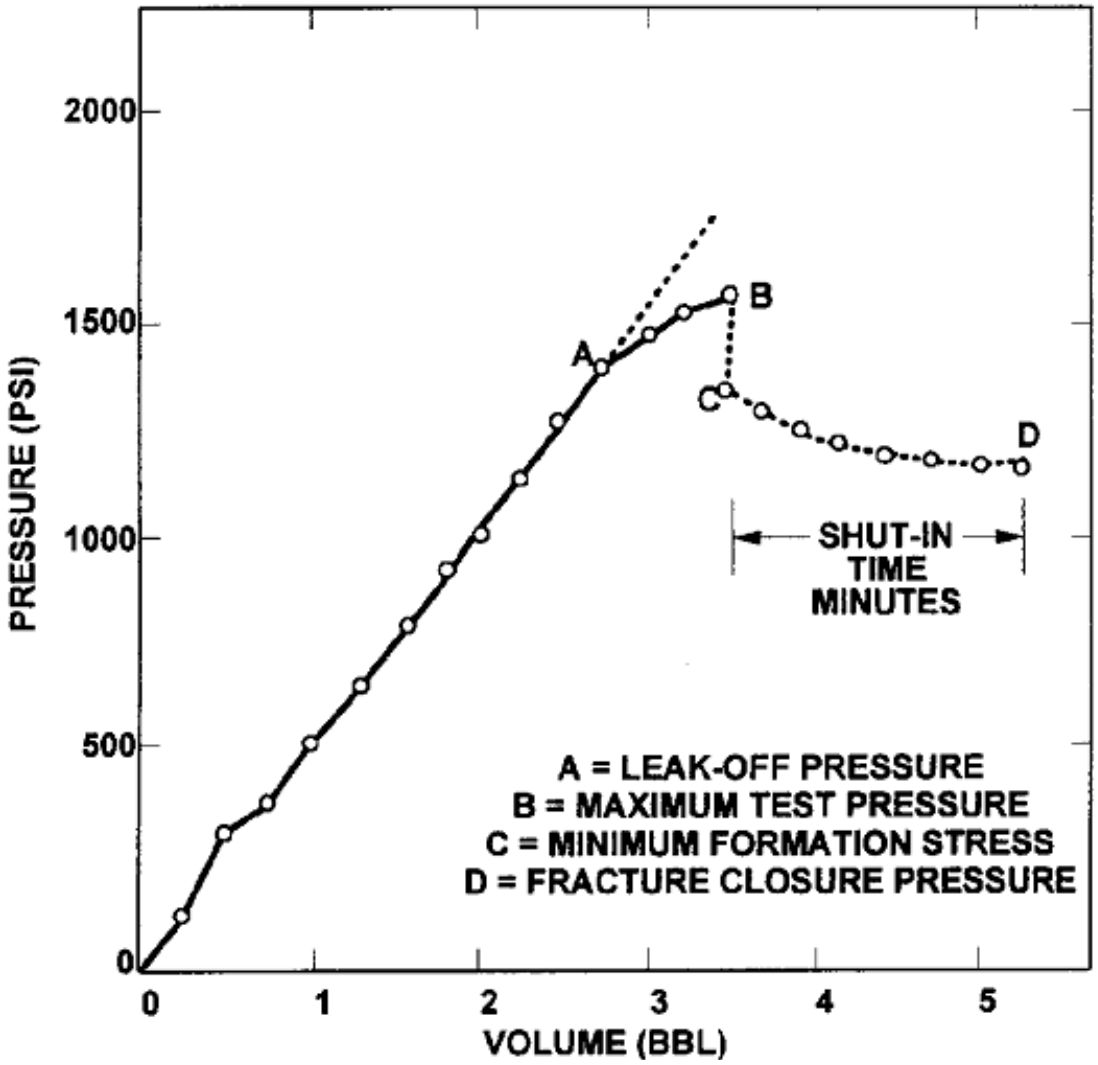

Figure 4-2: A typical Leak-off test plot, (Postler, 1997)

At the beginning of the pumping, equal amount of volume provides a constant increase of pressure. This compression of drilling causes elastic enlargements in the borehole, it is the linear portion of the plot. This linearity is not a perfect straight line due to some small losses to the formation but those losses are not resulting in nonlinearity. On this linear line, the first important point is called as leak-off pressure, shown by point A. After this point, the line starts to deviate, bending to the right. This deviation means that although the fluid is pumped into the borehole, the rate of increase of the pressure is decreased. The reason of this is that a small and stable fracture is opened. Opening of the crack cause fluid loss due to two occasions, those are entering of the

mud into the fracture and loss of filtrate along the permeable surfaces of the fracture. This point is also called “leak-off point” or “pit limit” (Postler, 1997).

The portion in between point A and B represents stable fracture growth with increasing pressure. In this part, pressure increase and fluid losses across the length of the growing fracture result in that stable crack growth. By the increase in pressure at the crack tip, initiation of unstable crack growth is observed in the borehole. The pressure just before the unstable crack growth at the tip of the crack is almost equal to the minimum fracture propagation pressure. By the observation of leak-off, the pressurization is stopped at point B. Then, shut-in pressure is recorded to monitor whether there is a leak or not. In the range between point B and C, the pressure is sharply dropped since the fluid is lost into the open fracture and the pump friction pressure loss. This sharp drop in pressure indicates that the fracture is closed, after that this shut-in pressure decreases slowly to point D. The slow decrease is caused by a small amount of fluid loss to the permeable faces of the fracture. When the pressure reaches the steady state, the test is accomplished (Postler, 1997).

The fracture is getting closed rather than growing after pumping is stopped from point B to C when the level of pressure is equal to the minimum stress acting on the crack. Therefore, it is considered that point C, or the shut-in time pressure gives nearly the S_{hmin}. Postler (1997) noted that the pressure level at point C varies between the leak-off pressure (point A) and the half of that level with the evaluation of several LOTs. The reason of this range is stated to be a possible leak in the surface equipment or casing or cement channels. This relation is important in the approximation of S_{hmin} by LOT. It is considered that both the leak-off pressure and the shut-in time pressure might represent the S_{hmin}. If the testing is well implemented in terms of procedure, both of them will be close to each other and provide acceptable estimation of S_{hmin}, which is proven by previous studies, (White et al., 2002). The plots of the LOTs in the field have that the leak-off pressure and the shut-in time pressure are close to each other, therefore both of them give similar pressure values.

4.1.2. Leak-off Test Results

For this study, LOTs were conducted for 68 boreholes, shown in Figure 3.8. Therefore, in the estimation of the magnitude of S_{hmin}, the results of all borehole LOT and the borehole V040A were analyzed separately.

If the result of only V040A is taken into consideration, S_{hmin} is approximately 3.5 MPa, Figure 4.3. On the other hand, since logging was done in V040A borehole, the results of the other boreholes are included by estimation of S_{hmin} using inverse distance square method in terms of distance of those ones to this borehole to obtain the general value of S_{hmin} for the area (Appendix B). By considering the distances and all results obtained, S_{hmin} is around 2.9 MPa. Therefore, this value is the results of inverse distance square method for all boreholes in the field.

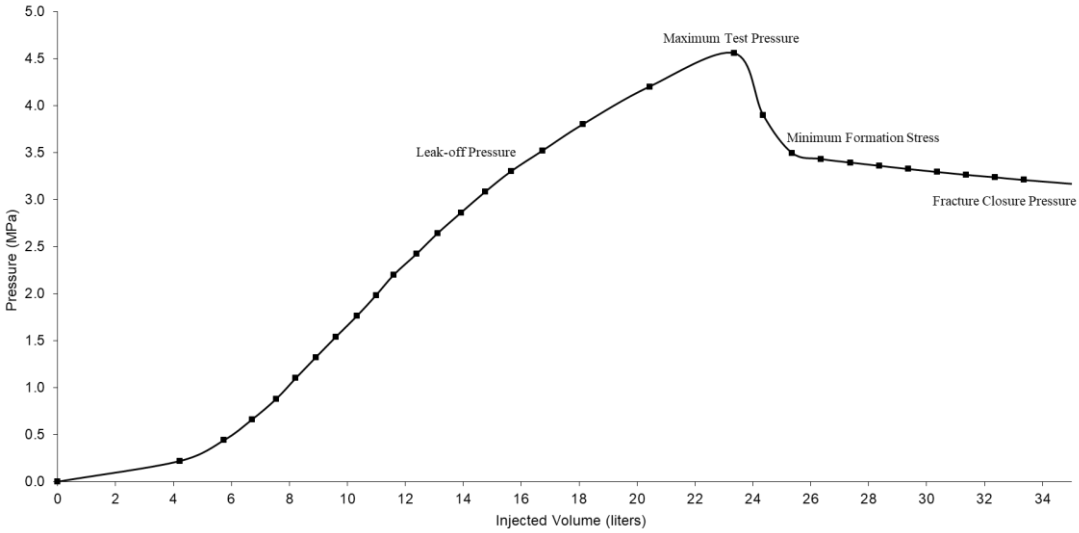

Figure 4-3: The leak-off plot of the borehole V040A

4.2. Laboratory Studies

As explained in the previous chapters, in order to estimate the magnitude of S_{hmax}, some steps have to be completed in order to identify the required parameters. By the results of LOTs, the magnitude of S_{hmin} was found. The other required parameters are the mechanical properties of rock units in the project area. It was observed that V040A

borehole is piercing two major rock units; marl and trona. Therefore, some rock mechanics laboratory experiments were conducted to obtain the compressive (C_0) and tensile strength (T_0), Young's Modulus (E), Poisson's ratio (ν), cohesion (c), and internal friction (ϕ) of both rock units. These experiments are static deformability, triaxial compressive strength, and Brazilian (indirect tensile) tests.

4.2.1. Static Deformability Tests

For determination of C_0, E and ν, 8 core samples were prepared, 6 for the properties of marl and 2 for the properties of trona rock units. MTS 815 Rock Testing Machine, a displacement-controlled testing machine, was utilized for those experiments. To obtain E and ν, the axial and lateral deformations were recorded during the loading with the rate of 0.002 mm/s. Clip-on gage extensometers were attached to the samples to get instantaneous data of both axial and lateral displacements as seen in Figure 4.4.

Figure 4-4: Static deformability test sample with axial and lateral extensometers after loading

A typical stress-strain curve for the samples is given in Figure 4.5, it shows the analysis of the sample called, DE-4. Stress-strain curves of the other samples can be viewed in Appendix C.

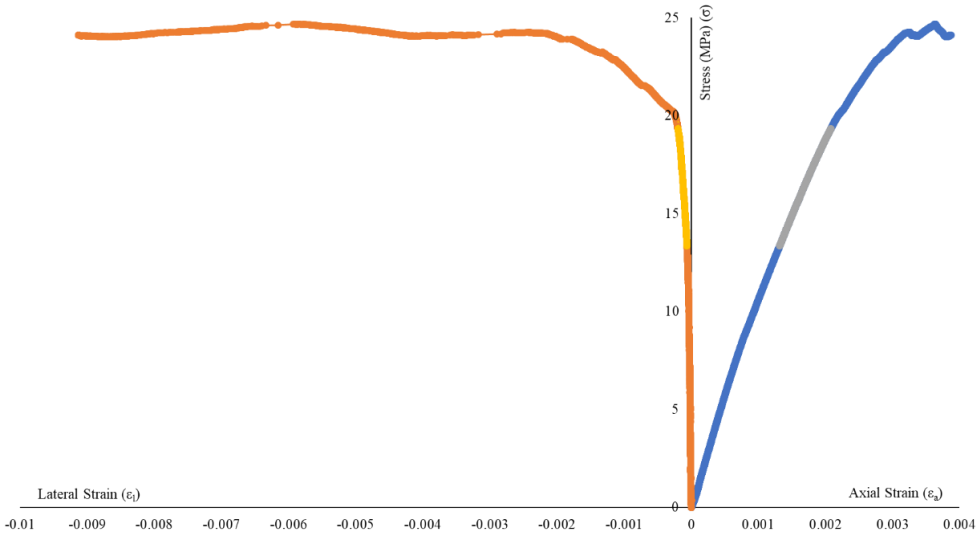

Figure 4-5: Stress-strain curve of the sample DE-4

The results of those experiments are presented in Table 4.1 with sample properties length and diameter, and the mechanical properties determined.

Table 4-1: *The Results of Static Deformability Tests*

Name of the Specimen	**Compressive Strength (MPa) (C_0)**	**Young's Modulus (GPa) (E)**	**Poisson's Ratio (v)**	**Diameter (mm) (Ø)**	**Length (mm) (L)**
DE-1 (Marl)	33.70	8.30	0.20	60.54	141.18
DE-2 (Marl)	16.70	4.70	0.30	60.16	140.13
DE-3 (Marl)	39.00	8.10	0.21	60.32	135.63
DE-4 (Marl)	25.70	7.90	0.17	60.31	136.74
DE-5 (Marl)	18.90	5.90	0.29	60.17	138.34
DE-6 (Marl)	30.10	8.20	0.20	60.42	131.74
DE-7 (Trona)	9.30	3.00	0.30	60.34	134.82
DE-8 (Trona)	9.80	2.00	0.30	60.28	132.85

The average compressive strength is 27.35 ± 7.87 MPa, Young's Modulus is 7.18 ± 1.38 GPa, and Poisson's ratio is 0.23 ± 0.05 for marl unit, while for trona unit, the average compressive strength is 9.55 MPa, Young's Modulus is 2.5 GPa, and Poisson's ratio is 0.30.

4.2.2. Brazilian (Indirect Tensile) Tests

Brazilian tests were performed to obtain tensile strength of the rock units, as indicated in Table 4.2, the specimens named BT-1 to BT-6 are the marl samples, seen in Figure 4.6, while the rest are the trona samples in Table 4.3. Similar to static deformability tests, MTS 815 Rock Testing Machine was utilized for those experiments with the loading rate of 0.002 mm/s.

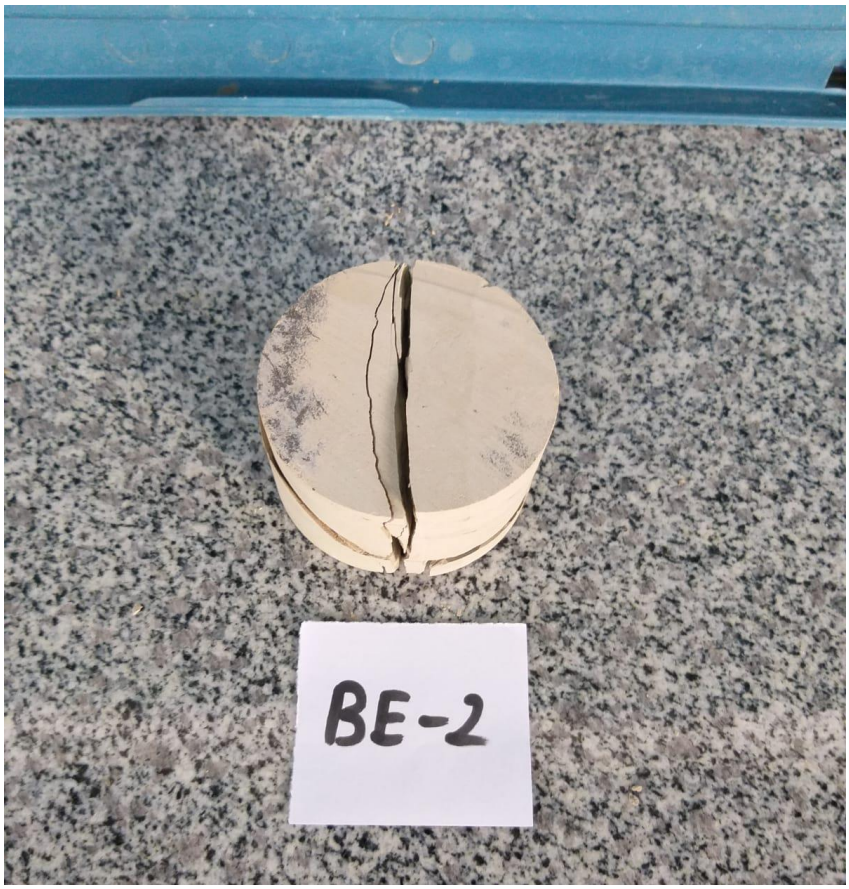

Figure 4-6: Brazilian test specimen after failure

The results of the indirect tensile tests are given in Table 4.2 and Table 4.3.

Table 4-2: *The Results of Brazilian Tests for Marl*

Name of the Specimen	Tensile Strength (MPa) (T_0)	Diameter (mm) (Ø)	Thickness (mm) (t)
BT-1 (Marl)	6.02	60.46	36.31
BT-2 (Marl)	5.39	60.42	36.40
BT-3 (Marl)	6.15	60.46	34.69
BT-4 (Marl)	4.36	60.45	36.12
BT-5 (Marl)	5.27	60.51	36.47
BT-6 (Marl)	4.17	60.58	35.39
Average Strength (MPa)	5.23 ± 0.75		

Table 4-3: *The Results of Brazilian Tests for Trona*

Name of the Specimen	Tensile Strength (MPa) (T_0)	Diameter (mm) (Ø)	Thickness (mm) (t)
BT-7 (Trona)	0.89	60.34	36.42
BT-8 (Trona)	0.71	60.49	35.84
BT-9 (Trona)	1.38	60.48	34.96
BT-10 (Trona)	1.29	60.41	36.28
BT-11 (Trona)	1.21	60.53	34.52
BT-12 (Trona)	1.13	60.49	35.76
BT-13 (Trona)	1.03	60.52	36.19
Average Strength (MPa)	**1.27 ± 0.57**		

4.2.3. Triaxial Compressive Strength Tests

In order to determine cohesion and internal friction angle of the rock units, triaxial compression tests were conducted. There were 5 triaxial compression sets prepared, 3 sets for marl and 1 set for trona.

In the experiments for marl, 12 specimens were prepared and the smallest principal stress (σ_3) levels were 3, 6, 9, and 12 MPa, respectively for one set of experiments, Table 4.4.

Table 4-4: *The Results of Triaxial Compressive Strength Tests for the Marl*

Name of the Specimen	σ_1 (MPa)	Diameter (mm) (Ø)	Length (mm) (L)	Density (g/cm3)
TE 1-1 (σ3=3)	46.63	60.45	129.97	2.30
TE 2-1 (σ3=6)	64.39	60.42	126.54	2.14
TE 3-1 (σ3=9)	72.34	60.47	126.81	2.29
TE 4-1 (σ3=12)	90.85	60.53	129.36	2.22
TE 1-2 (σ3=3)	47.06	60.42	125.94	2.09
TE 2-2 (σ3=6)	52.63	60.41	125.97	2.03
TE 3-2 (σ3=9)	68.17	60.30	128.19	2.23
TE 4-2 (σ3=12)	134.23	60.51	128.50	2.36
TE 1-3 (σ3=3)	35.89	60.56	129.00	1.93
TE 2-3 (σ3=6)	55.33	60.43	127.78	1.91
TE 3-3 (σ3=9)	59.70	60.22	126.21	1.85
TE 4-3 (σ3=12)	66.12	59.93	127.72	1.88

With those results, the cohesion of marl was found as 6.83 ± 0.72 MPa, and the internal friction angle was 37.44° ± 1.41°. Besides, average density was estimated as 2.1 g/cm^3.

On the other hand, 3 specimens were taken for trona, and σ_3 was adjusted to be 0, 5, and 10 MPa, respectively. The cohesion of trona was found as 0.99 MPa, and the internal friction angle was 53.65° with 2.14 g/cm^3 of average density. Mohr's circles of samples are given in Figure 4.7 and Figure 4.8. Details of the laboratory studies can be investigated in Appendix C.

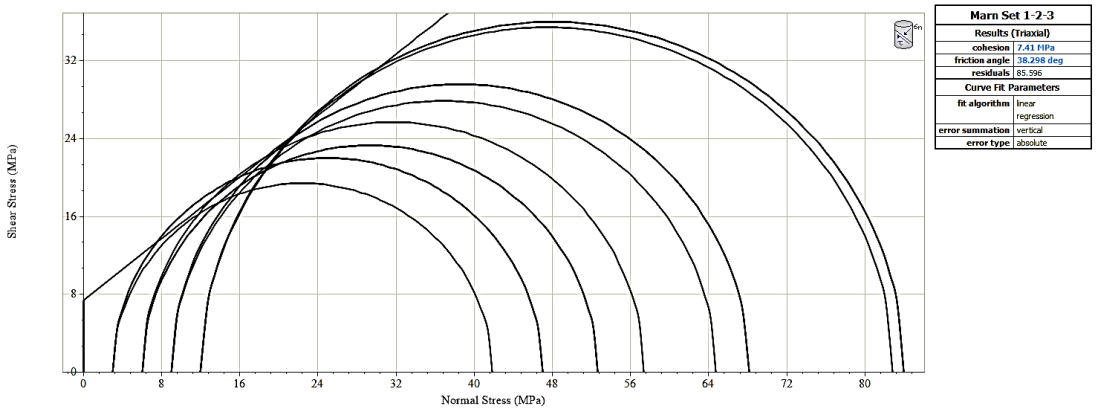

Figure 4-7: Mohr Circle's of Marl Samples

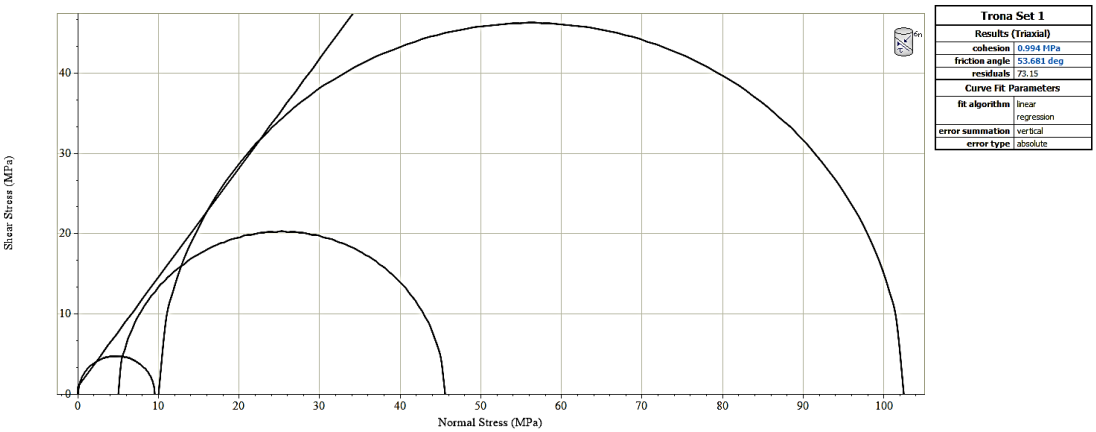

Figure 4-8: Mohr Circle's of Trona Samples

CHAPTER 5

NUMERICAL MODELLING

This chapter covers the numerical modelling of the cross-sections of the borehole V040A. The main purpose is to find out the magnitude of S_{hmax} by numerical analysis for two different corresponding S_{hmin} magnitudes. The correlation between r_d and stress/strength ratio is also the other objective in this chapter. In addition to those, the analytical results and numerical results were compared in the estimation. FLAC 2D (Itasca, 2016) software was utilized for numerical analyses of this study.

5.1. FLAC

FLAC 2D is a numerical analysis program that uses a two-dimensional explicit finite difference method. Dynamic equations in explicit time-marching scheme are used in FLAC. Newton's law of motion, (the equations of motion), constitutive relations, and boundary conditions are the components in the solution of solid body problems. Finite difference meshes (quadrilateral elements) divides the solid body defined. For the calculation steps, the velocities and displacements are acquired from forces and stresses, strain rates are obtained correspondingly those velocities and new stresses from strain rates by the equations of motion. The program examines the state of element if it is elastic or plastic in each cycling step for plasticity analysis. By the stress increments, elastic trials are calculated from the total strain increment and controlled by whether the yield criterion is disrupted or not. Therefore, in order to take plastic deformation, the stresses violate the yield criterion assigned, (Itasca, 2016). The mechanical behavior of soil, rock, or other materials can be simulated. Elements or zones are used to represent the materials creating grids to form the shape of the objects modeled. Predefined linear or nonlinear stress/strain laws for the materials determine the behavior of elements with the applied forces and the boundary conditions.

Although this program was firstly developed for geotechnical and mining engineering purposes, it can provide solutions for complex problems of mechanics by built-in constitutive models for highly nonlinear, irreversible geologic, or similar, materials available (Itasca, 2016). It includes several features;

- Plane strain, plane stress and axisymmetric geometry modeling,
- Interface elements to model different planes where separation might occur,
- Groundwater and consolidation models,
- Simulation of structural supports,
- Viscoelastic and viscoplastic models,
- Thermal modeling capability,
- Dynamic analysis capability,
- Graphical-user interface in model construction
- User-defined constitutive models written in C++

5.2. Borehole Cross-Section Models

In numerical analysis of the borehole, plane strain condition is implemented for 2D modeling. A full square zone is created, and an empty circular section is assigned at the center of this square zone to represent the borehole as seen in Figure 5.1. Mesh around the borehole is discretized finally as shown on the close-up view in order to capture failure zones in “mm” level. Each mesh is a rectangle with a dimension of 2.67 mm.

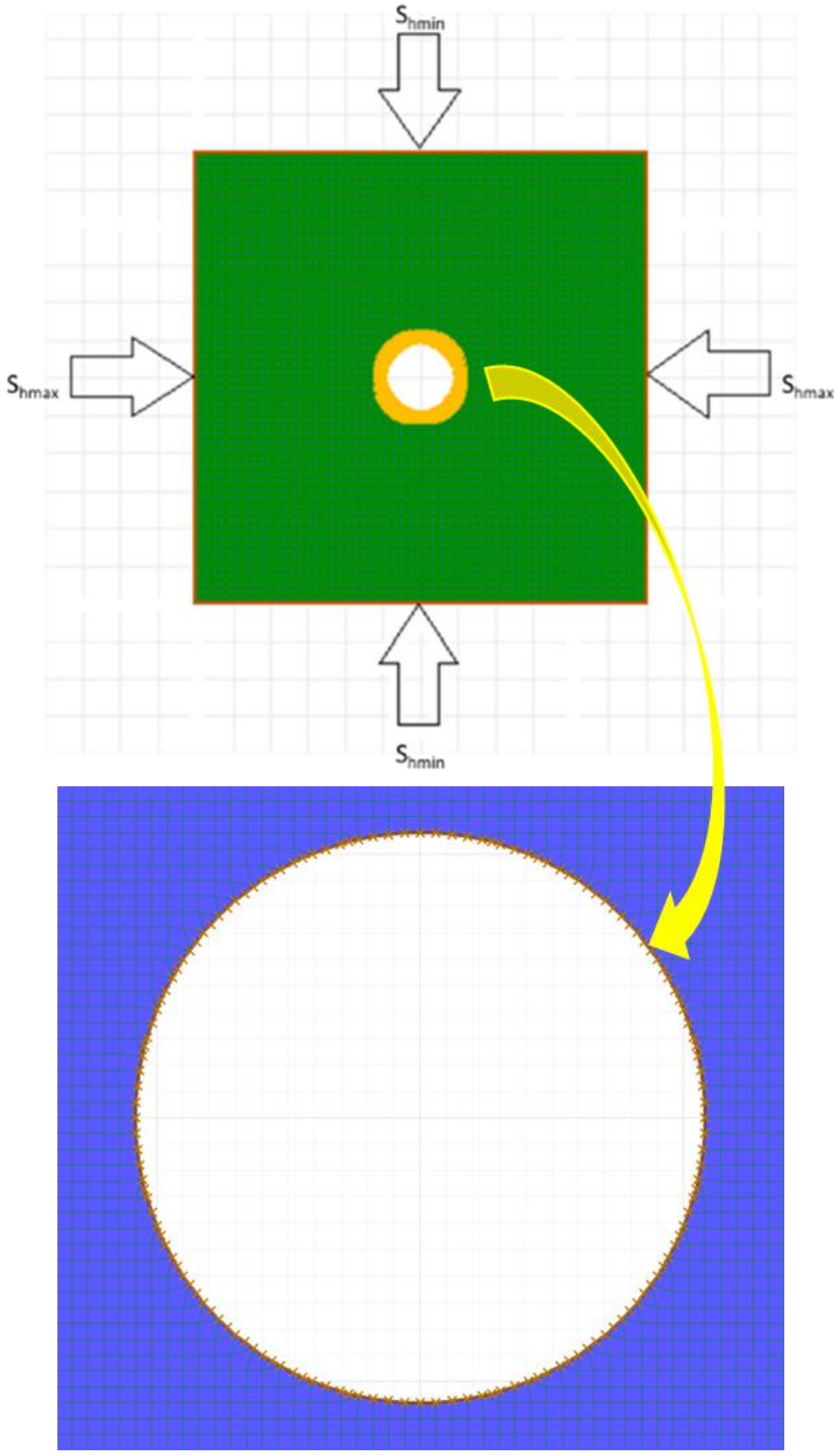

Figure 5-1: Modelling geometry of the borehole section

This rectangle is subjected to the far field stresses S_{hmax} and S_{hmin}, orthogonally to all boundaries as the boundary conditions. The rock properties obtained by laboratory studies are the input parameters of the square domain, while the empty borehole section is defined to be null in terms of rock properties to represent the borehole with a radius of 0.108 m. According to explanations in Chapter 2 (such as compressive shear failure mechanisms of breakouts), it was decided to assign Mohr-Coulomb failure criterion for the perfectly plastic rock behavior determined by the stress-strain curves, see Appendix C.

After modeling the cross-sections, the model was run in elastic stages in order to validate the elastic model by the comparing with analytical solutions (Kirsch solution) in terms of variation of radial and tangential stresses as a function of the distance between the far field and the borehole boundaries. For validation run, both horizontal stresses were kept equal to be 3.5 MPa, hence the curve in Figure 5.2 represents the change in the tangential and the radial stresses with respect to the distance from the borehole wall and demonstrates that both stress components match the stresses calculated by Kirsch's solution. It is important to remind that θ is defined in x-y plane and it is equal to zero at the azimuth of S_{hmax}. This validates the elastic 2D circular FLAC models.

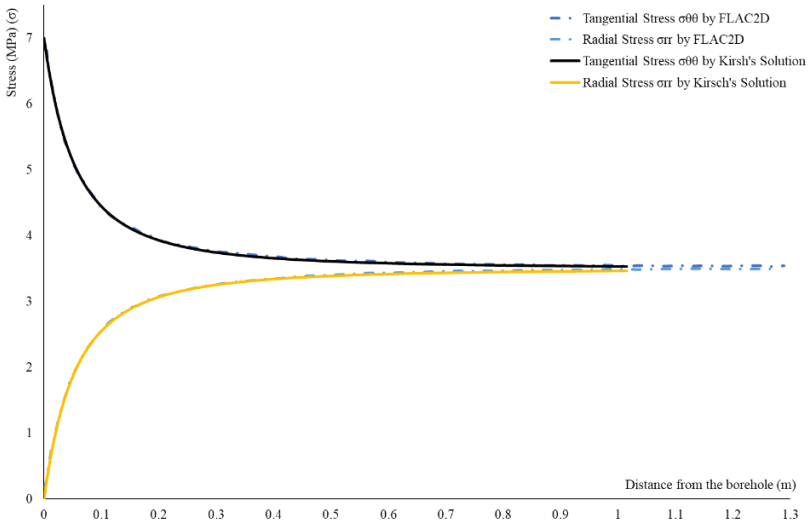

Figure 5-2: Comparison of FLAC and Kirsch's Solution in elastic state

There are two different rock units marl and trona, therefore, the input parameters were different for the same modeling geometry to analyze both units, Tables 5.1 and 5.2.

Table 5-1: *The Mechanical Properties of Marl used in FLAC*

Properties	**Quantity**
Poisson's Ratio	0.23
Young's Modulus	7.18 GPa
Density	2.10 g/cm^3
Cohesion	6.82 MPa
Internal Friction Angle	32.60°
Dilation Angle	0°
Tensile Strength	5.2 MPa

Table 5-2: *The Mechanical Properties of Trona used in FLAC*

Properties	**Quantity**
Poisson's Ratio	0.33
Young's Modulus	2.50 GPa
Density	2.14 g/cm^3
Cohesion	0.99 MPa
Internal Friction Angle	53.65°
Dilation Angle	0°
Tensile Strength	1.27MPa

The existences and states of breakouts and DIFs were analyzed by different S_{hmax} and S_{hmin} combinations. By those rock parameters as inputs of FLAC, S_{hmin} is also the other constant parameter for each run with varying S_{hmax}. Therefore, as indicated in Chapter 4, S_{hmin} was assumed to have two different the values of magnitude; the first one is from the LOT of the borehole V040A, and the other one is the inverse distance square value of all borehole LOT results. These are 3.5 MPa and 2.9 MPa, respectively. In

this case, there are 4 different cases to be modeled in FLAC; analyses of marl and trona for S_{hmin}=3.5 MPa and S_{hmin}=2.9 MPa.

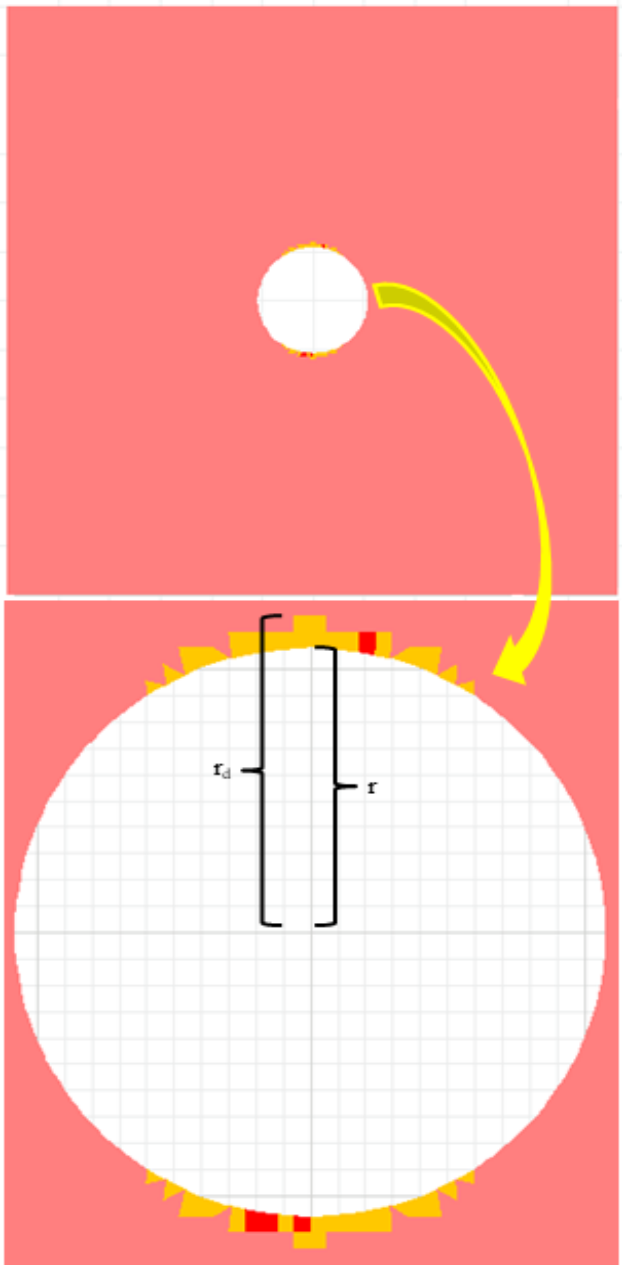

Figure 5-3: Borehole Breakout Represented by Yielded Elements

In these 4 analyses, with the given parameters above, the S_{hmax} magnitude was gradually increased by 0.2 MPa and 0.5 MPa increments, for trona and marl, respectively. The reason of different increments for those two units was the sensitivity

difference in failure analysis due to distinct rock parameters. By increasing S_{hmax} gradually, the dog-ear shaped borehole breakouts were observed, as seen in Figure 5.3. Then, after a certain level, DIFs were also observed with breakouts at the same time, as given in Figure 5.4. The runs were continued until the failure begins to become undefined, which means it is not a breakout or DIF anymore for the relevant cross-section and the failure mode is observed in the FMI zone.

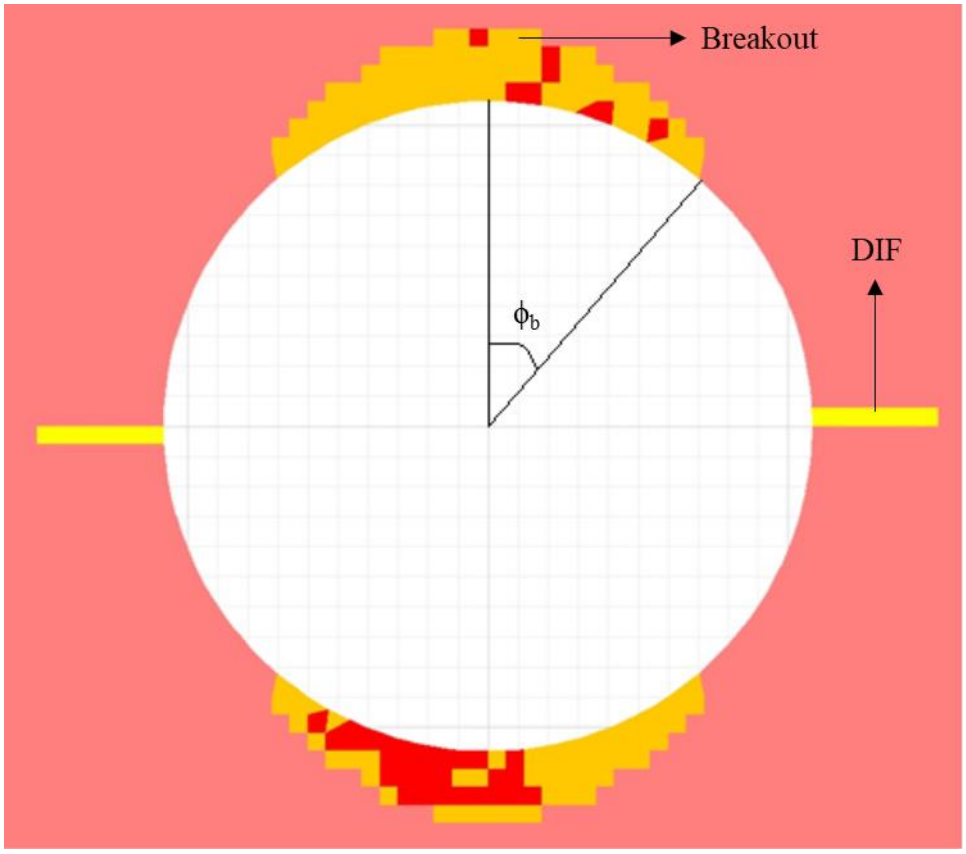

Figure 5-4: DIF and Borehole Breakout Represented by Yielded Elements

5.3. Numerical Analysis Run Results

During, FMI log readings no DIF were identified, therefore, the numerical analyses results giving breakouts were mainly used for the estimation of S_{hmax} and the correlation between failure and stress/strength ratio. Since there are two units along the borehole, the magnitude of S_{hmax} was analyzed for both units individually. The breakout data, obtained from FMI log, showed 8 different breakouts at different depths

with different amount of r_d and W_{BO}. Increasing S_{hmax} also simulated the increasing breakout depths and widths. These numerical analyses results versus stress/strength ratio were plotted, then the field data were plotted together with these charts to estimate the magnitude of S_{hmax}. This correlation presented the magnitude of S_{hmax} in addition to analytical solutions by Kirsch's solution, Barton and Zoback theory.

According to the FMI log, the breakouts are only observed in marl, hence the relation of the actual breakout and numerical breakouts might give a certain range for S_{hmax} magnitude, Table 5.3. However, there is no breakout in trona section, this means numerical breakouts might present limiting values for that section. It is only possible that S_{hmax} is less than the value causing breakout in FLAC.

Table 5-3: *The Obtained Normalized Breakout Depth (% of r) from FMI log with the given*

Type of Failure	**Depth of Interval (m)**	**Lithology**	**Normalized Breakout Depth (% of r) from FMI log**
Breakout	77.75 - 78.50	Marl	24.44
Breakout	94.00 - 95.00	Marl	16.67
Breakout	117.75 - 118.50	Marl	13.33
Breakout	121.00 - 123.50	Marl	31.11
Breakout	124.00 - 125.00	Marl	23.33
Breakout	126.50 - 127.50	Marl	22.22
Breakout	141.00 - 142.00	Marl	30.00
Breakout	143.75 - 144.75	Marl	13.33

The S_{hmax} will be estimated for those 8 breakouts by building up a correlation between the breakout depth, percentages that are normalized, and the ratio of maximum and minimum horizontal stresses to compressive strength.

5.3.1. Marl Results

According to the given parameters of marl, the analyses were completed with 3.5 MPa and 2.9 MPa of S_{hmin}, S_{hmax} was increased by 0.5 MPa increments. For S_{hmin}= 3.5 MPa, the borehole did not yield until S_{hmax} reached 10.5 MPa. 25 runs were performed up to 22 MPa, the breakout depths and widths were recorded after each run. Table 5.4 shows the stress level inputs and corresponding breakout depths and normalized breakout depths.

Table 5-4: *Modelling Results for the Marl (S_{hmin}=3.5 MPa)*

S_{hmax} (MPa)	**r_d (m)**	**Normalized Breakout Depth (% of r)**
10.0	0.1080	0.00
10.5	0.1143	5.88
11.0	0.1145	6.00
11.5	0.1151	6.54
12.0	0.1161	7.51
12.5	0.1228	13.69
13.0	0.1233	14.17
13.5	0.1238	14.63
14.0	0.1244	15.17
14.5	0.1253	16.04
15.0	0.1296	19.97
15.5	0.1308	21.15
16.0	0.1312	21.50
16.5	0.1321	22.30
17.0	0.1322	22.45
17.5	0.1394	29.10
18.0	0.1399	29.51
18.5	0.1399	29.55

19.0	0.1406	30.16
19.5	0.1474	36.48
20.0	0.1495	38.46
20.5	0.1498	38.69
21.0	0.1508	39.66
21.5	0.1512	39.98
22.0	0.1514	40.18

The correlation was visualized as a plot of the normalized breakout depth versus the ratio of maximum stress at the borehole wall to compressive strength of marl. Using these results, the best fit logarithmic line, upper and lower limit lines were drawn. The upper and lower limit lines were drawn by taking into account the farthermost points with respect to the best fit line. Furthermore, the actual breakout widths from the field data were plotted on those three lines to obtain a range of S_{hmax} magnitude, as shown in Figure 5.5.

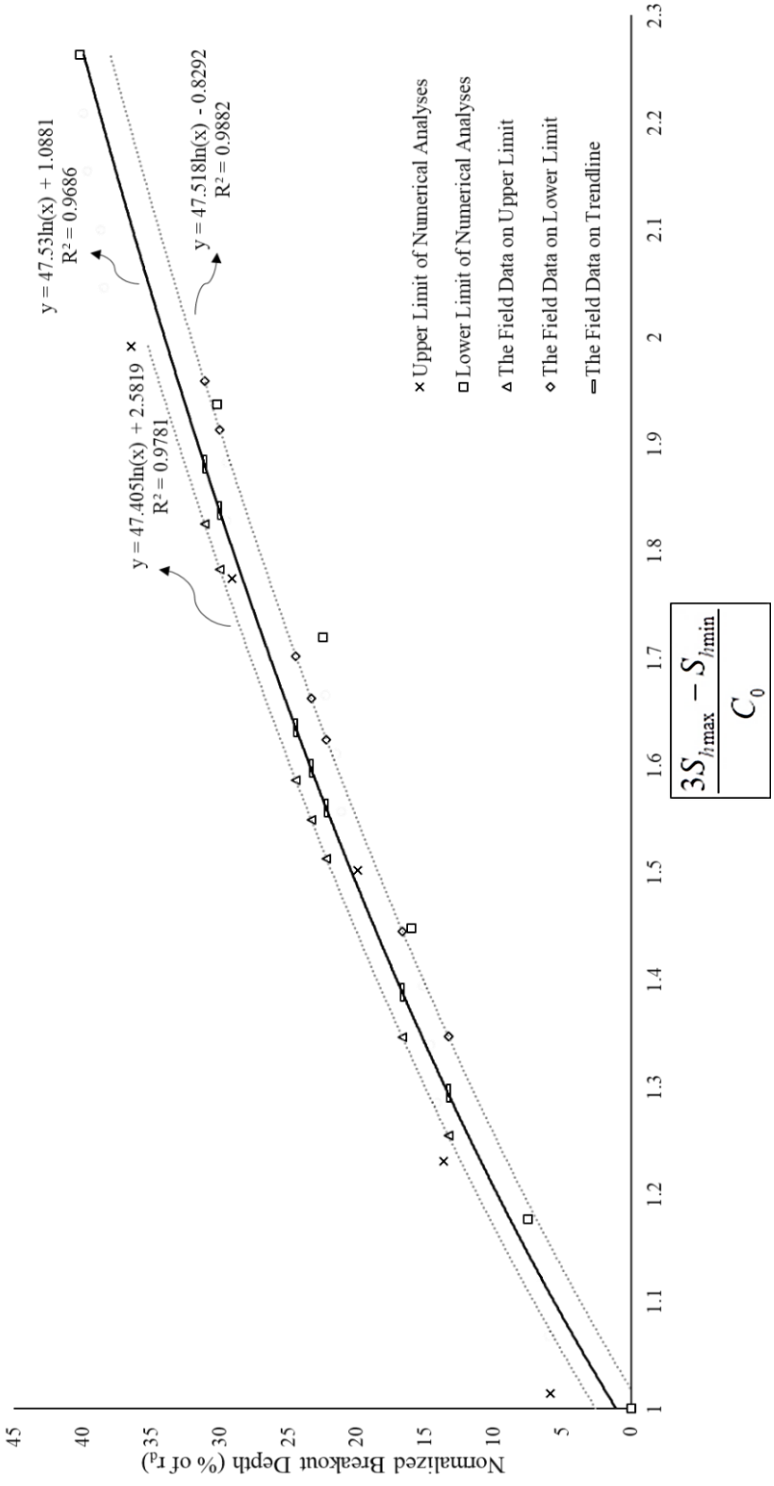

Figure 5-5: Correlation between Normalized Depth Percentage and Stress-Strength Ratio of the Marl for S_{hmin}=3.5 MPa

If the equations of the best-fit lines are converted to give the value of S_{hmax}, they are as follows; Equation 26, 27, and 28 of the best fit, the upper limit, and the lower limit, respectively.

$$S_{hmax} = \frac{\left(e^{2.10\frac{r_d}{r}-2.12} \right) C_0 + S_{hmin}}{3} \quad (26)$$

$$S_{hmax} = \frac{\left(e^{2.11\frac{r_d}{r}-2.16} \right) C_0 + S_{hmin}}{3} \quad (27)$$

$$S_{hmax} = \frac{\left(e^{2.10\frac{r_d}{r}-2.09} \right) C_0 + S_{hmin}}{3} \quad (28)$$

If the actual breakout depths are placed into Equations 26, 27, and 28, the values of S_{hmax} will be as in Table 5.5.

Table 5-5: *Normalized Breakout Depth Percentage of the Actual Field Data and Corresponding S_{hmax} Values on the Best Fit, the Upper Limit, and the Lower Limit Lines for S_{hmin}= 3.5 MPa*

Normalized Breakout Depth Percentage	**S_{hmax} (MPa) on the Best Fit**	**S_{hmax} (MPa) on the Upper Limit**	**S_{hmax} (MPa) on the Lower Limit**
24.44	16.22	15.77	16.84
16.67	13.95	13.56	14.47
13.33	13.08	12.72	13.57
31.11	18.48	17.97	19.20
23.33	15.87	15.43	16.47
22.22	15.53	15.10	16.12
30.00	18.08	17.58	18.78
13.33	13.08	12.72	13.57

For S_{hmin}= 2.9 MPa, the borehole did not yield until S_{hmax} reached 10 MPa. 26 runs were performed up to a 22 MPa for S_{hmax}. After following the same procedures, the best fit, the upper limit, and the lower limit lines and Equations 29, 30, and 31 were obtained. The numerical results of this part are presented in Appendix D.

$$S_{hmax} = \frac{\left(e^{2.26\frac{r_d}{r}-2.34} \right) C_0 + S_{hmin}}{3} \quad (29)$$

$$S_{hmax} = \frac{\left(e^{2.13\frac{r_d}{r}-2.19} \right) C_0 + S_{hmin}}{3} \quad (30)$$

$$S_{hmax} = \frac{\left(e^{2.07\frac{r_d}{r}-2.06} \right) C_0 + S_{hmin}}{3} \quad (31)$$

If the actual breakout depths are used in Equations 29, 30, and 31, the values of S_{hmax} will be as in Table 5.6.

Table 5-6: *Normalized Breakout Depth Percentage of the Actual Field Data and Corresponding S_{hmax} Values on the Best Fit, the Upper Limit, and the Lower Limit Lines for S_{hmin}= 2.9 MPa*

Normalized Breakout Depth Percentage	**S_{hmax} (MPa) on the Best Fit**	**S_{hmax} (MPa) on the Upper Limit**	**S_{hmax} (MPa) on the Lower Limit**
24.44	15.82	15.55	16.41
16.67	13.43	13.33	14.12
13.33	12.52	12.48	13.24
31.11	18.24	17.77	18.70
23.33	15.45	15.21	16.06
22.22	15.09	14.87	15.72
30.00	17.81	17.38	18.30
13.33	12.52	12.48	13.24

There are two different groups of equations developed for the field with those analyses of 2.9 MPa and 3.5 MPa of S_{hmin}. Two equation groups were integrated to be correlated on average. To obtain the curves of average correlation, S_{hmin} was taken as 3.2 MPa and all normalized breakout depth values were combined into a single graph. In this way, the average lines were created. The equations of those three lines (the best fit, the upper limit, and the lower limit lines) are Equations 32, 33, and 34.

$$S_{hmax} = \frac{\left(e^{2.13\frac{r_d}{r}-2.16} \right) C_0 + S_{hmin}}{3} \quad (32)$$

$$S_{hmax} = \frac{\left(e^{2.17\frac{r_d}{r}-2.25} \right) C_0 + S_{hmin}}{3} \quad (33)$$

$$S_{hmax} = \frac{\left(e^{2.08\frac{r_d}{r}-2.05} \right) C_0 + S_{hmin}}{3} \quad (34)$$

If the actual breakout depths are implemented into Equations 29, 30, and 31, the values of S_{hmax} will be as in Table 5.7.

Besides the breakout depth analysis, the breakouts in numerical models were analyzed in terms of comparison of half of breakout width versus S_{hmax} from the theory developed by Barton et al (1988) (Equation 10), and numerical results as seen in Figures 5.6 and 5.7.

Table 5-7: *Normalized Breakout Depth Percentage of the Actual Field Data and Corresponding S_{hmax} Values on the Best Fit, the Upper Limit, and the Lower Limit Lines for S_{hmin}= 3.2 MPa*

Normalized Breakout Depth Percentage	**S_{hmax} (MPa) on the Best Fit**	**S_{hmax} (MPa) on the Upper Limit**	**S_{hmax} (MPa) on the Lower Limit**
24.44	16.06	15.58	16.78
16.67	13.77	13.32	14.43
13.33	12.90	12.46	13.53
31.11	18.35	17.84	19.11
23.33	15.71	15.23	16.42
22.22	15.36	14.89	16.07
30.00	17.94	17.44	18.70
13.33	12.90	12.46	13.53

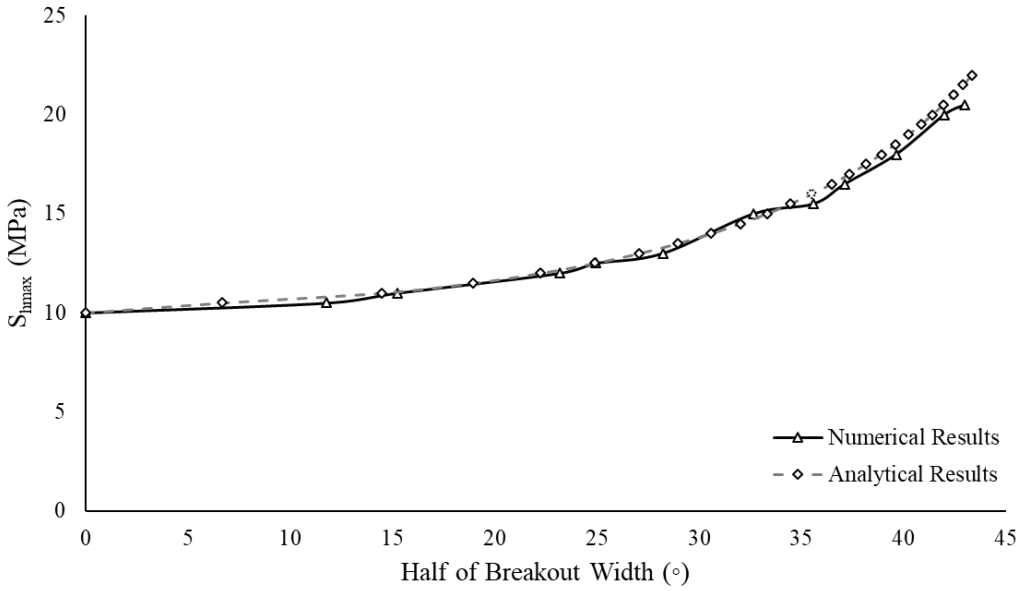

Figure 5-6: Comparison of Equation 10 (Barton et al., 1988) and Numerical Results for S_{hmin}= 3.5 MPa

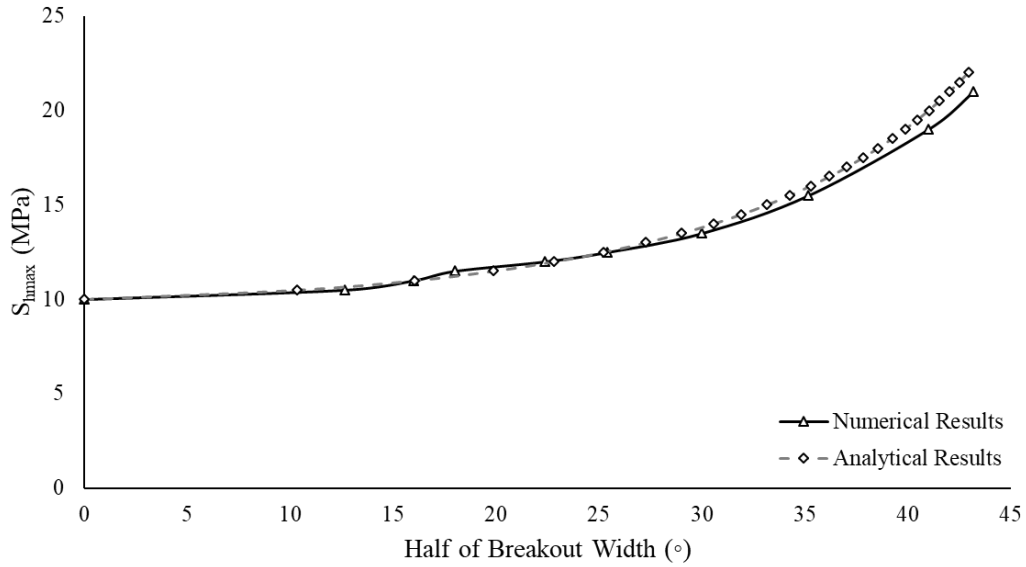

Figure 5-7: Comparison of Equation 10 (Barton et al., 1988) and Numerical Results for S_{hmin}= 2.9 MPa

5.3.2. Trona Results

The analyses for trona were done with 3.5 MPa and 2.9 MPa of S_{hmin}, S_{hmax} was increased by 0.2 MPa increments with the given parameters of trona. The strength values of trona are smaller compared to marl, the increments of S_{hmax} are required to be kept smaller because the development of breakouts were more sensitive in smaller increments for trona. There were 39 and 28 runs done for 3.5 MPa and 2.9 MPa of S_{hmin}, respectively. The reason why there are different numbers of run is that there was no significant change after a certain level of S_{hmax}. Following the same procedure in marl, there are three logarithmic best fit curves created for the field, Figure 5.8. The remaining curves and numerical analyses results are presented in Appendix D.

According to these best fit correlation curves, there are 9 equations of the best fit, the upper limit, and the lower limit lines (35, 36, 37, 38, 39, 40, 41, 42, 43) for 2.9 MPa and 3.5 MPa of S_{hmin} and the average of both, respectively.

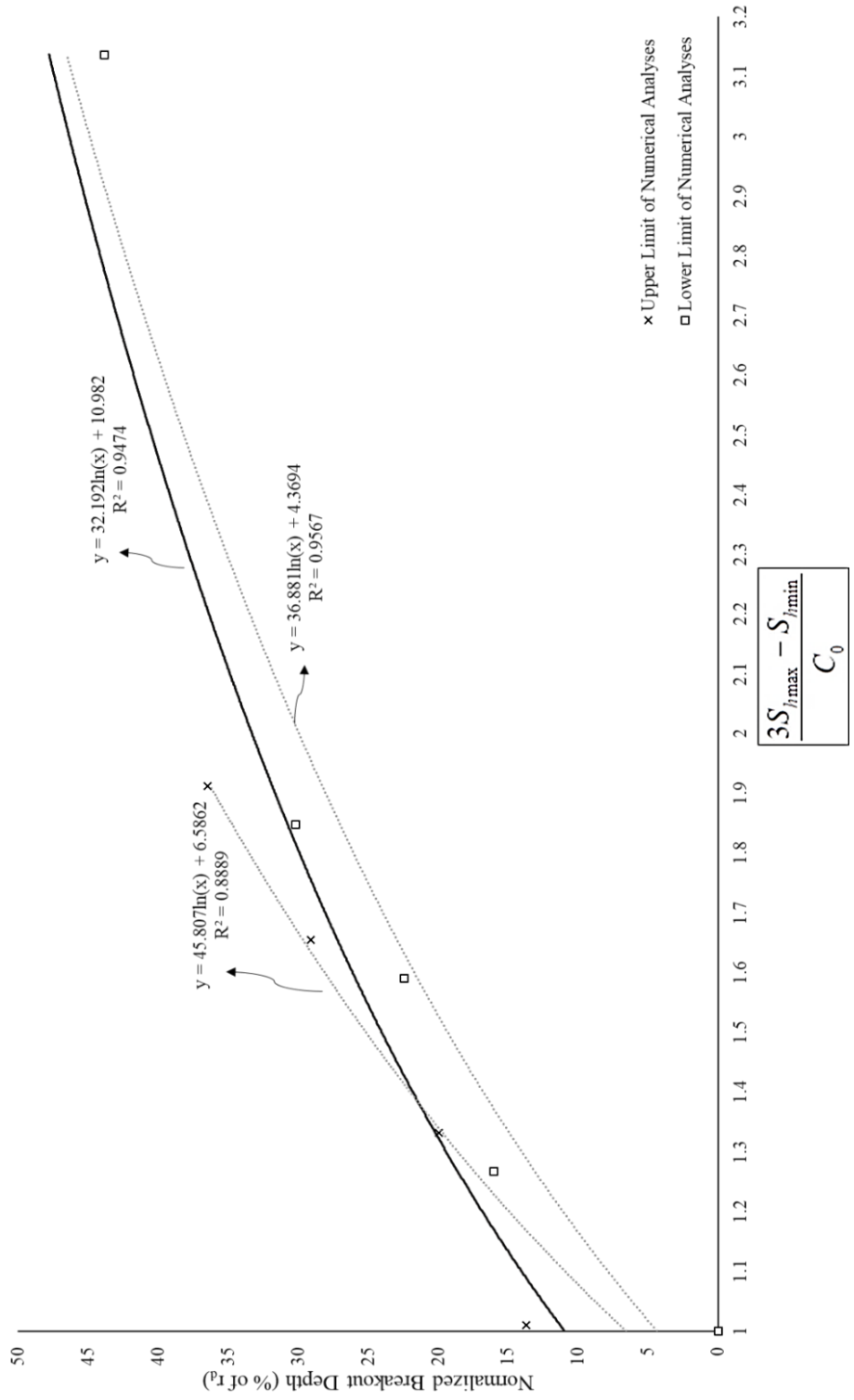

Figure 5-8: Correlation between Normalized Depth Percentage and Stress-Strength Ratio of the Trona for S_{hmin}=3.5 MPa

For S_{hmin}=3.5 MPa,

$$S_{hmax} = \frac{\left(e^{2.11\frac{r_d}{r}-2.45} \right) C_0 + S_{hmin}}{3} \quad (35)$$

$$S_{hmax} = \frac{\left(e^{2.18\frac{r_d}{r}-2.33} \right) C_0 + S_{hmin}}{3} \quad (36)$$

$$S_{hmax} = \frac{\left(e^{2.71\frac{r_d}{r}-2.83} \right) C_0 + S_{hmin}}{3} \quad (37)$$

For S_{hmin}=2.9 MPa,

$$S_{hmax} = \frac{\left(e^{2.88\frac{r_d}{r}-1.11} \right) C_0 + S_{hmin}}{3} \quad (38)$$

$$S_{hmax} = \frac{\left(e^{2.88\frac{r_d}{r}-1.11} \right) C_0 + S_{hmin}}{3} \quad (39)$$

$$S_{hmax} = \frac{\left(e^{2.21\frac{r_d}{r}-2.27} \right) C_0 + S_{hmin}}{3} \quad (40)$$

For the average,

$$S_{hmax} = \frac{\left(e^{2.99\frac{r_d}{r}-3.31} \right) C_0 + S_{hmin}}{3} \quad (41)$$

$$S_{hmax} = \frac{\left(e^{2.17\frac{r_d}{r}-2.33}\right)C_0 + S_{hmin}}{3} \quad (42)$$

$$S_{hmax} = \frac{\left(e^{2.62\frac{r_d}{r}-2.73}\right)C_0 + S_{hmin}}{3} \quad (43)$$

However, it is not possible to represent the estimation of S_{hmax} as a range since there was no breakout in trona section of the borehole. Therefore, it is only possible to argue that the value of S_{hmax} is less than 3.1 MPa and 3.5 MPa for 2.9 MPa and 3.5 MPa of S_{hmin}, respectively.

Furthermore, in aspect of angular analysis, the comparison of Equation 10 (Barton et al., 1988) and numerical results showed that S_{hmax} is less than 3.9 MPa and 4.1 MPa for 2.9 MPa and 3.5 MPa of S_{hmin}, respectively, see Appendix D for the curves based the change of breakout width.

Table 5-8: *The S_{hmax} Estimation of Marl Depending on r_d and ϕ_b for a Given S_{hmin}*

S_{hmin}	**S_{hmax} (MPa) (Based on r_d)**	**S_{hmax} (MPa) (Based on ϕ_b)**
2.90	12.48-18.70	11.50-12.50
3.20	12.46-19.11	-
3.50	12.72-19.20	11.70-12.50

Table 5-9: *The S_{hmax} Estimation of the Trona Depending on r_d and ϕ_b for a Given S_{hmin}*

S_{hmin}	**S_{hmax} (MPa) (Based on r_d)**	**S_{hmax} (MPa) (Based on ϕ_b)**
2.90	<3.10	3.90
3.20	<3.30	-
3.50	<3.50	4.10

5.4. Comparison of Numerical and Analytical Results

In order to estimate the magnitude of S_{hmax}, there are 2 different theories mentioned in Chapter 2. One of them is based on Kirsch's solution (Equation 1-2), and the other one is developed by Barton et al (1988) (Equation 10). In addition to these, numerical analysis results presented some stress results depending on breakout depth and width. The stress estimations were done for two different units at different S_{hmin} magnitudes with a given rock parameter. According to those studies, all stress results are given in Table 5.10 and Table 5.11.

Table 5-10: *The S_{hmax} Estimation Results of the Marl by Equation 2 (Kirsch's solution), Equation 10 (Barton et al., 1988), and Numerical Analyses*

	Analytical		**Numerical**	
S_{hmin}	**S_{hmax} (MPa) (Equation 2)**	**S_{hmax} (MPa) (Equation 10)**	**S_{hmax} (MPa) (Based on r_d)**	**S_{hmax} (MPa) (Based on ϕ_b)**
2.90	10.08	11.42-12.33	12.48-18.70	11.50-12.50
3.20	10.18	11.47-12.37	12.46-19.11	-
3.50	10.28	11.54-12.40	12.72-19.20	11.70-12.50

Table 5-11: *The S_{hmax} Estimation Results of the Trona by Equation 2 (Kirsch's solution), Equation 10 (Barton et al., 1988), and Numerical Analyses*

	Analytical		**Numerical**	
S_{hmin}	**S_{hmax} (MPa) (Equation 2)**	**S_{hmax} (MPa) (Equation 10)**	**S_{hmax} (MPa) (Based on r_d)**	**S_{hmax} (MPa) (Based on ϕ_b)**
2.90	4.15	4.15	<3.10	<3.90
3.20	4.25	4.25	<3.30	-
3.50	4.35	4.35	<3.50	<4.10

Three studies show some differences in S_{hmax} estimation. ϕ_b being too small might be one of the reasons. It should be noted that analytical studies are based on linear elastic assumptions. If numerical results, based on ϕ_b are considered, it can be seen that they

give close values to the magnitudes by Equation 2 and 10. The reason of this might be that the stress is equal to the strength at the edge of the breakouts. Furthermore, for the analytical solution based on Equation 10, since there is no breakout in trona, it results in θ_b is equal to 0. In this case, Equation 2 and 10 are equal to each other, therefore, it is possible to explain it in terms of θ_b, in spite of no breakout.

Breakout depth is another part of the numerical analyses to determine the S_{hmax}. It gives a very wide range for the magnitude; there were three curves defined for a given S_{hmin} level, and it can be observed that the lower levels of the ranges are close to the other stress magnitudes, while they are greater at the upper level of the ranges for Marl. In order to explain the differences, the used modeling software or time dependent breakout growth might be considered as the reasons. FLAC might cause fewer yielded elements as compared to the actual case on field, in other words, the models by FLAC might lead to the underestimation of the breakout depths. Besides, time dependent growth of borehole breakout might be the reason; it means that the breakout formed just after drilling might not be the same with the results obtained from FMI log due to the time passed between drilling and borehole imaging. Therefore, if the r_d obtained are smaller, then the results depending on r_d from numerical analysis could be close to the other ones.

Since there were no breakout results along trona unit, it is not possible to present a range for the S_{hmax} using breakout depth. However, upper limit for S_{hmax} can be presented. The same reason is valid for S_{hmax}, depending on ϕ_b. In comparison of Kirsch's solution and Barton's theory, they are both giving the same result since both of them are based on elasticity theory and if the breakout angle is assigned to be zero in Equation 10 due to no breakout along the trona unit, it would be the same equation by Kirsch's solution.

When the whole depth of V040A borehole was considered. S_{hmax} is in the range of 10.08 to 19.20 MPa for the marl section, which corresponds to a depth of 78m to 150 m. However, S_{hmax} for the deeper parts of the borehole (>400 m trona section) is less

than 4.35 MPa. The reason for such a S_{hmax} change might be attributed to local fault or a tectonic difference along the depth of the borehole. This argument might be checked with active fault mapping of the corresponding area.

CHAPTER 6

CONCLUSIONS AND RECOMMENDATIONS

The objectives of this thesis are to estimate the orientation and magnitude of horizontal stresses, and to introduce a methodology to estimate the S_{hmax} by borehole breakout using its depth and width. The other objective is to compare the results from analytical theories and numerical models, and to find out the possible reasons of the differences among them. Therefore, this thesis study covers FMI log analysis for the determination of horizontal stresses, laboratory studies for the rock parameters, the field studies (LOTs) for the estimation of the magnitude of S_{hmin} and the numerical studies to estimate the magnitude of S_{hmax}.

Main conclusions from this thesis are as follows:

i. According to FMI log analyses (resistivity image and caliper log analyses), 8 breakouts were determined while the borehole does not include any DIF data. The direction of S_{hmin} was estimated at the azimuth of N78.75E, and N11.25W is the direction of S_{hmax} since all the breakouts are from the marl section (78 m – 150 m). it can be argued that S_{hmin} and S_{hmax} orientations presented here are only for this portion of the borehole.

ii. The magnitude of S_{hmin} was determined by LOTs, there were two different values for it. One of them is 3.5 MPa found by LOT result of the borehole V040A, while the other one is 2.9 MPa found by inverse distance square method result estimated using LOT results of all boreholes in the field.

iii. The magnitude of S_{hmax} was determined by analytical and numerical studies for marl and trona units regarding the borehole V040A. Analytical results are based on Kirsch's solution and Barton et al (1988). Numerical analysis results are based on breakout depth and width separately.

For Marl;

- According to Kirsch's solution, S_{hmax} is in the range of 10.08 MPa and 10.28 MPa.
- According to Barton et al (1988), S_{hmax} is in the range of 11.42 MPa and 12.40 MPa.
- According to numerical analysis depending on r_d, S_{hmax} is in the range of 12.46 MPa and 19.20 MPa.
- According to numerical analysis depending on ϕ_b, S_{hmax} is in the range of 11.50 MPa and 12.50 MPa.

For Trona;

- According to Kirsch's solution, S_{hmax} is in the range of 4.15 MPa and 4.35 MPa.
- According to Barton et al (1988), S_{hmax} is in the range of 4.15 MPa and 4.35 MPa.
- According to numerical analysis depending on r_d, S_{hmax} is less than 3.50 MPa.
- According to numerical analysis depending on ϕ_b, S_{hmax} is less than 4.10 MPa.

There are 4 different stress levels for those two units, however, the most reliable values are from the theory developed by Barton et al (1988).

Recommendations are listed below:

i. One way of checking the significance of this orientation can be cross checking this information on the topography of the area. However, the topography does not reveal any mountain range tectonism to suggest that the S_{hmax} direction is N11.25W. However, this should not be misinterpreted

either since all the failures are in the depth range of 78m-145m. Therefore, local faults extending to a certain depth might be creating this result as well. Fault maps of the area might be also useful for the interpretation of the estimated stress orientation. For the first 50m - 90 m part of the borehole, lithology of marl, and the last 300 m part of it, lithology of marl and shale, there were no signal of failures. Since there was neither DIF or breakout for these portions, it means that deviatoric stresses might be low compared to the compressive/tensile strength of the lithology (marl or marl – shale), so that stresses could not cause compressive or tensile failure. On the other hand, since the breakouts were determined in the marl, this might also be interpreted as the deviatoric stresses at the depth range of 75m – 145m is higher or the uniaxial compressive strength of marl is weak compared to the stress.

ii. More FMI log should be performed on the other boreholes of the field for more accurate breakout and DIF results should be obtained.

iii. As mentioned in Chapter 4, different pressure integrity tests can be conducted for distinct purposes besides LOT. In stress estimation, XLOT/ELOT provides more reliable results. They should be used in further studies.

iv. As mentioned in the comparison of analytical and numerical results, there are differences found for the magnitudes of S_{hmax}. One of the reasons might be the models created in FLAC could not give proper fracture propagation, hence the software that can use fracture toughness as an input for fracture propagation should be used to obtain more accurate r_d results in stress estimation.

v. Time dependent crack growth is to depend on subcritical crack growth, causing time dependency in borehole breakout growth (Zheng et al., 1989). It is considered that there are some reasons resulting in these subcritical

cracks in rocks; these are stress corrosion, dissolution, diffusion, and microplasticity etc. (Atkinson, 1984). It is also proposed that breakout growth is strongly correlated with chemical and hydrologic conditions. Furthermore, absorption of strain energy through inelastic deformation may also cause time dependent failure after the rock failure begins. After breakouts are initiated, although their widths stay stable, they have a tendency to deepen (Zoback, 2007). Therefore, the time passed between the drilling and the borehole imaging should be kept as short as possible.

vi. Anisotropic material behavior can be accounted in the further studies since it can be determinant in the stress distribution in the rocks.

REFERENCES

Addis, M. A., Hanssen, T. H., Yassir, N., Willoughby, D. R., & Enever, J. (1998). A comparison of leak-off test and extended leak-off test data for stress estimation. In SPE/ISRM Rock Mechanics in Petroleum Engineering. Society of Petroleum Engineers.

Al-Ajmi, A. M., & Zimmerman, R. W. (2005). Relation between the Mogi and the Coulomb failure criteria. International Journal of Rock Mechanics and Mining Sciences, 42(3), 431-439.

Allerstorfer, C. (2011). Investigation of the "Plastic Behavior" Region in Leak Off Tests. Master's thesis Montanuniversität Leoben, Austria

Alluad, L. A., & Ringot, J. (1969). The high resolution dipmeter tool. The Log Analyst, 10(03).

Amadei, B., & Stephansson, O. (1997). Rock stress and its measurement. Springer Science & Business Media.

Anderson, E. M. (1951). The dynamics of faulting and dyke formation with applications to Britain. Hafner Pub. Co..

Arslan, I., Akin, S., Karakece, Y., & Korucu, O. (2007). Is Bati Raman Heavy Oil Field a Triple Porosity System?. In SPE/EAGE Reservoir Characterization and Simulation Conference. Society of Petroleum Engineers.

Asquith, G. B., Krygowski, D., & Gibson, C. R. (2004). Basic well log analysis (Vol. 16). Tulsa: American Association of Petroleum Geologists.

Atkinson, B. K. (1984). Subcritical crack growth in geological materials. Journal of Geophysical Research: Solid Earth, 89(B6), 4077-4114.

Babcock, E. A. (1978). Measurement of subsurface fractures from dipmeter logs. AAPG Bulletin, 62(7), 1111-1126.

Barton, C., Zoback, M. & Burns, K. (1988). In-situ stress orientation and magnitude at the Fenton Geothermal Site, New Mexico, determined from wellbore breakouts. Geophysical Research Letters, 15(5), pp.467-470.

Bell, J. S. (1989). "Investigating stress regimes in sedimentary basins using information from oil industry wireline logs and drilling records." Geological Applications of Wireline Logs. Special Publication 48(Geological Society of London), 305–325.

Bell, J. S., & Gough, D. I. (1979). Northeast-southwest compressive stress in Alberta evidence from oil wells. Earth and planetary science letters, 45(2), 475-482.

Bell, J. S. & Gough, D. I. (1983). The use of borehole breakouts in the study of crustal stress, in Hydraulic fracturing stress measurements. D.C, National Academy Press, Washington.

Brown, E. T., & Hoek, E. (1978). Trends in relationships between measured in-situ stresses and depth. In International Journal of Rock Mechanics and Mining Sciences & Geomechanics Abstracts (Vol. 15, No. 4, pp. 211-215). Pergamon.

Brown, R. O., & Forgotson, J. M. (1980). Predicting the orientation of hydraulically created fractures in the Cotton Valley Formation of east Texas. In SPE Annual Technical Conference and Exhibition. Society of Petroleum Engineers.

Brudy, M. & Zoback, M. D. (1999). "Drilling-induced tensile wall-fractures: implications for the determination of in situ stress orientation and magnitude." International Journal of Rock Mechanics and Mining Sciences, 136, 191–215.

Camur, M. Z., Er, C., & Yazicigil, H. (2008). Modeling of lithology induced chemical anomalies in the aquifer systems of the Kazan Trona deposit area, Ankara, Turkey. Environmental geology, 54(4), 777-789.

Castillo, D. A. & Zoback, M. D. (1994). "Systematic variations in stress state in the Southern San Joaquin Valley: Inferences based on well-bore data and contemporary seismicity." American Association Petroleum Geologists Bulletin, 78(8), 1257–1275.

Colmenares, L. B. & Zoback, M. D. (2002). "A statistical evaluation of rock failure criteria constrained by polyaxial test data for five different rocks." International Journal of Rock Mechanics and Mining Sciences, 39, 695–729.

Cox, J. W. (1970). The high resolution dipmeter reveals dip-related borehole and formation characteristics. In SPWLA 11th Annual Logging Symposium. Society of Petrophysicists and Well-Log Analysts.

Cox, J. W. (1983). Long Axis Orientation In Elongated Roreholes And Its Correlation With Rock Stress Data. In SPWLA 24th Annual Logging Symposium. Society of Petrophysicists and Well-Log Analysts.

Drucker, D. & Prager,W. (1952). "Soil mechanics and plastic analysis or limit design." Quantitative and Applied Mathematics, 10, 157–165.

Ekstrom, M. P., Dahan, C. A., Chen, M.-Y., Lloyd, P. M., & Rossi, D. J. (1986). Formation Imaging with Microelectrical Scanning Arrays. Society of Petrophysicists and Well-Log Analysts.

Ewy, R. (1999). "Wellbore-stability predictions by use of a modified Lade criterion." SPE Drilling and Completion, 14(2), 85–91.

Fjaer, E., Holt, R. M., Horsrud, P. and Raen, A. M., 1992- Petroleum Related Rock Mechanics, 2nd Ed. pdf. (Vol.33) Elsevier.

Fordjor, C. K., Bell, J. S., & Gough, D. I. (1983). Breakouts in Alberta and stress in the North American plate. Canadian Journal of Earth Sciences, 20(9), 1445-1455.

Gallagher Jr, J. J., Friedman, M., Handin, J., & Sowers, G. M. (1974). Experimental studies relating to microfracture in sandstone. Tectonophysics, 21(3), 203-247.

Gough, D. I., Fordjor, C. K., & Bell, J. S. (1983). A stress province boundary and tractions on the North American plate. Nature, 305(5935), 619.

Haimson, B. C. & Herrick, C. G. (1989). Borehole breakouts and in situ stress. 12th Annual Energy- Sources Technology Conference and Exhibition, Houston, Texas.

Haimson, B. C., & Lee, C. F. (1995). Estimating in-situ stress conditions from borehole breakouts and corediscing experiment results ingranite. In Proceedings of the Workshop on Rock Stress Measurement at Great Depth. Tokyo, Japan: Eighth ISRN Congress.

Haimson, B., Lin, W., Oku, H., Hung, J. H., & Song, S. R. (2010). Integrating borehole-breakout dimensions, strength criteria, and leak-off test results, to constrain the state of stress across the Chelungpu Fault, Taiwan. Tectonophysics, 482(1-4), 65-72.

Hoek, E. & Brown, E. T. (1980). "Empirical strength criterion for rock masses." J. Geotechnical Engineering Div., 106, 1013–1035.

Hoek, E. & Brown, E. (1997). "Practical estimates of rock strength." International Journal of Rock Mechanics and Mining Sciences, 34(8), 1165–1186.

Hoek, E. & Brown, E. T. (1980). "Empirical strength criterion for rock masses." J. Geotechnical Engineering Div., 106, 1013–1035.

Hoek, E., Carranza-Torres, C., & Corkum, B. (2002). Hoek-Brown Failure Criterion – 2002 Edition. 5. North American Rock Mechanics Symposium, (pp. 267-273). Toronto.

Itasca, (2016) Manual of Fast Lagrangian Analysis of Continua (FLAC) User's Guide

Jaeger, J. C. & Cook, N. G. W. (1979). Fundamentals of Rock mechanics, 4th edn. New York, Chapman and Hall.

Moos, D. & Zoback, M. D. (1990). "Utilization of Observations of Well Bore Failure to Constrain the Orientation and Magnitude of Crustal Stresses: Application to Continental Deep Sea Drilling Project and Ocean Drilling Program Boreholes." J. Geophys. Res., 95, 9305–9325.

Ketin, İ. (1966), "Tectonic Units of Anatolia," MTA Bulletin, 66, pp. 23–34.

Kirsch, G. (1898). “Die Theorie der Elastizitat und die Bedurfnisse der Festigkeitslehre, Zeitschrift des Verlines Deutscher Ingenieure.” 42, 707.

Leeman, E. R. (1959). The measurement of changes in rock stress due to mining. Mine Quarry Eng., 25, 300-304.

Lin, H., Oh, J., Masoumi, H., Canbulat, I., Zhang, C., & Dou, L. (2018). A Review of In Situ Stress Measurement Techniques.

Ljunggren, C., Chang, Y., Janson, T., & Christiansson, R. (2003). An overview of rock stress measurement methods. International Journal of Rock Mechanics and Mining Sciences, 40(7-8), 975-989.

Luthi, S. (2001). Geological well logs: Their use in reservoir modeling. Springer Science & Business Media.

Paterson, M. S. (1978) Experimental Rock Deformation The Brittle Field. Springer-Verlag, New York.

Pendexter, C., & Rohn, R. E. (1954). Fractures induced during drilling. Journal of Petroleum Technology, 6(3), 15.

Plumb, R. A. & Cox, J.W. (1987). “Stress directions in eastern North America determined to 4.5 km from borehole elongation measurements.” Journal of Geophysical Research, 92, 4805–4816.

Plumb, R. A., & Hickman, S. H. (1985). Stress-induced borehole elongation: A comparison between the four-arm dipmeter and the borehole televiewer in the Auburn geothermal well. Journal of Geophysical Research: Solid Earth, 90(B7), 5513-5521.

Postler, D. P. (1997). Pressure integrity test interpretation. In SPE/IADC drilling conference. Society of Petroleum Engineers.

Rajabi, M., Tingay, M., & Heidbach, O. (2016). The present-day stress field of New South Wales, Australia. Australian Journal of Earth Sciences, 63(1), 1-21.

Raaen, A. M., & Brudy, M. (2001, January). Pump-in/flowback tests reduce the estimate of horizontal in-situ stress significantly. In SPE Annual Technical Conference and Exhibition. Society of Petroleum Engineers.

Schafer, J. N. (1979). A practical method of well evaluation and acreage development for the naturally fractured Austin Chalk formation. In SPWLA 20th Annual Logging Symposium. Society of Petrophysicists and Well-Log Analysts.

Slb.com. (2019). 1920s: The First Well Log | Schlumberger. [online] Available at: https://www.slb.com/who-we-are/our-history/1920s [Accessed 9 Jul. 2019].

Terzaghi, K., & Richart, F. E. (1952). Stresses in rock about cavities. Institution of Civil Engineers.

Tingay, M., Reinecker, J., & Müller, B. (2008). Borehole breakout and drilling-induced fracture analysis from image logs. World Stress Map Project, 1-8.

Tuncay, E., Ulusay, R., Watanabe, H., Tano, H., Yüzer, E., & Aydan, Ö. (2002). Acoustic emission (AE) technique: A preliminary investigation on the determination of in situ stresse by AE technique in Turkey. Yerbilimleri/Earthsciences, 25, 83-98.

Wawersik, W. R., & Fairhurst, C. H. (1970, September). A study of brittle rock fracture in laboratory compression experiments. In International Journal of Rock Mechanics and Mining Sciences & Geomechanics Abstracts (Vol. 7, No. 5, pp. 561-575). Pergamon.

White, A. J., Traugott, M. O., & Swarbrick, R. E. (2002). The use of leak-off tests as means of predicting minimum in-situ stress. Petroleum Geoscience, 8(2), 189-193.

Wiprut, D., Zoback, M., Hanssen, T. H., & Peska, P. (1997). Constraining the full stress tensor from observations of drilling-induced tensile fractures and leak-off tests: Application to borehole stability and sand production on the Norwegian margin. International Journal of Rock Mechanics and Mining Sciences, 34(3-4), 365-e1.

Yamamoto, K., 2003. Implementation of the extended leak-off test in deep wells in Japan. Rock Stress.

Zheng, Z., Kemeny, J. et al. (1989). "Analysis of borehole breakouts." Journal of Geophysical Research, 94(B6), 7171–7182.

Zoback, M., Moos, D., Mastin, L. and Anderson, R. (1985). Well bore breakouts and in situ stress. Journal of Geophysical Research: Solid Earth, 90(B7), pp.5523-5530.

Zoback, M. D., & Healy, J. H. (1992). In situ stress measurements to 3.5 km depth in the Cajon Pass scientific research borehole: Implications for the mechanics of crustal faulting. Journal of Geophysical Research: Solid Earth, 97(B4), 5039-5057.

Zoback, M. D., Apel, R., Baumgärtner, J., Brudy, M., Emmermann, R., Engeser, B., Fuchs K., Kessels W., Rischmüller H., Rummel F. & Vernik, L. (1993). Upper-crustal strength inferred from stress measurements to 6 km depth in the KTB borehole. Nature, 365(6447), 633.

Zoback, M. D., & Harjes, H. P. (1997). Injection-induced earthquakes and crustal stress at 9 km depth at the KTB deep drilling site, Germany. Journal of Geophysical Research: Solid Earth, 102(B8), 18477-18491.

Zoback, M. D. (2007). Reservoir geomechanics. Cambridge University Press.

APPENDICES

A. FMI LOGS

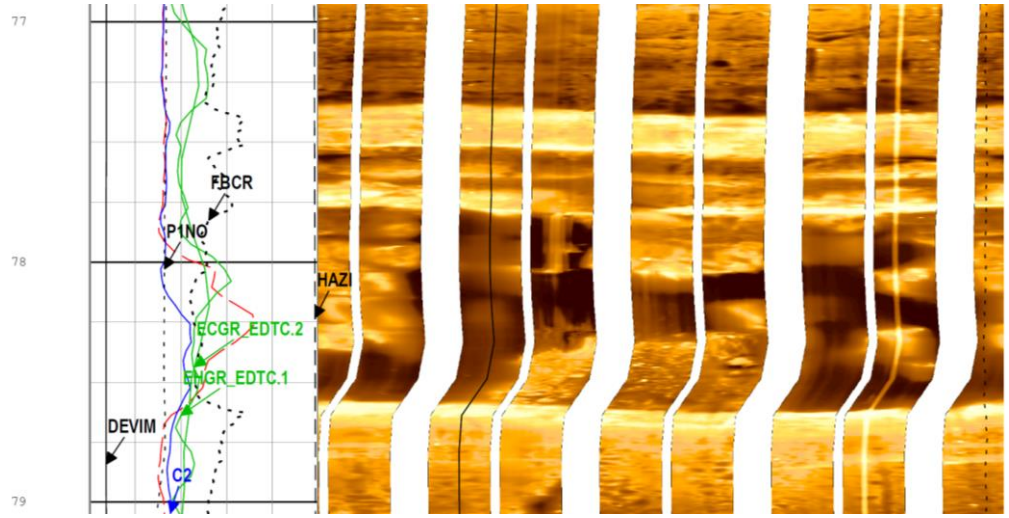

Figure A.1: FMI image of the interval from 77.75 to 78.50 m (% of r = 24.44)

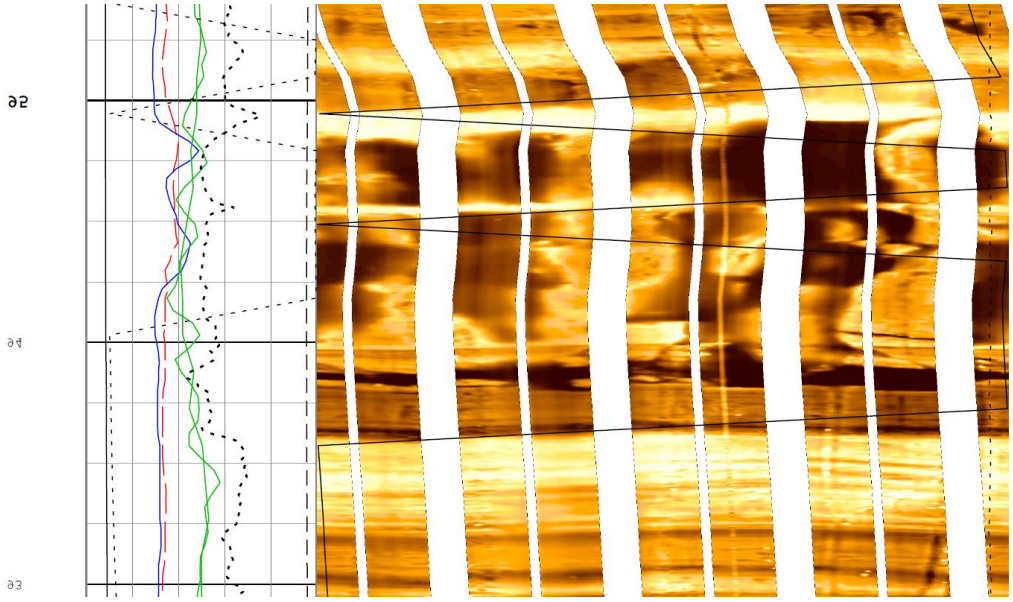

Figure A.2: FMI image of the interval from 94.00 to 95.00 m (% of r = 16.67)

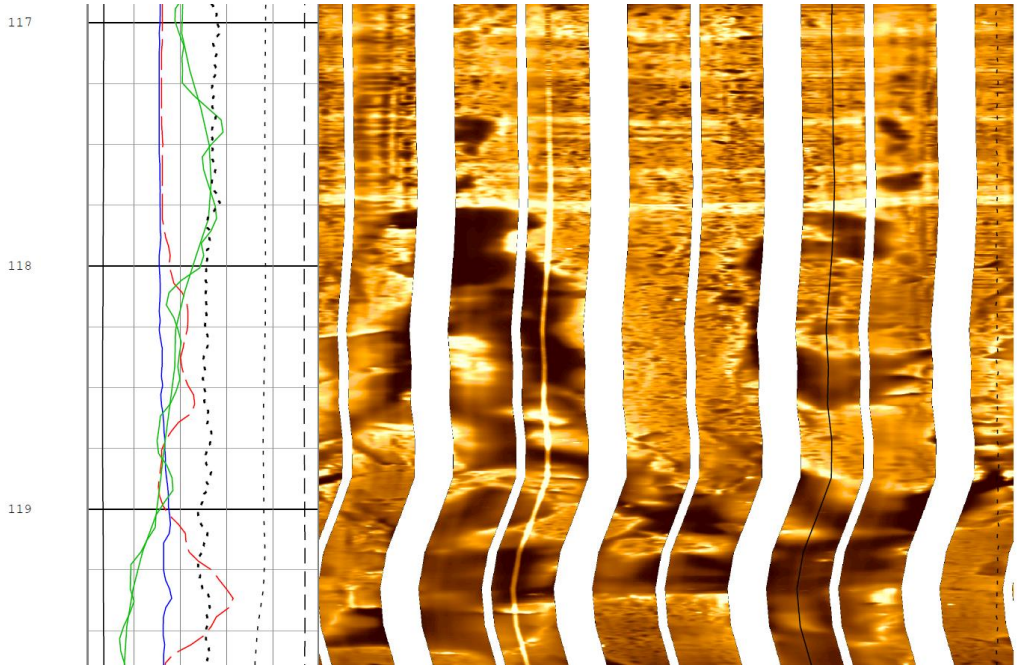

Figure A.3: FMI image of the interval from 117.75 to 118.50 m (% of r = 13.33)

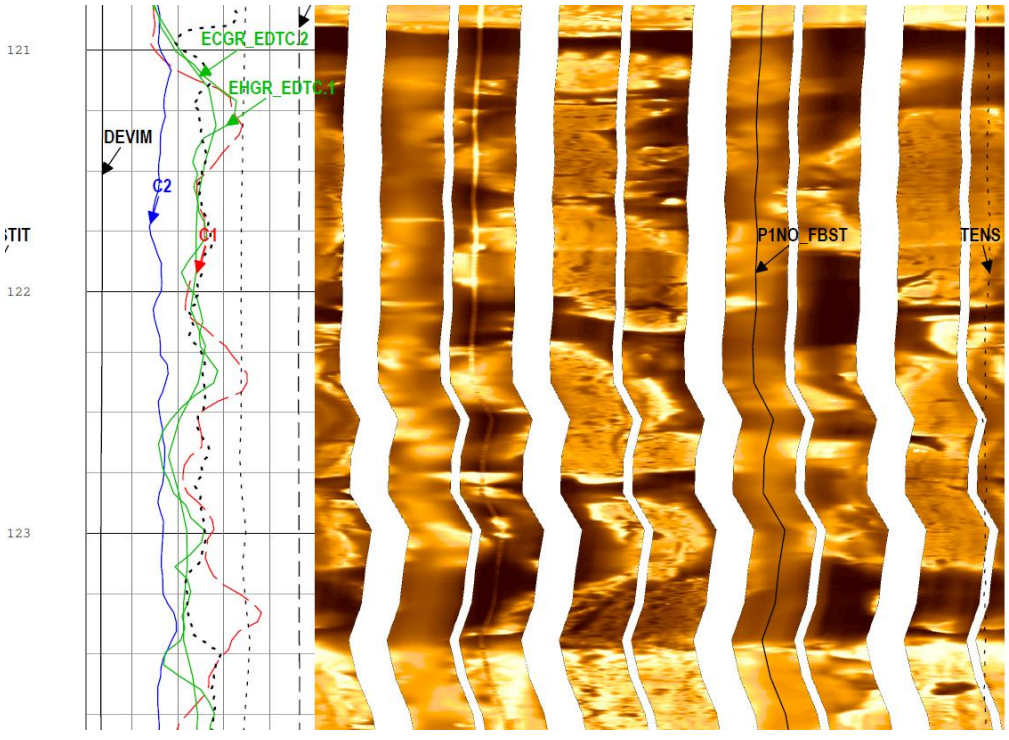

Figure A.4: FMI image of the interval from 121.00 to 123.50 m (% of r = 31.11)

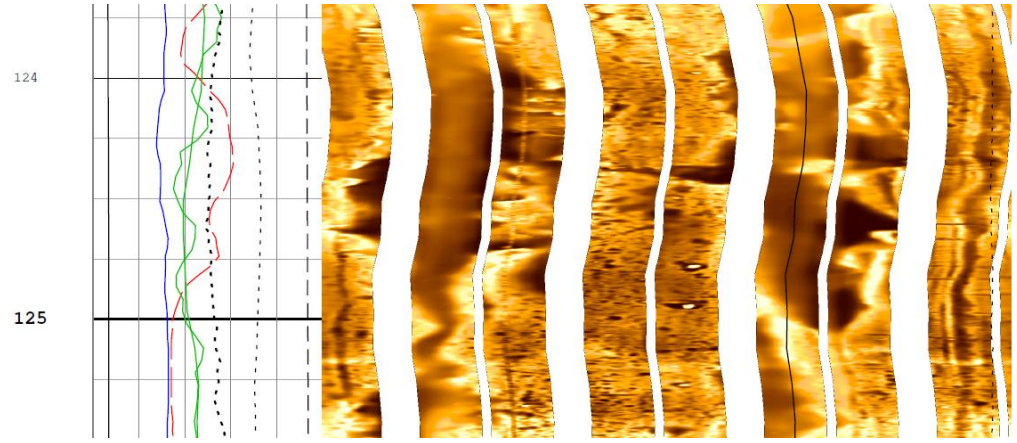

Figure A.5: FMI image of the interval from 124.00 to 125.00 m (% of r = 23.33)

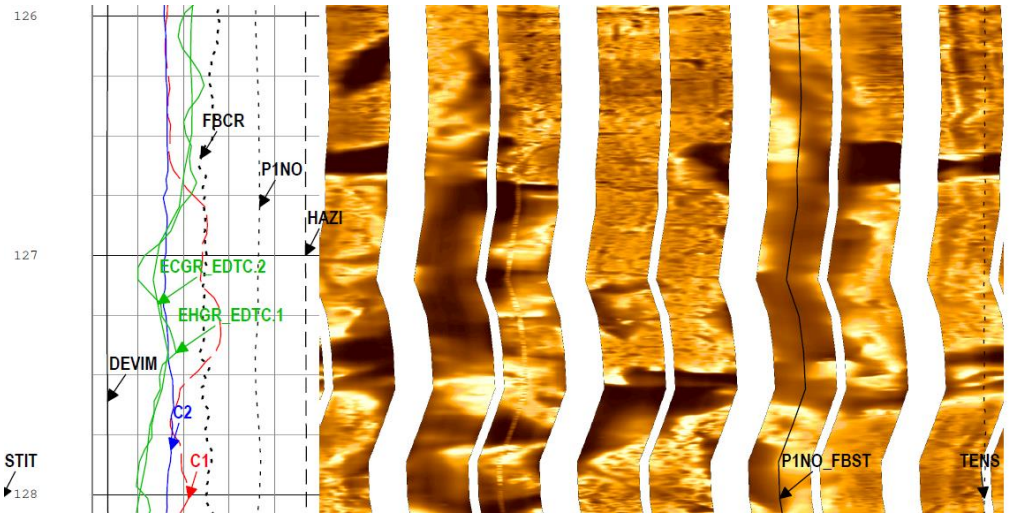

Figure A.6: FMI image of the interval from 126.50 to 127.50 m (% of r = 22.22)

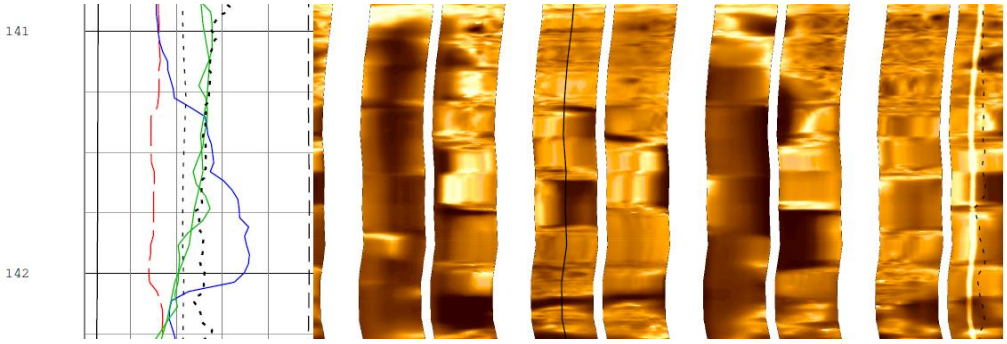

Figure A.7: FMI image of the interval from 141.00 to 142.00 m (% of r = 30.00)

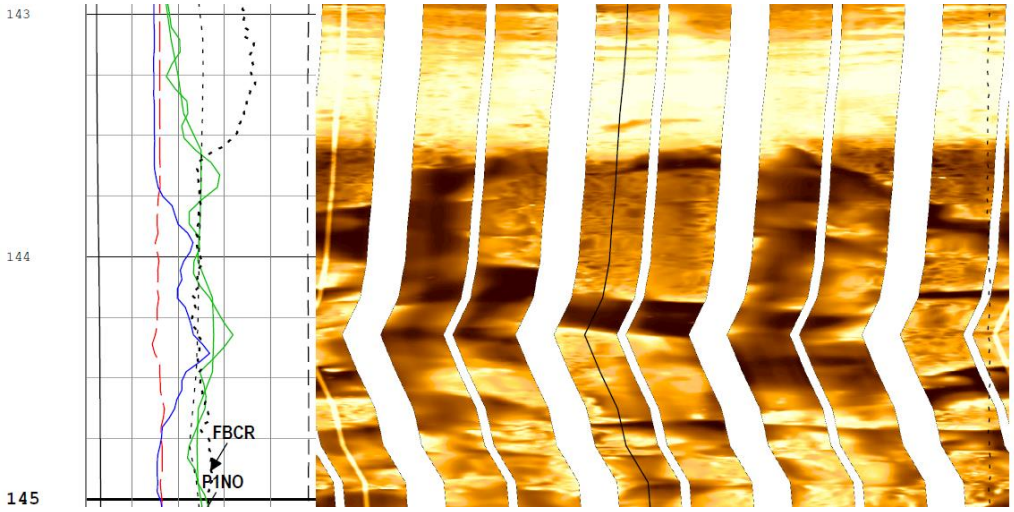

Figure A.8: FMI image of the interval from 143.75 to 144.75 m (% of r = 13.33)

B. LOT RESULTS

Table B.1: *LOT results of the Boreholes with distances to V040A*

Name of Borehole	Minimum Horizontal Stress (MPa)	Distance (m)
V040A	3.50	0.00
V040B	3.53	88.80
V039B	3.47	134,00
V048B	2.46	157.60
V048A	3.31	236.70
V048B	1.77	238.40
V028A	3.05	245.10
V030A	3.28	257.60
V029A	2.40	269.40
V050A	1.17	282.70
V041B	3.95	335.40
V028B	2.00	337.00
V051_1A	1.76	364.10
V051_1B	1.30	364.10
V030A	3.10	365.50
V030B	2.77	367.00
V044B	2.13	381.20
V051_1B	3.14	445.70
V019A	3.50	449.30
V018A	2.98	453.80
V032_1B	3.40	454.60
V042B	2.96	463.30
V032_2B	2.16	481.80
V020B	2.30	485.70
V016A	1.72	491.20
V016B	3.14	492.00
V042A	1.94	509.10
V044A	1.22	509.60
V052B	0.41	525.80
V054B	2.53	534.50
V018B	1.23	609.30
V053A	2.03	627.50
V033B	3.78	644.20
V033A	4.10	646.90
V052A	1.69	649.70

V043B	3.26	658.30
V054A	2.88	658.70
V023B	1.38	690.80
V043A	2.89	722.50
V024A	3.63	731.50
V034A	3.27	746.70
V034B	3.09	768.10
V024B	4.10	768.70
V011A	3.80	781.30
V058B	1.71	826.60
V035A	2.78	846.90
V025B	3.92	854.70
V012A	2.44	863.10
V057B	3.09	888.40
V011B	0.94	894.90
V045B	3.95	906.80
V058A	3.33	919.20
V013A	3.41	933.40
V026B	3.38	935.40
V035B	3.98	936.70
V056B	3.95	945.22
V013B	3.77	984.50
V055B	3.59	994.00
V037A	3.94	1013.20
V046B	3.11	1020.90
V007B	2.82	1040.30
V014A	2.56	1049.00
V014B	1.08	1049.00
V015B	1.14	1090.20
V059B	3.31	1113.20
V063A	3.94	1169.70
V064B	3.61	1331.30
V081B	2.57	1477.40

C. LABORATORY STUDIES

C.1 Stress-Strain Curves

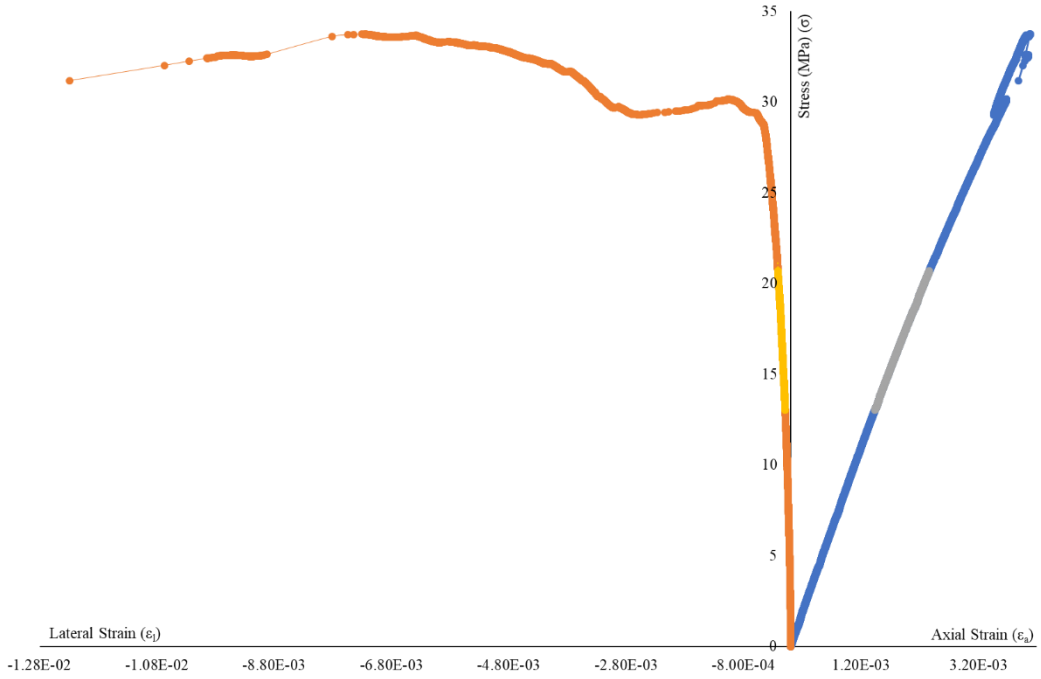

Figure C.9: Stress-Strain curve of the sample DE-1

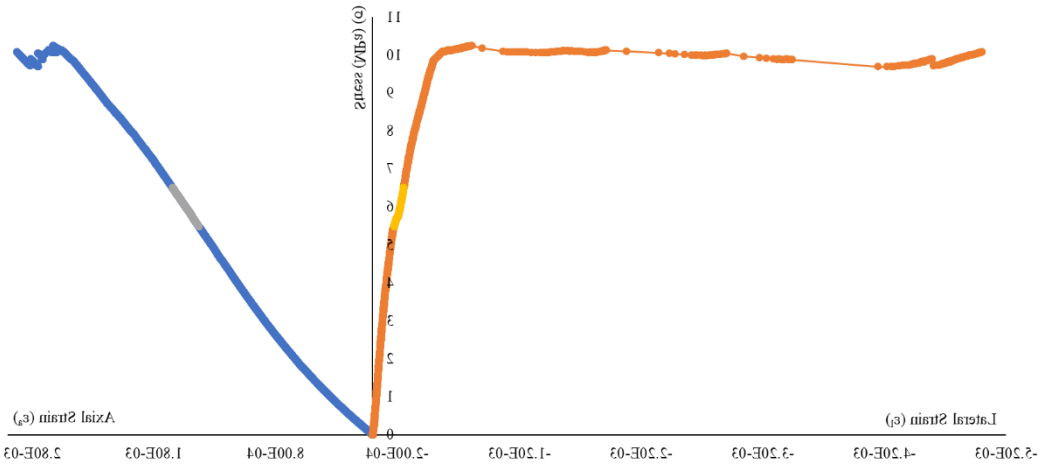

Figure C.10: Stress-Strain curve of the sample DE-2

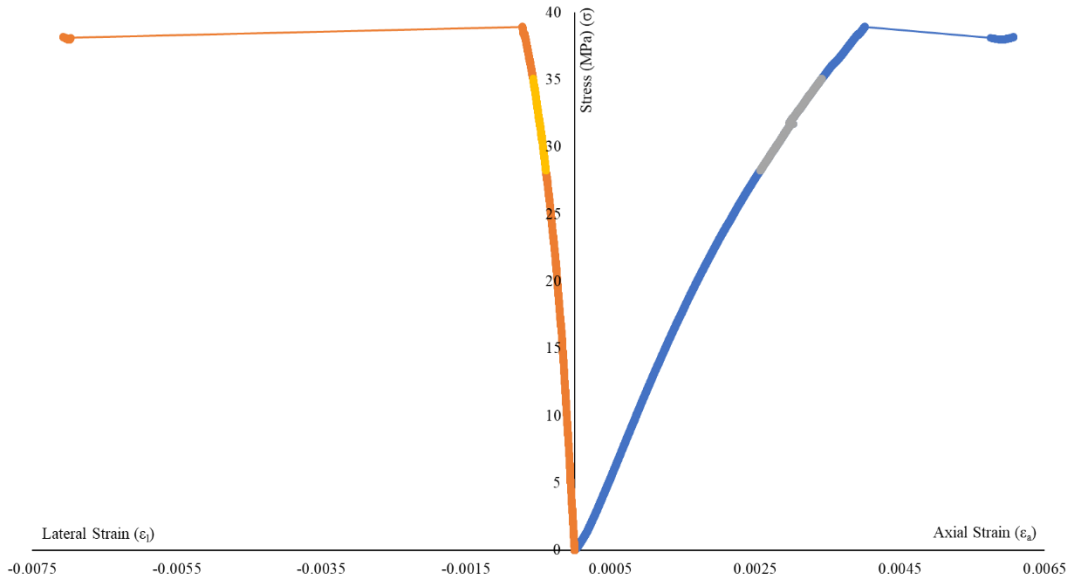

Figure C.11: Stress-Strain curve of the sample DE-3

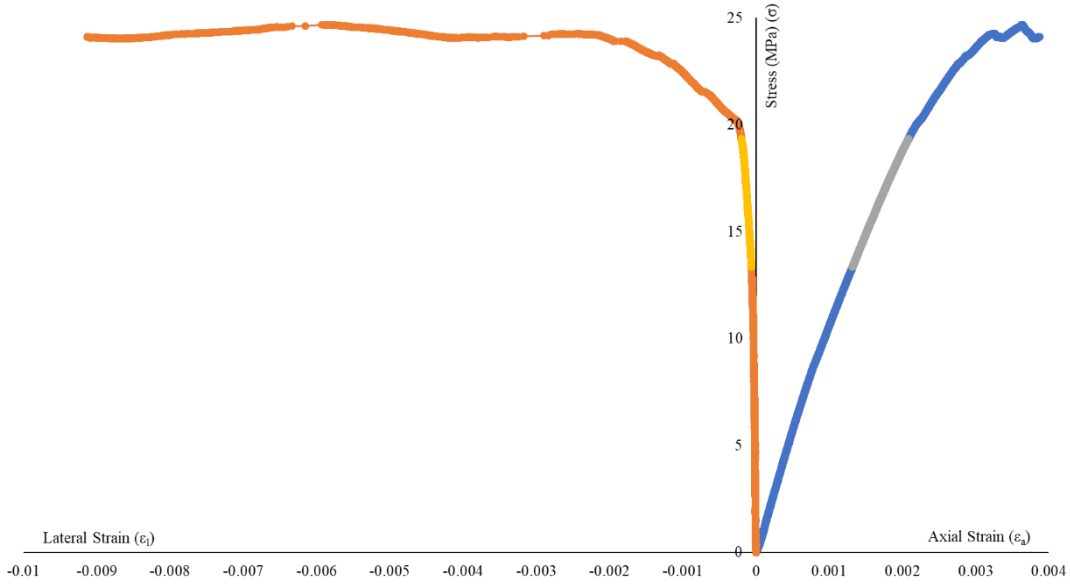

Figure C.12: Stress-Strain curve of the sample DE-4

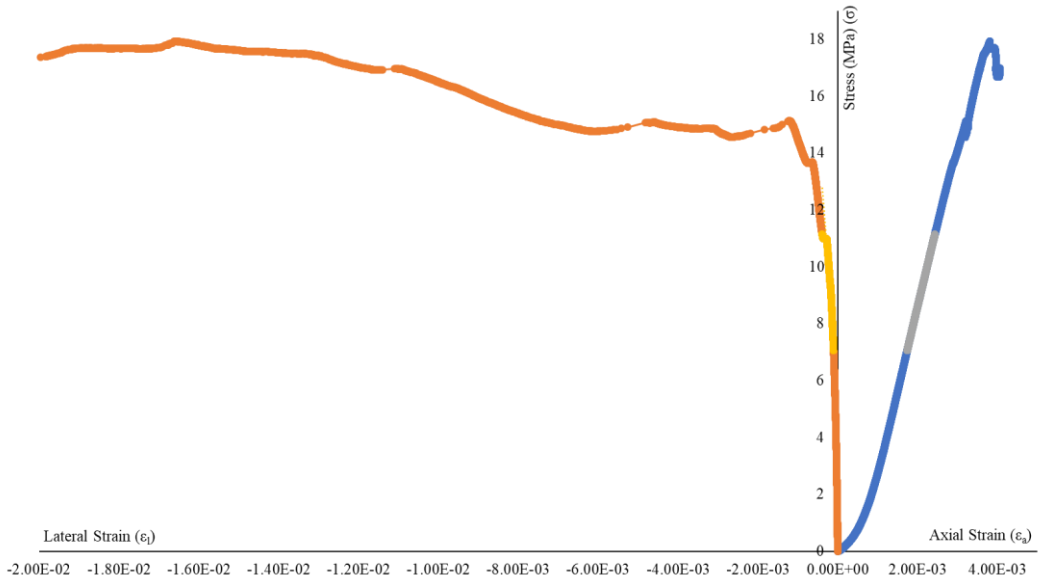

Figure C.13: Stress-Strain curve of the sample DE-5

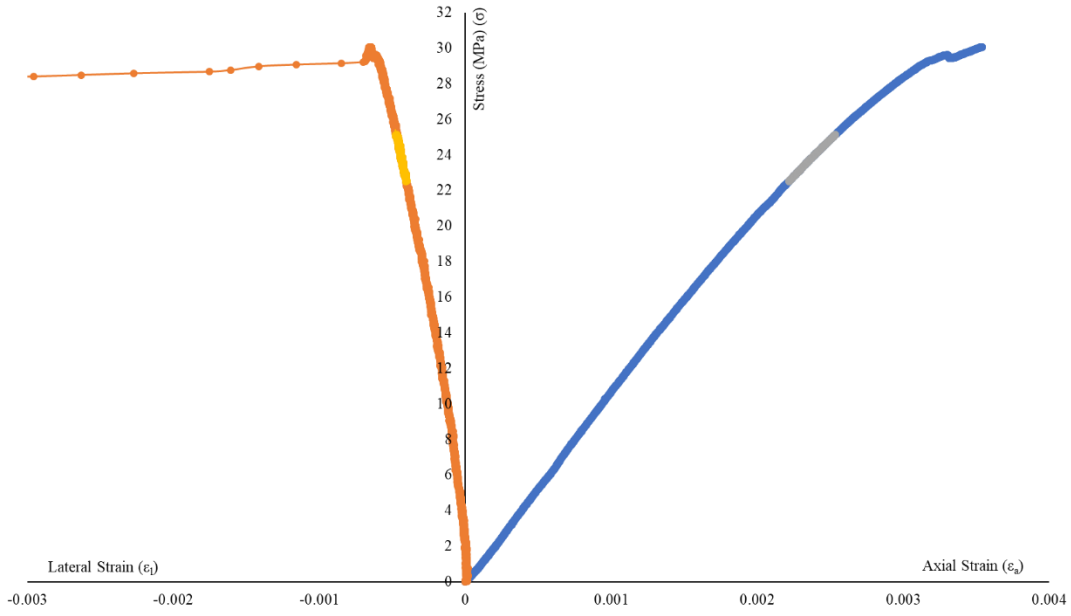

Figure C.14: Stress-Strain curve of the sample DE-6

C.2 Lateral-Axial Strain Curves

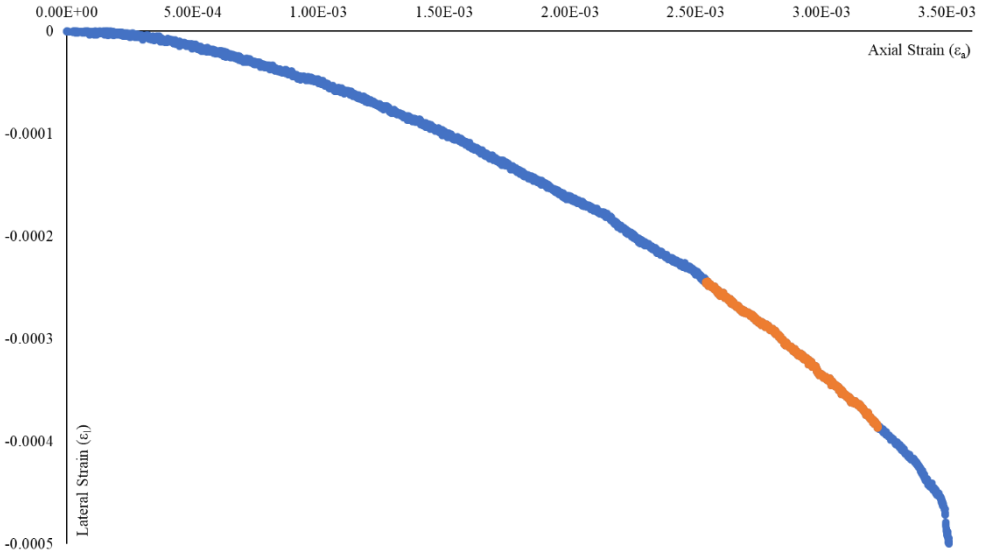

Figure C.15: Lateral-Axial strain curve of the sample DE-1

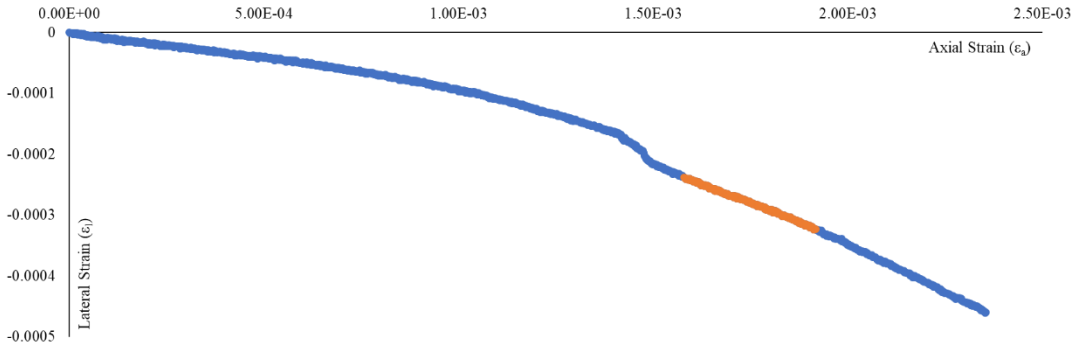

Figure C.16: Lateral-Axial strain curve of the sample DE-2

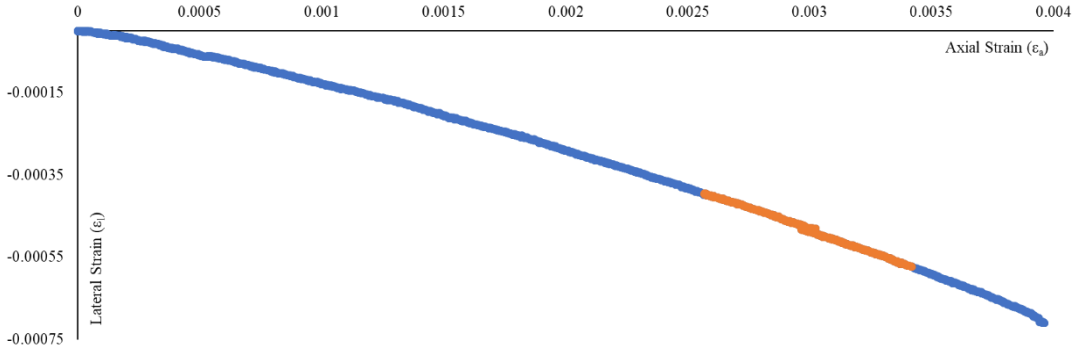

Figure C.17: Lateral-Axial strain curve of the sample DE-3

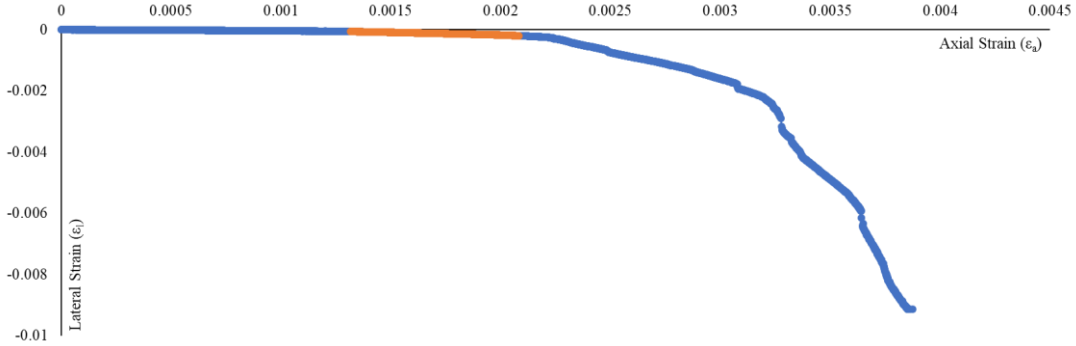

Figure C.18: Lateral-Axial strain curve of the sample DE-4

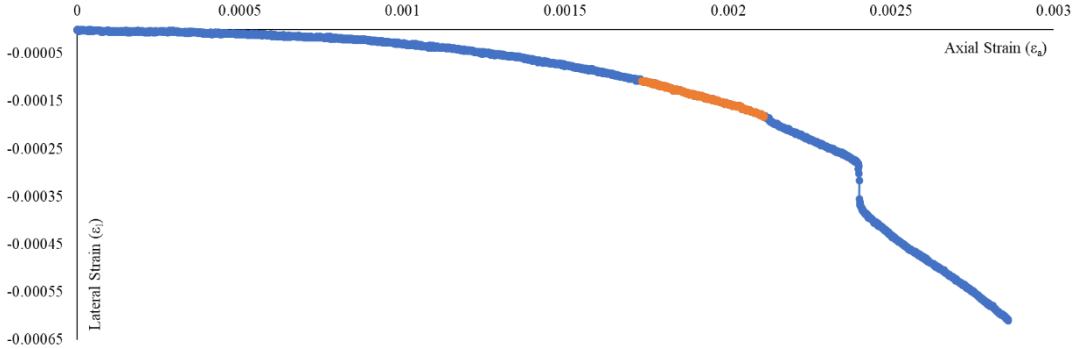

Figure C.19: Lateral-Axial strain curve of the sample DE-5

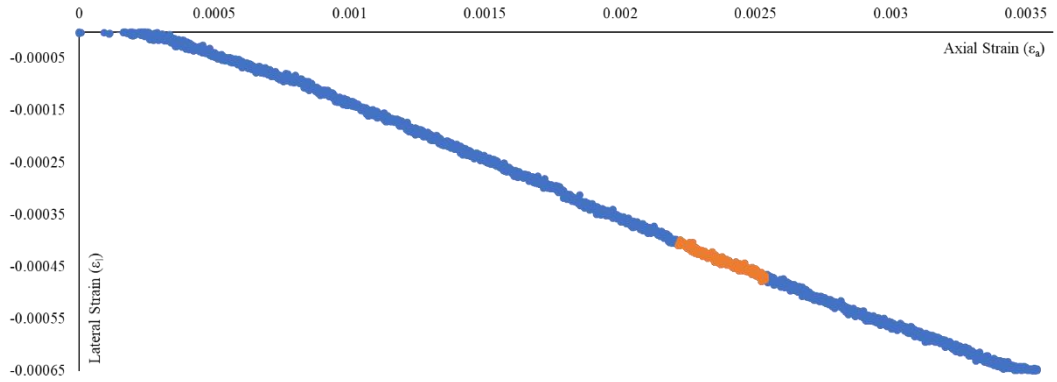

Figure C.20: Lateral-Axial strain curve of the sample DE-6

C.4 Mohr Circles of Samples

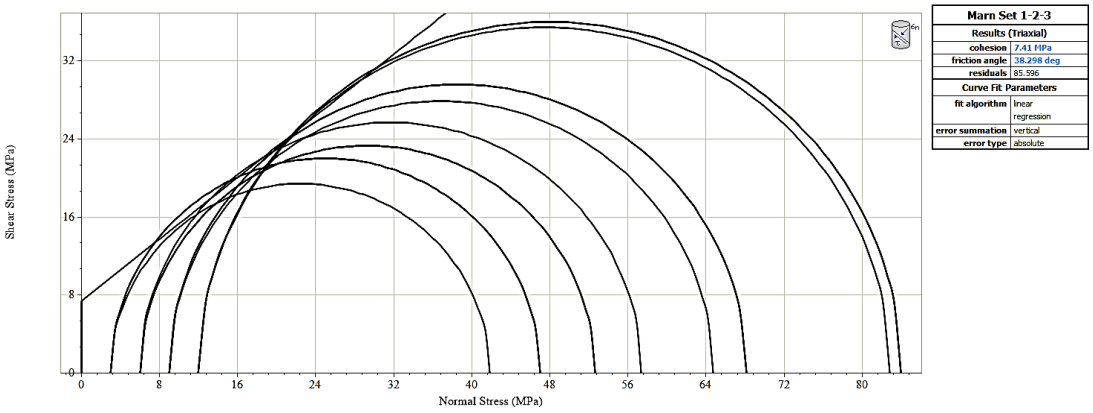

Figure C.21: Mohr's Circles of Marl

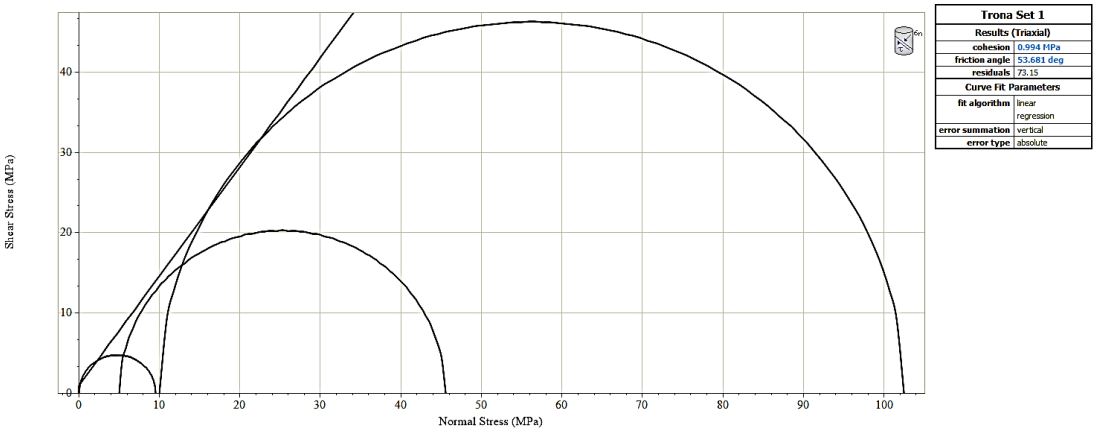

Figure C.22: Mohr's Circles of Trona

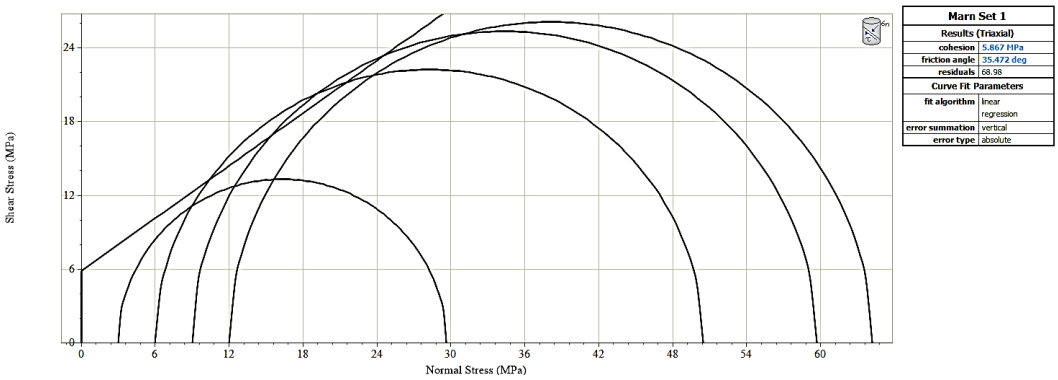

Figure C.23: Mohr's Circles of Marl (Set 1)

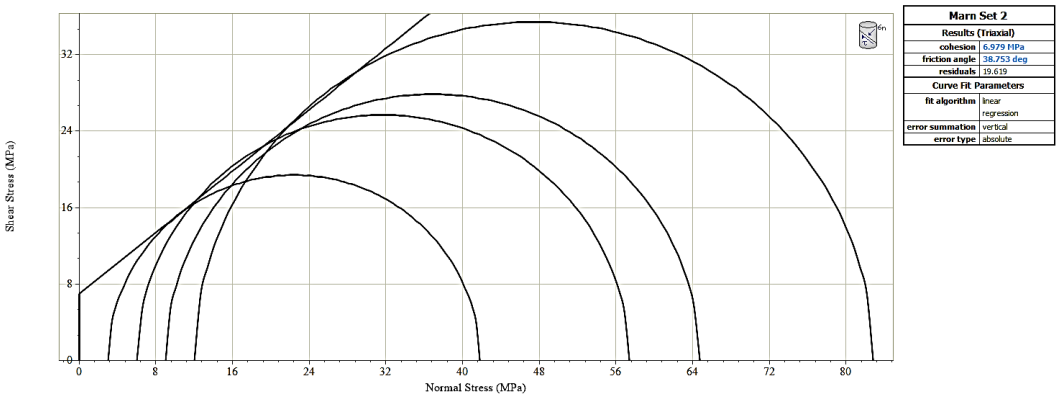

Figure C.24: Mohr's Circles of Marl (Set 2)

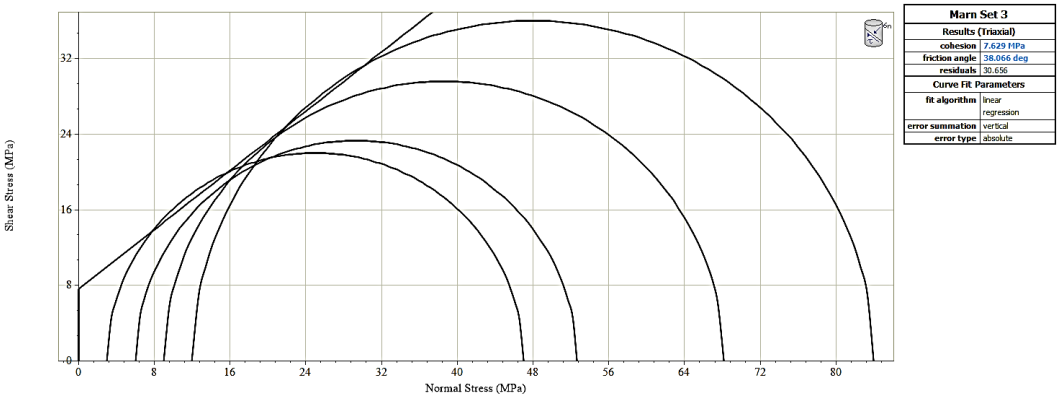

Figure C.25: Mohr's Circles of Marl (Set 3)

C.4 Specimen Photos

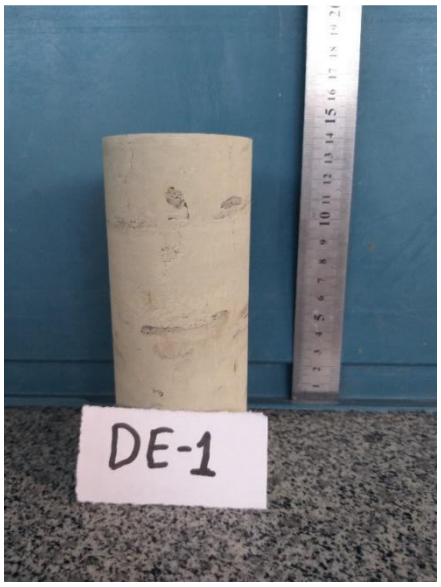

Figure C.26: Deformability Sample 1

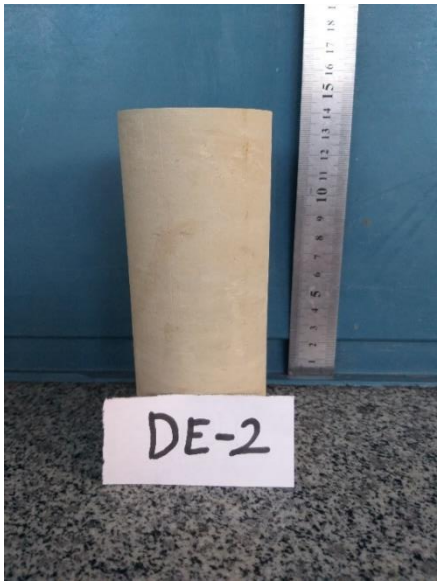

Figure C.27: Deformability Sample 2

Figure C.28: Deformability Sample 3

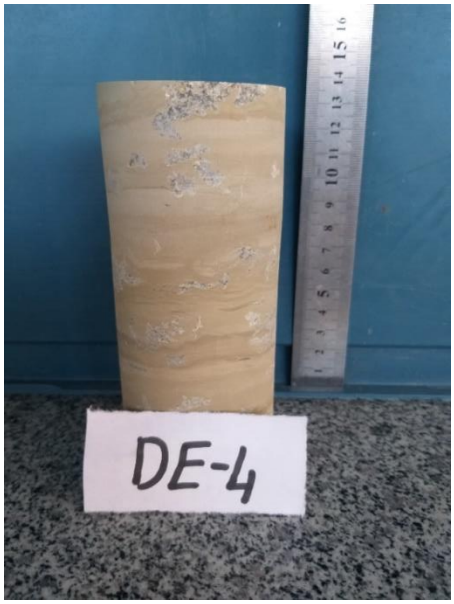

Figure C.29: Deformability Sample 4

Figure C.30: Deformability Sample 5

Figure C.31: Deformability Sample 6

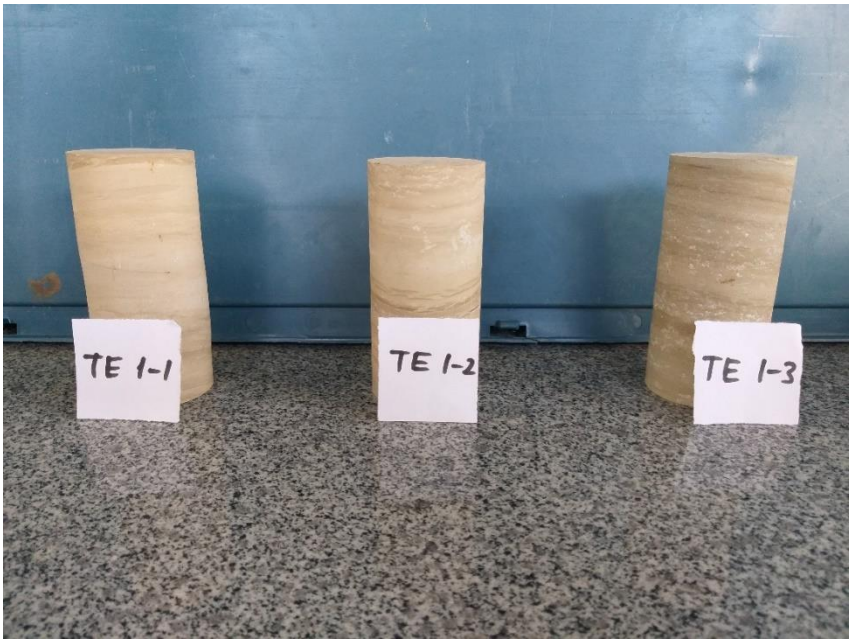

Figure C.32: Triaxial Specimens (Set 1)

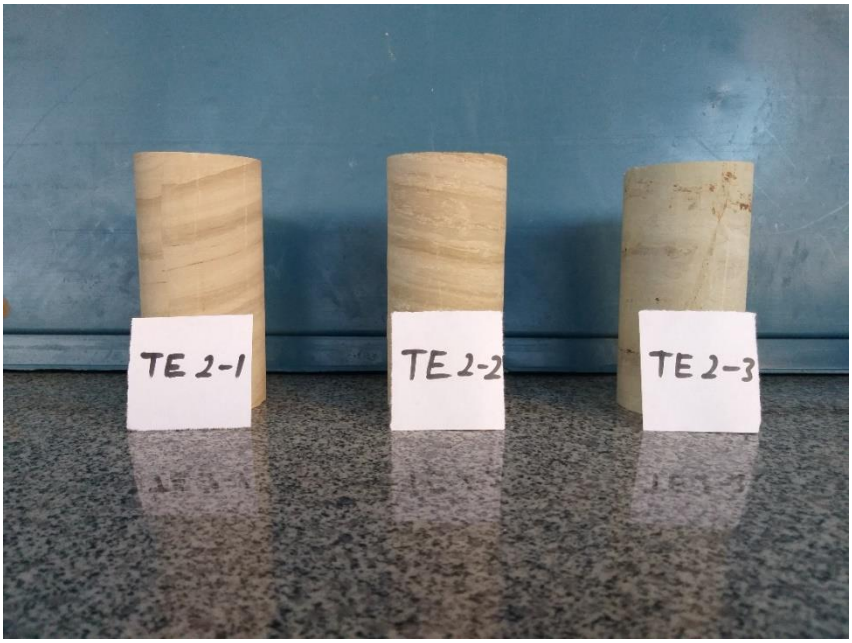

Figure C.33: Triaxial Specimens (Set 2)

Figure C.34: Triaxial Specimens (Set 3)

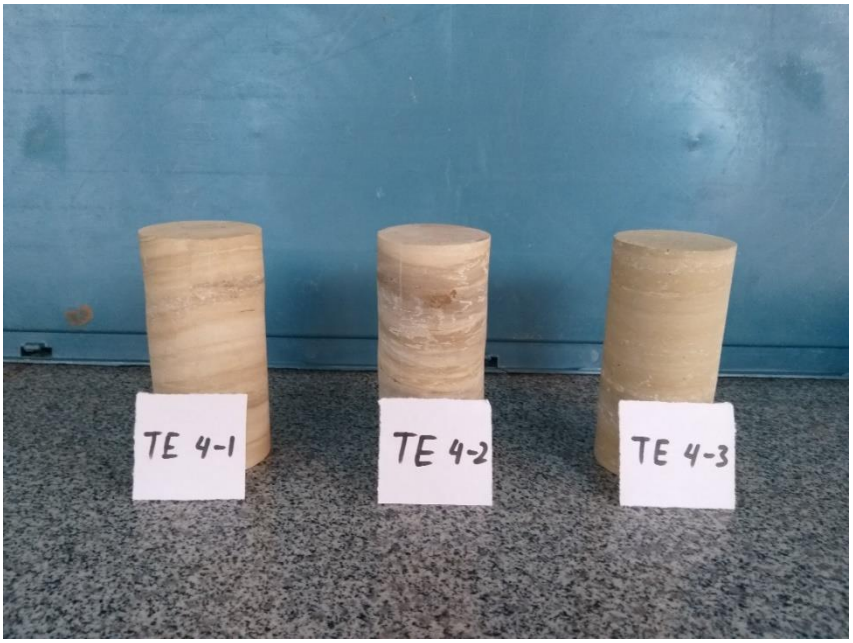

Figure C.35: Triaxial Specimens (Set 4)

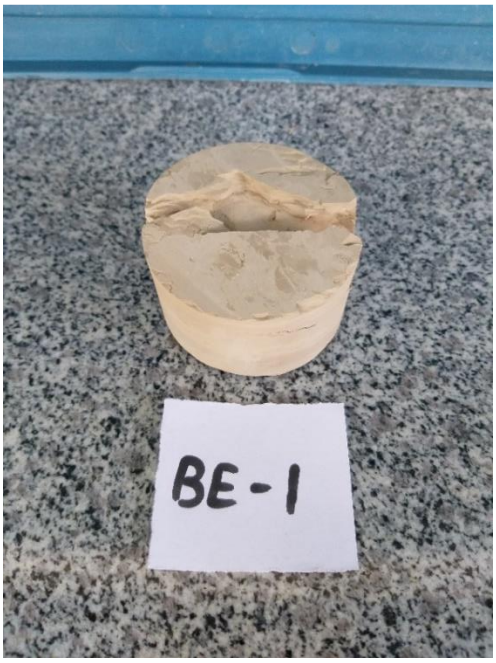

Figure C.36: Brazilian Test Sample 1

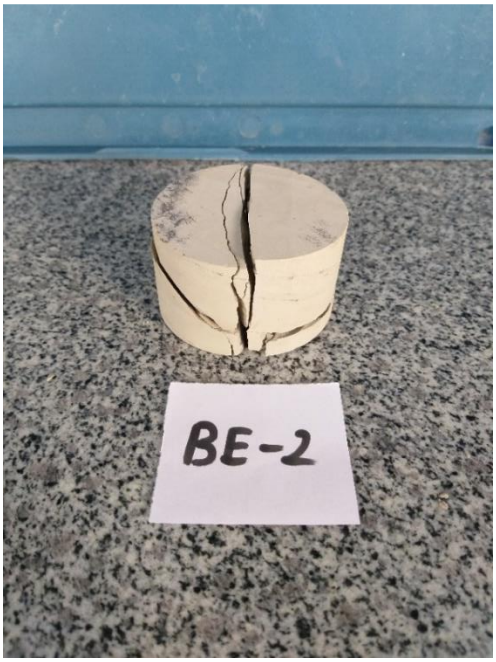

Figure C.37: Brazilian Test Sample 2

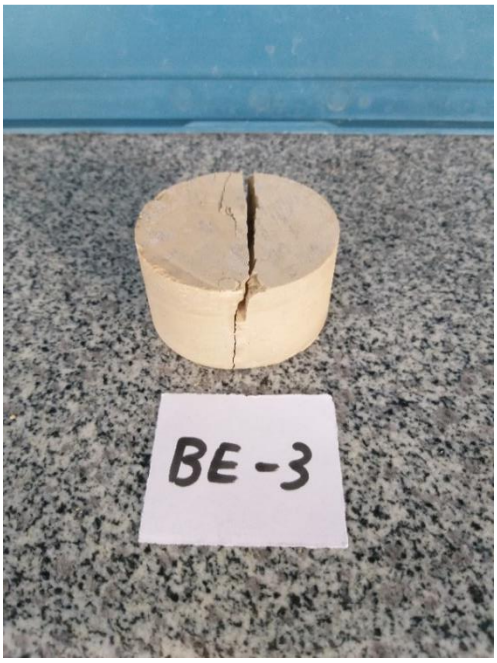

Figure C.38: Brazilian Test Sample 3

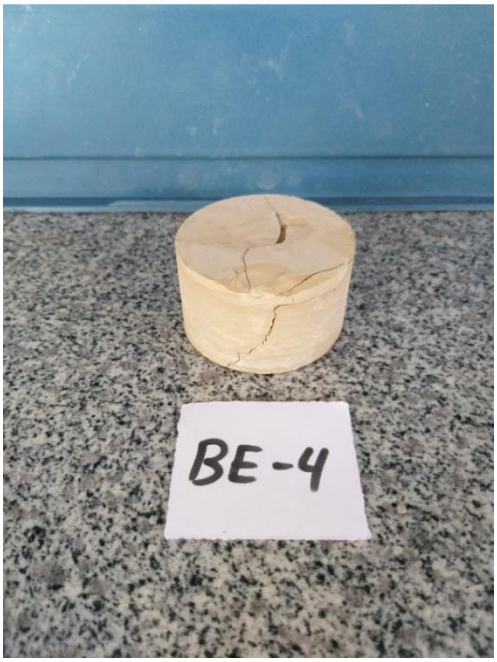

Figure C.39: Brazilian Test Sample 4

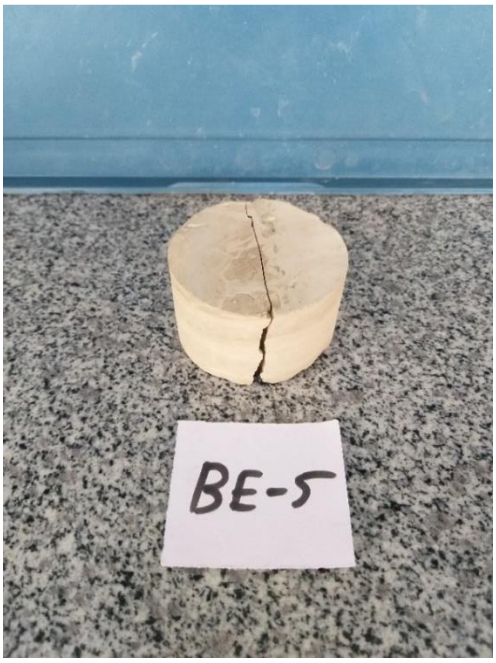

Figure C.40: Brazilian Test Sample 5

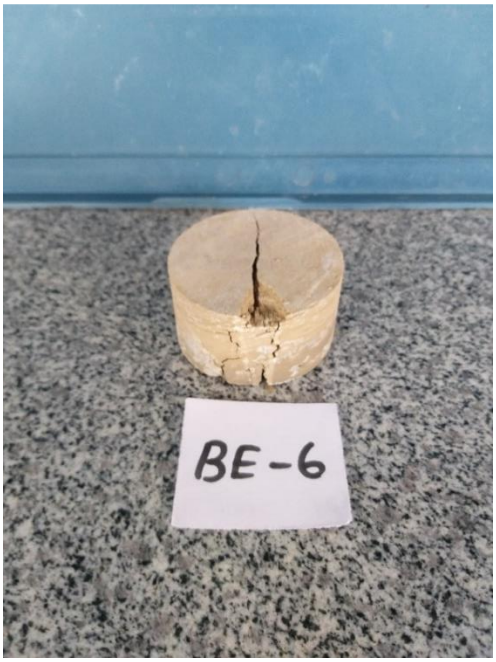

Figure C.41: Brazilian Test Sample 6

D. NUMERICAL ANALYSIS

D.1 Modelling Results

Table D.2: *Modelling Results for Marl (S_{hmin}= 3.5 MPa)*

S_{hmax} (MPa)	r_d (m)	Normalized Breakout Depth (% of r)
10.0	0.1080	0.00
10.5	0.1143	5.88
11.0	0.1145	6.00
11.5	0.1151	6.54
12.0	0.1161	7.51
12.5	0.1228	13.69
13.0	0.1233	14.17
13.5	0.1238	14.63
14.0	0.1244	15.17
14.5	0.1253	16.04
15.0	0.1296	19.97
15.5	0.1308	21.15
16.0	0.1312	21.50
16.5	0.1321	22.30
17.0	0.1322	22.45
17.5	0.1394	29.10
18.0	0.1399	29.51
18.5	0.1399	29.55
19.0	0.1406	30.16
19.5	0.1474	36.48
20.0	0.1495	38.46
20.5	0.1498	38.69
21.0	0.1508	39.66
21.5	0.1512	39.98
22.0	0.1514	40.18

Table D.3: *Modelling Results for Marl (S_{hmin}=2.9 MPa)*

S_{hmax} (MPa)	**r_d (m)**	**Normalized Breakout Depth (% of r)**
9.5	0.1080	0.00
10.0	0.1159	7.29
10.5	0.1162	7.57
11.0	0.1168	8.11
11.5	0.1180	9.24
12.0	0.1181	9.37
12.5	0.1200	11.12
13.0	0.1252	15.89
13.5	0.1264	17.01
14.0	0.1271	17.66
14.5	0.1275	18.03
15.0	0.1277	18.27
15.5	0.1291	19.53
16.0	0.1352	25.22
16.5	0.1365	26.35
17.0	0.1368	26.67
17.5	0.1373	27.10
18.0	0.1408	30.40
18.5	0.1413	30.88
19.0	0.1426	32.07
19.5	0.1434	32.78
20.0	0.1493	38.23
20.5	0.1510	39.82
21.0	0.1516	40.35
21.5	0.1520	40.69
22.0	0.1523	41.05

Table D.4: *Modelling Results for Trona (S_{hmin}=3.5 MPa)*

S_{hmax} (MPa)	**r_d (m)**	**Normalized Breakout Depth (% of r)**
3.3	0.1080	0.00
3.5	0.1143	5.88
3.7	0.1149	6.00
3.9	0.1161	6.54
4.1	0.1163	7.51
4.3	0.1181	13.69
4.5	0.1184	14.17
4.7	0.1186	14.63
4.9	0.1189	15.17
5.1	0.1206	16.04
5.3	0.1206	19.97
5.5	0.1218	21.15
5.7	0.1225	21.50
5.9	0.1229	22.30
6.1	0.1231	22.45
6.3	0.1241	29.10
6.5	0.1243	29.51
6.7	0.1245	29.55
6.9	0.1248	30.16
7.1	0.1250	36.48
7.3	0.1263	38.46
7.5	0.1274	38.69
7.7	0.1278	39.66
7.9	0.1282	39.98
8.1	0.1283	40.18
8.3	0.1289	40.46
8.5	0.1290	40.72
8.7	0.1301	40.98
8.9	0.1331	41.23
9.1	0.1335	41.49
9.3	0.1348	41.75
9.5	0.1355	42.01
9.7	0.1388	42.27
9.9	0.1394	42.53
10.1	0.1410	42.79
10.3	0.1415	43.05
10.5	0.1419	43.31
10.7	0.1422	43.57

Table D.5: *Modelling Results for Trona (S_{hmin}=2.9 MPa)*

S_{hmax} (MPa)	**r_d (m)**	**Normalized Breakout Depth (% of r)**
3.0	0.1080	0.00
3.1	0.1089	0.85
3.3	0.1095	1.37
3.5	0.1106	2.42
3.7	0.1107	2.54
3.9	0.1125	4.18
4.1	0.1221	13.06
4.3	0.1223	13.22
4.5	0.1227	13.64
4.7	0.1232	14.09
4.9	0.1299	20.27
5.1	0.1300	20.38
5.3	0.1304	20.74
5.5	0.1309	21.22
5.7	0.1312	21.52
5.9	0.1386	28.34
6.1	0.1390	28.66
6.3	0.1394	29.10
6.5	0.1396	29.24
6.7	0.1452	34.40
6.9	0.1453	34.54
7.1	0.1463	35.44
7.3	0.1470	36.13
7.5	0.1484	37.45
7.7	0.1493	38.21
7.9	0.1497	38.64
8.1	0.1500	38.92
8.3	0.1517	40.50

D.2 Correlation Between Normalized Depth Percentage and Stress-Strength Ratio

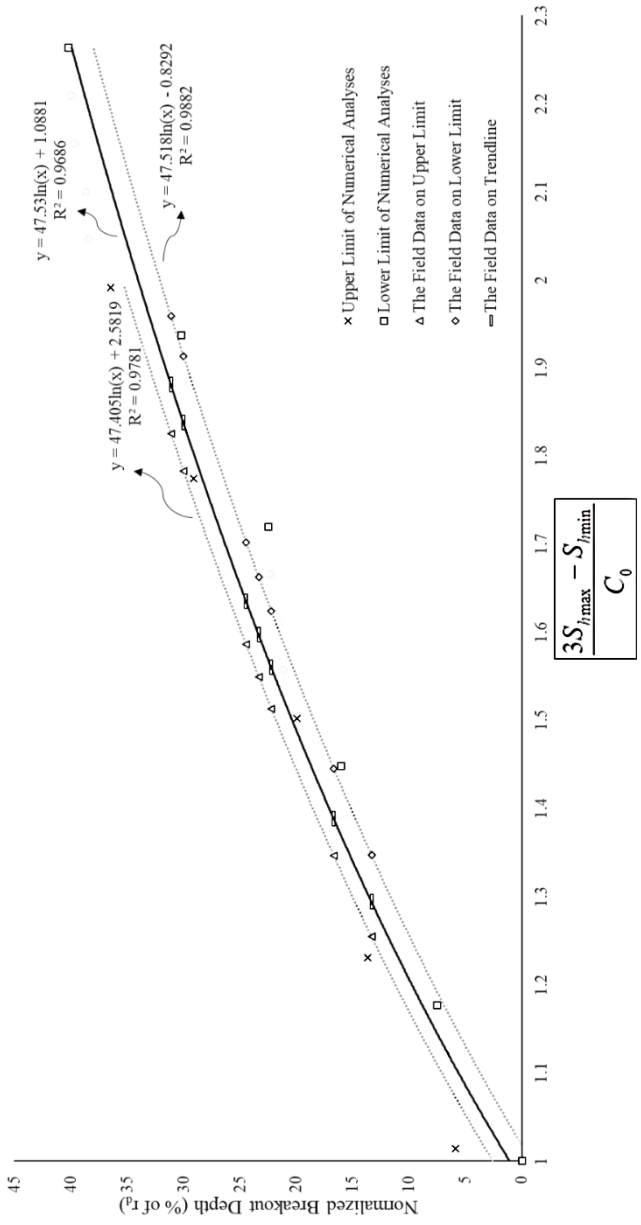

Figure D.42: Correlation between Normalized Depth Percentage and Stress-Strength Ratio of Marl for S_{hmin}=3.5 MPa

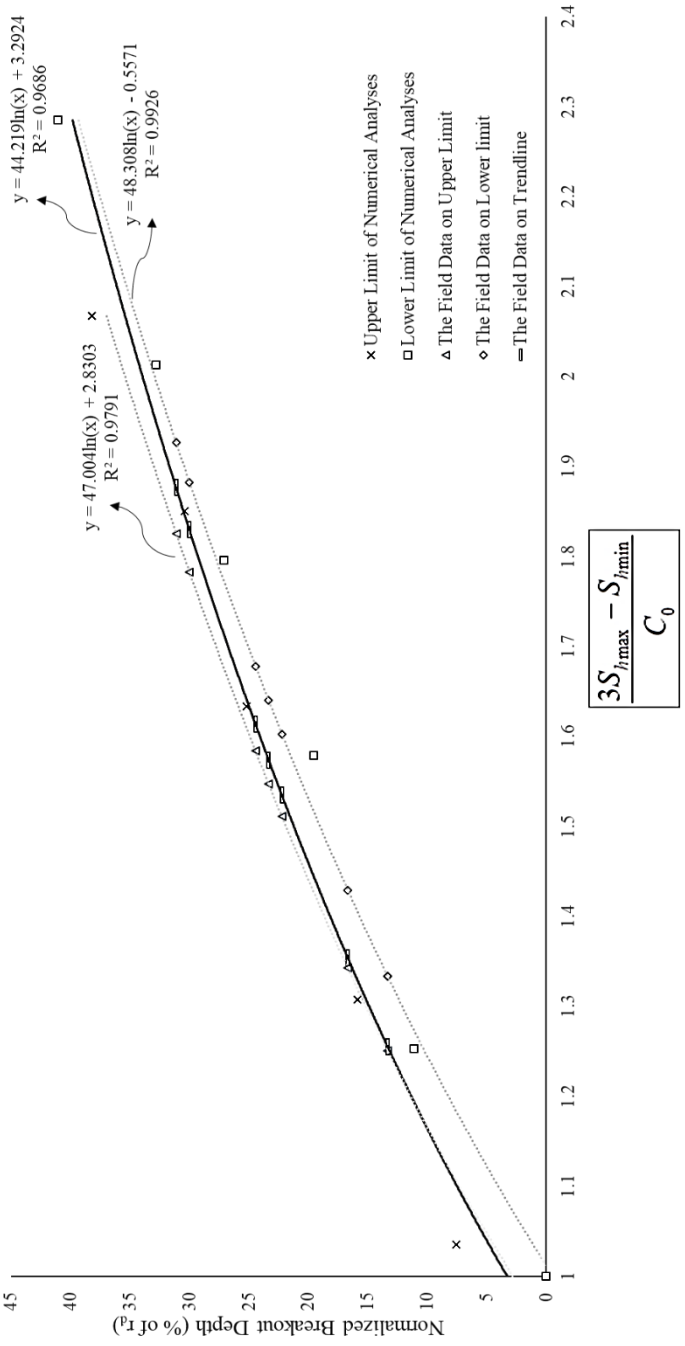

Figure D.43: Correlation between Normalized Depth Percentage and Stress-Strength Ratio of Marl for S_{hmin}=2.9 MPa

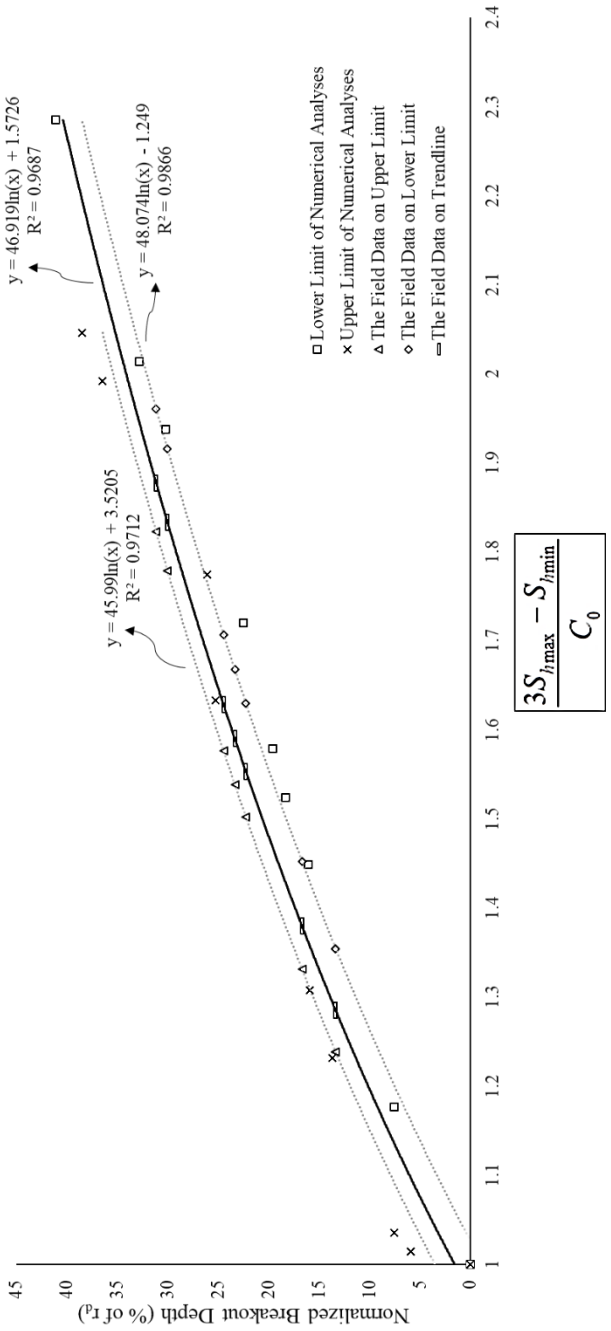

Figure D.44: Correlation between Normalized Depth Percentage and Stress-Strength Ratio of Marl for Average S_{hmin}=3.2 MPa

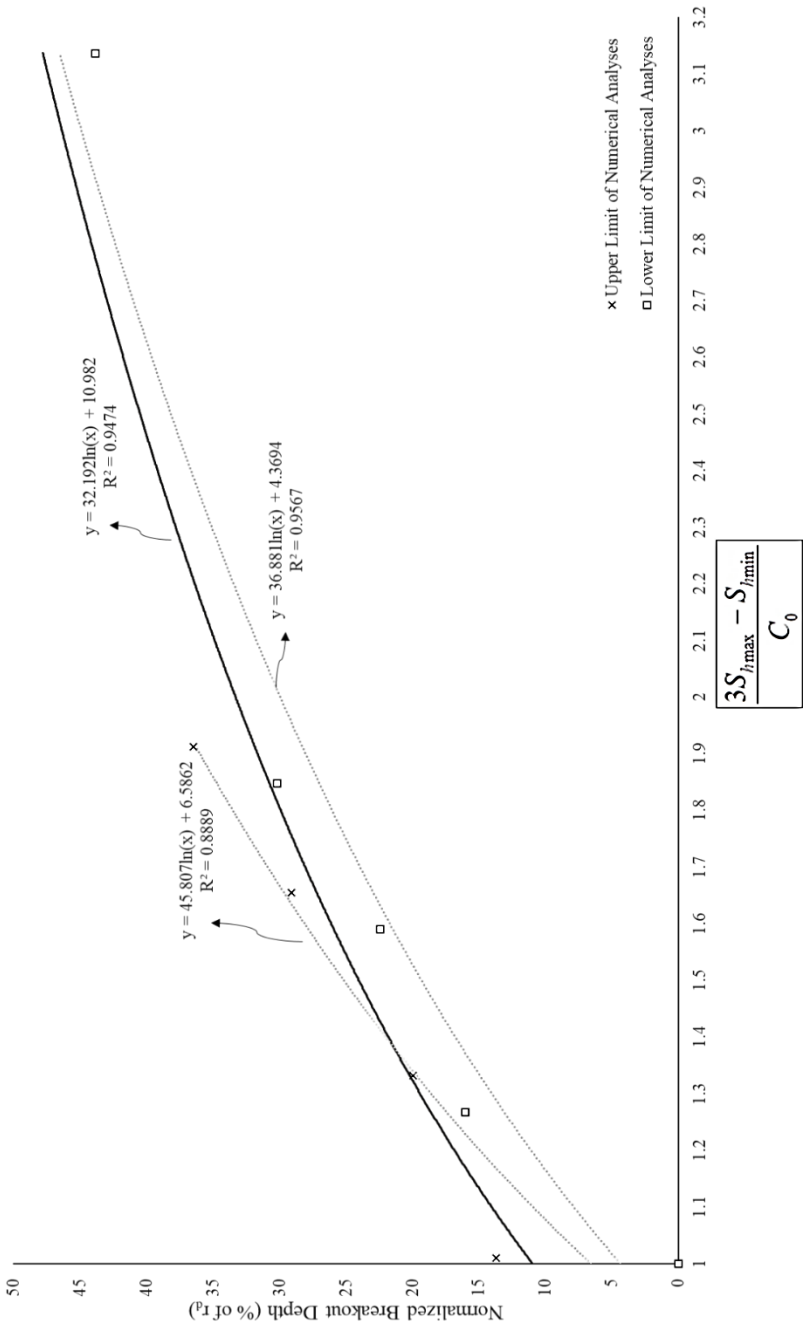

Figure D.45: Correlation between Normalized Depth Percentage and Stress-Strength Ratio of Trona for S_{hmin}=3.5 MPa

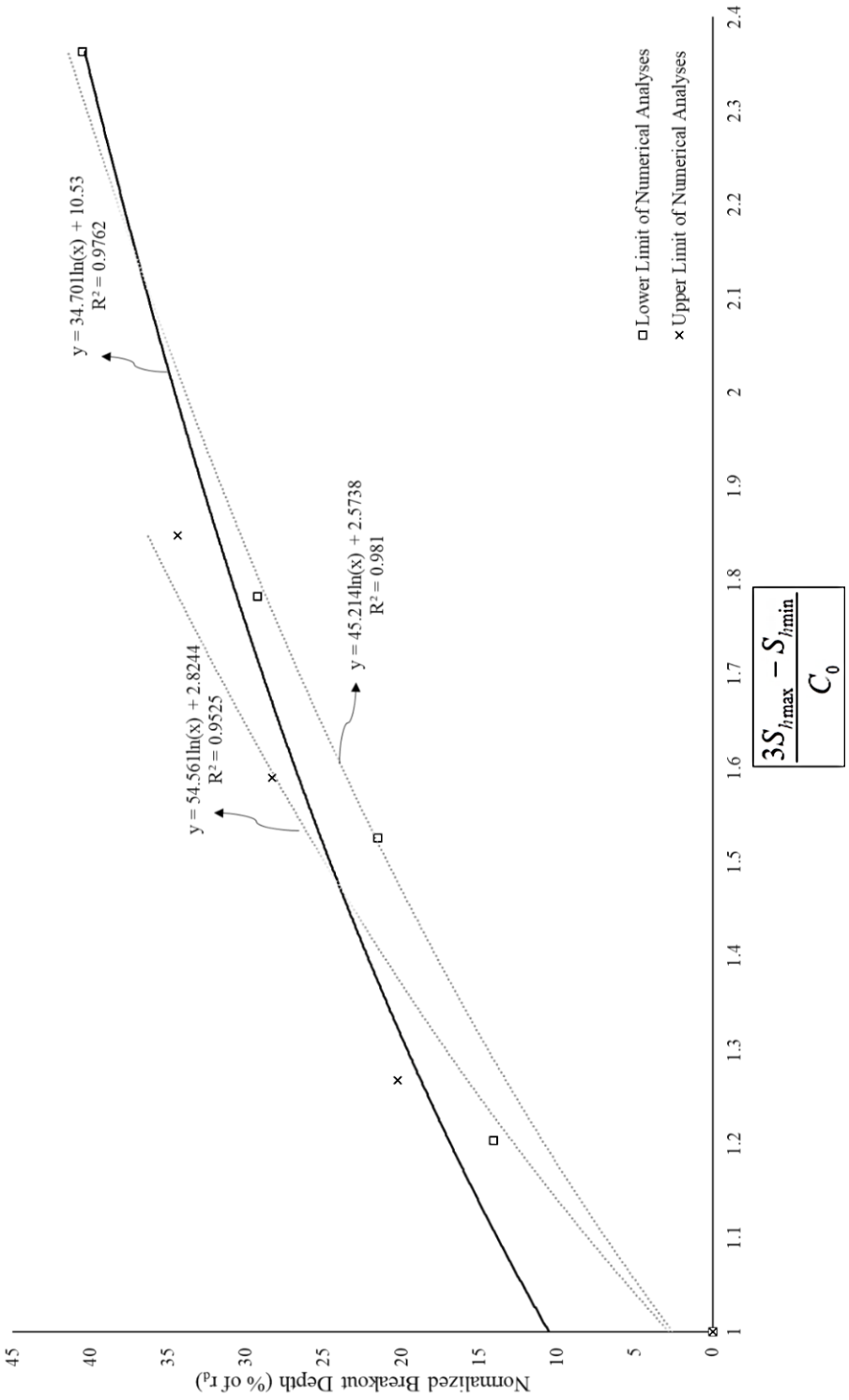

Figure D.46: Correlation between Normalized Depth Percentage and Stress-Strength Ratio of Trona for S_{hmin}=2.9 MPa

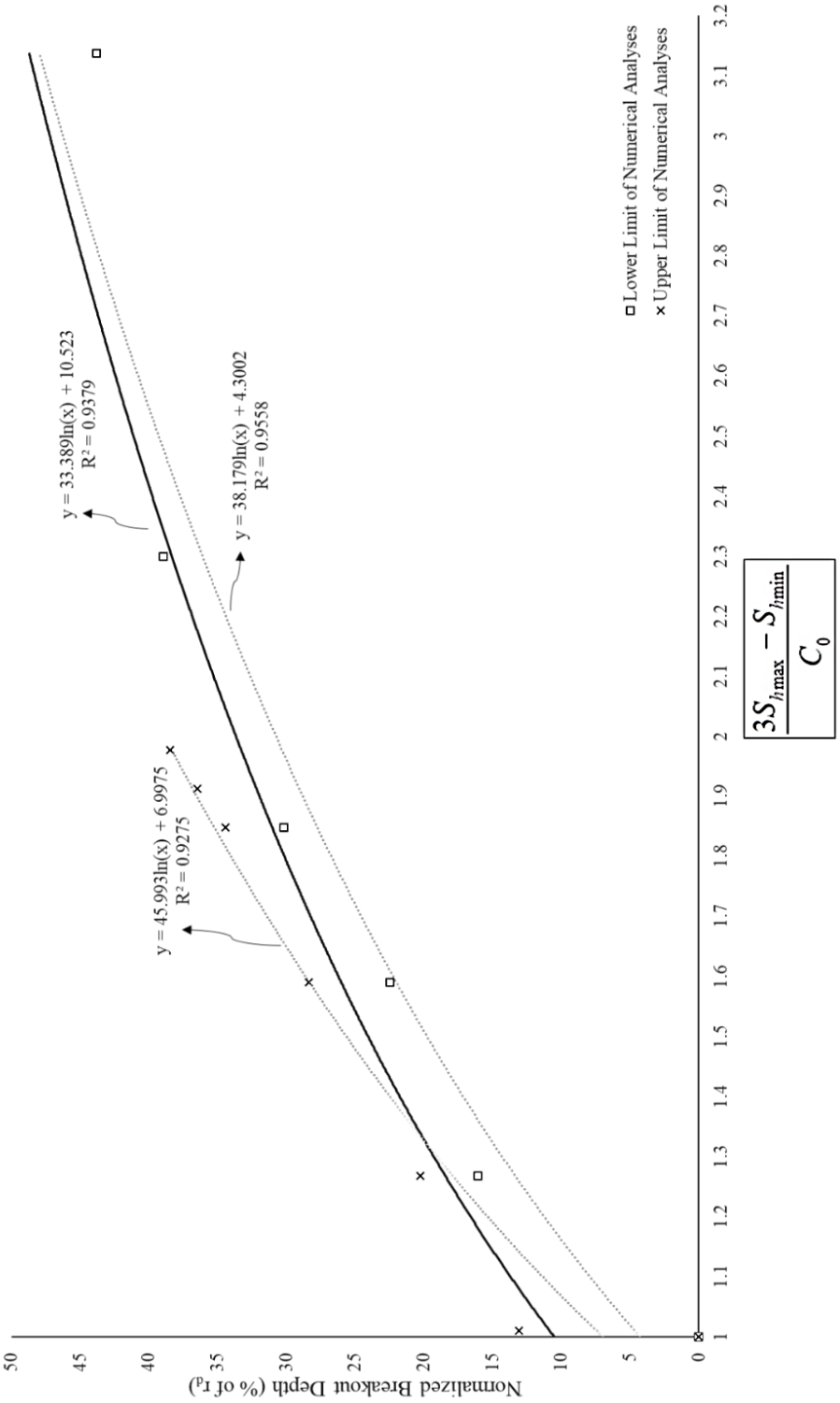

Figure D.47: Correlation between Normalized Depth Percentage and Stress-Strength Ratio of Trona for Average S_{hmin}=3.2 MPa

D.3 Relation Between Breakout Width of Numerical and Analytical Results

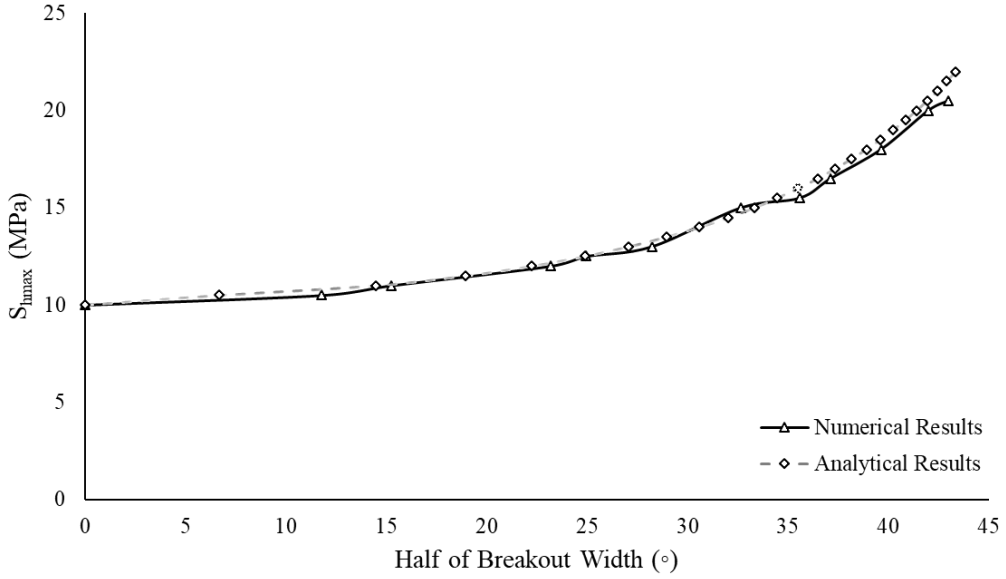

Figure D.48: Comparison of Equation 10 (Barton et al., 1988) and Numerical Results for S_{hmin}= 3.5 MPa (Marl)

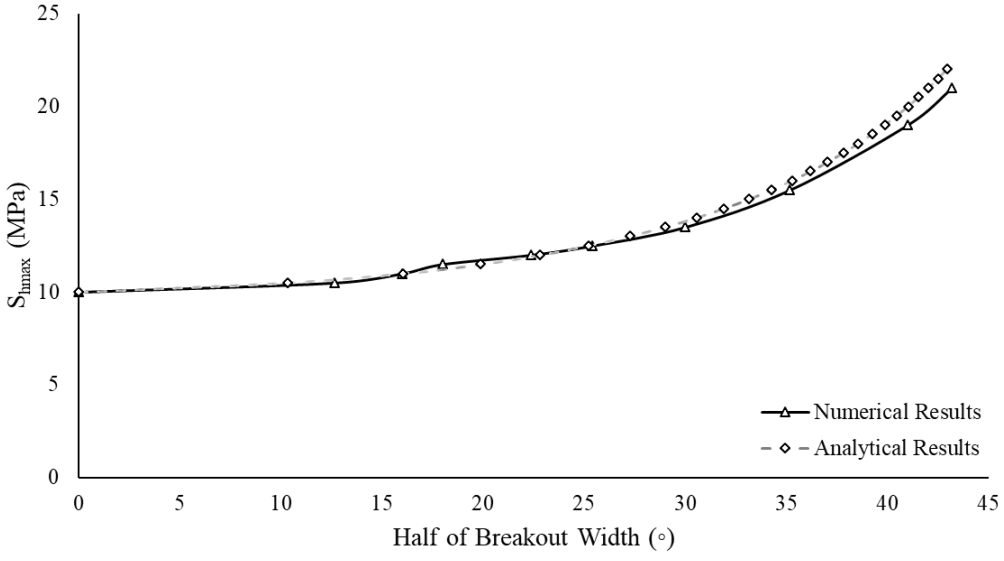

Figure D.49: Comparison of Equation 10 (Barton et al., 1988) and Numerical Results for S_{hmin}= 2.9 MPa (Marl)

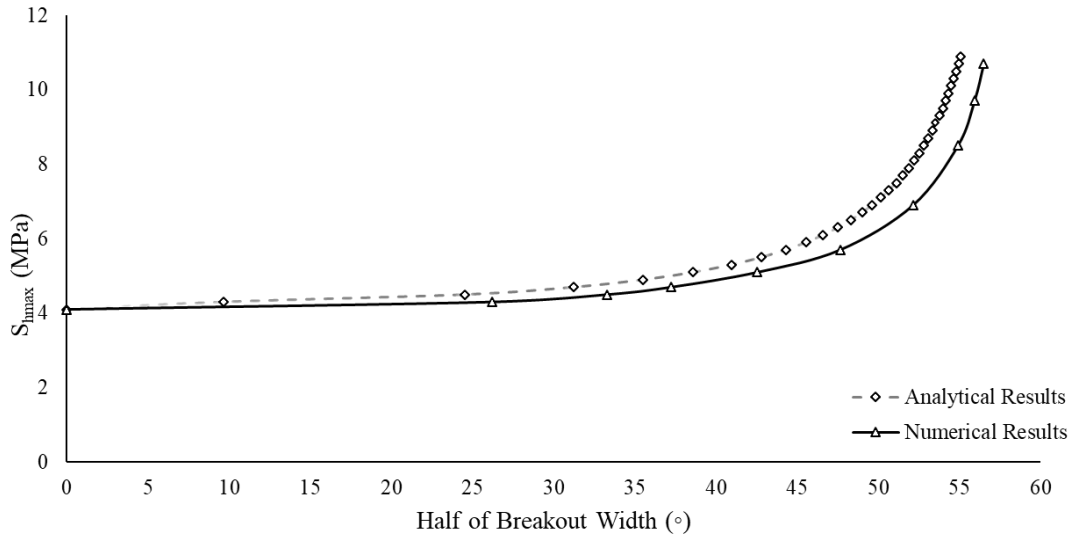

Figure D.50: Comparison of Equation 10 (Barton et al., 1988) and Numerical Results for S_{hmin}= 3.5 MPa (Trona)

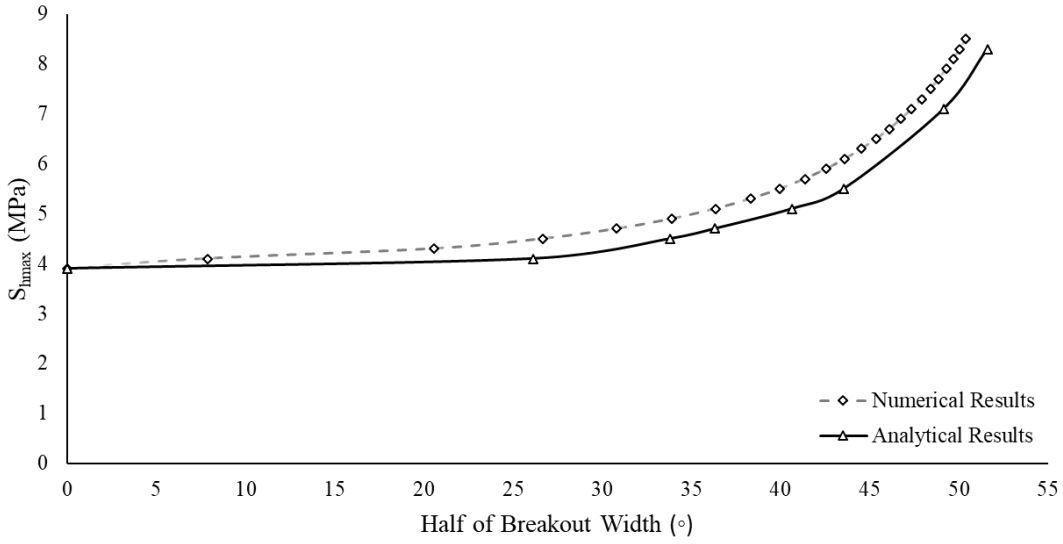

Figure D.51: Comparison of Equation 10 (Barton et al., 1988) and Numerical Results for S_{hmin}= 3.5 MPa (Trona)